Development of a Microfluidic Tool for Understanding Whole Cell Algal Cultures

Katherine Glover

Linacre College

Department of Engineering Science

University of Oxford

A thesis submitted for the degree of

Doctor of Philosophy

Michaelmas Term 2014

Abstract

Liquid biofuels, made from renewable sources, have the advantage over other renewable energy forms, such as solar, wind and tidal in that they can be stored and used on demand. Microalgae cultures are a source of lipids, for use as a raw feedstock to make biodiesel, and require a power input to mix them, and create a homogeneous culture. Some strains of microalgae are motile and can swim in reaction to the stimuli of light or chemical gradients.

This project focuses on the development, characterisation and use of a microfluidic tool to study cells in suspension, and the motility of cells. This microfluidic tool is designed to have a low convective flow, so transport is dominated by diffusion, which allows a 2D concentration gradient to be maintained and manipulated, and cells to swim without advection. Numerical simulations are used to characterise a microfluidic device, in which a concentration gradient can be maintained. A microfluidic device has been fabricated and utilised to analyse the motility of microalgae.

Whole cell cultures, which are more representative of the culture within a photobioreactor than the more commonly studied refined and concentrated cultures, are used throughout.

The rheology of the whole cell cultures, with bubbles rising through the fluid is modelled. The whole cell culture exhibited non-linear rheology. Despite this, it was found that bubbles rising through whole cell culture would impose a shear that correlated to the viscosity at the high shear plateau. That is, the medium around bubbles of any size, from 1 mm to 100 mm, has a viscosity of 0.001 Pas.

Numerical simulations are used to characterise and optimise the design and operation of the microfluidic devices. Recommendations regarding the geometry of the device include an inlet width to inlet neck length ratio of less than 2 and a radius of less then 400 μm.

Cheap, disposable PDMS devices were fabricated, a protocol was developed for filling the chambers and experimental concentration gradients were maintained.

Proof of concept is presented for visualising cells within a disposable PDMS microfluidic device with the design numerically simulated.

From this thesis, it has been shown that microfluidic devices have important potential for understanding the motility of microalgae in real environments and in controlled concentration gradients, although they require careful analysis and thoughtful fabrication.

Publications

Data in Chapter 5, Designing and Characterising a Microfluidic Device for a Controlled Concentration Gradient, was published in

Katherine Glover, Jon Strang and Alex S. Lubansky. Characterising the Effect of Geometry on a Microchamber for Producing Controlled Concentration Gradients. *Chem. Eng. Sci.*, 117, 389395, 2014.

Data in Chapter 8, *Tetraselmis* sp. Swimming Characteristics in Media with Varying Alginate Content, was orally presented in

Katherine Glover, Aimee S. Guha Roy, Alex S. Lubansky, Hua Ye, Robert Field, Zhanfeng Cui, The Rheology of Swimming Algal Suspensions, The XVIth International Congress on Rheology, Lisbon, Portugal, 2012.

Data in Chapter 4, Shear Effect of Bubbles Rising Through a Whole Cell Culture, was presented on a poster as

Katherine Glover, Aimee S. Guha Roy, Alex S. Lubansky, Robert Field, Zhanfeng Cui, The Difficulties of Measuring the Rheology of Whole Cell Cultures, The British Society of Rheology Midwinter Meeting: Food, pharma, health care and biological systems, British Society of Rheology, University of Nottingham, 2010.

Acknowledgements

I'd like to thank my supervisor, Alex, not only for his academic mentorship, but for the endless patience he has extended to me over the course of this project.

Cathy, thank you for being an understanding supervisor, and for all your help and advice. And thank you to the IBME family for adopting me and helping with the experimental work. Special thanks to Julian George, Prof Cui, Phill Putter, Shaoyang Yeh, Jinnan Zhang, Xiao Wan.

I acknowledge EPSRC DTA funding for making it possible for me to carry on studying and researching.

I acknowledge the algae cultures given to me by Aimee Guha Roy, and the advice and help from Prof Dirk Aarts' laboratory in fabricating the microfluidic devices. I also acknowledge the help of the Gurr Group for autoclaving glassware and advice on sterility, particularly the ever helpful Sarah Rodgers. I acknowledge Jon Strang's help in getting started with fabrication of the devices.

To my parents and sister, who have been worrying and cheering me on throughout my time as a student, thank you. And thank you for the endless proof reading.

Tamara, you have been an inspiration and your support unwavering. We've shared tears, laughter and drinks. I hope to share hundreds more with you.

Maryam, the short, sweet phone calls we have shared whilst we have both been studying our PhDs have given me an outlet for my frustrations and have been of much comfort to me. Here's to lazy afternoons shared together in the future.

Mike and Caroline, thank you for welcoming me into your home, feeding me delicious food, and providing a warm place for me to finish writing.

A huge shout out to the Ursula Hicks crew, especially Sean, Roya, Dan, Mel, Rachel, Ruben, Aleks and Stephen. I have shared some of the most fun times of my life with you and the most delicious home made snacks. After handing in, hopefully now my swearing will subside.

Thank you to countless miscellaneous friends, who have been neglected, but still continue to check on me, despite missed birthdays and weddings, especially Megan Garrod, Jimmy Peake, Sav Skinner, Robert Kiwanuka, Shiv Singh, Mohamad Fazeek and Bethan Willams and all my Welsh family.

Thank you to staff at the Engineering Department, who have made my life easier by going out of their way for me, Sara Downs on reception, Sukarni Wheeler, Kevin Corbett, Clive Stayt, Richard Dodsworth, Gary Axe and Jon Harding.

To the city and University of Oxford, you broke me and then made me a better and stronger person, a reluctant thank you.

And lastly, I want to thank Aled, who has felt every painful word and minute of experiments with me and whose love, pep talks and meals on wheels have sustained and motivated me. I could not have done this without you.

Contents

List of Figures

List of Tables

Nomenclature

δ	phase angle
$\dot{\gamma}$	shear rate
$\dot{\gamma}_c$	critical shear rate
η_f	apparent fluid viscosity
η_s	apparent solvent viscosity
γ	shear stress
μ	viscosity
ω	angular frequency
ρ	density
ρ_f	density of fluid
ρ_g	density of gas
τ	shear stress
Θ	volume fraction
a_b	bubble radius
c	concentration
$C_{(D_0)}$	drag coefficient
D	diffusion coefficient
G	Young's modulus
g	gravitation field
$G^{''}$	storage modulus
$G^{'}$	elastic modulus
p	pressure
r	radius of central chamber
Re_b	Reynolds number of a rising bubble
T	observation time
t	time

t_{95}	time to reach steady state
t_{exp}	experimental time to reach steady state
u	solvent velocity field
u	velocity vector
u_b	bubble rise velocity
u_{b_∞}	terminal bubble rise velocity
a	radius
De	Deborah number
EPS	extracellular polymeric substances
h	distance
Nanno	*Nannochloropsis* sp.
PDMS	polydimethylsiloxane
PTFE	Polytetrafluoroethylene
Re	Reynolds number
s	speed
Sh	Sherwood Number
SOP	standard operating procedure
Tetra	*Tetraselmis impellucida*
W	Inlet width

Chapter 1

Introduction

The world's reliance on fossil fuels has affected the climate [IPCC, 2014]. With a global population of over 8 billion, developing renewable, sustainable energy sources is a priority. Energy from biomass can be sustainable. Biomass can be controversial, often inciting arguments of 'food vs fuel'. Therefore, feedstock production must avoid using agricultural land that would otherwise be used for food production [Gallagher, 2008]. Biofuels are of interest, as unlike solar, wind and tidal, liquid biofuels can be stored and used on demand. Despite a wealth of research, liquid biofuel contributions to world energy production in 2008 was less than 1% [Williams and Laurens, 2010]. Fossil fuels accounted for 88%.

Microalgae[1] is an aquatic organism that harnesses the sun's energy by photosynthesis, and produces biomass. Contained within the cells are lipids which can be converted to biodiesel [Lee et al., 2012]. Algae cultures can grow in brackish and salt water, so could be cultured on land, or even in the ocean, without encroaching on valuable farming and arable land. Salt water algae don't compete for fresh water. Current limitations for commercially producing biodiesel from algae lipids on a large scale are the lack of research and development [Gallagher, 2008]. Choice of algae strains, culturing techniques, extraction, purification and transesterification are steps that don't have a fully developed commercially mature

[1] Macro algae i.e. seaweed, is not considered in this project. As such 'microalgae' is referred to as algae.

technology, and as such, it is not possible to make an estimate of how much green house gas emissions will be prevented by using biodiesel from algae over traditional liquid fuels derived from fossil fuels [Gallagher, 2008] [Scott et al., 2010].

The cultivation of microbes is present in many aspects of modern life. Improving the efficiency of cultivation is important, not only economically, but also to save raw materials and energy. Optimisation is only possible if the system is properly understood [Gill et al., 2008].

This project focuses specifically on the development and characterisation of a microfluidic tool to study cells in suspension, and the motility of single cells.

Chapter 2 is the literature review. It gives an overview of the usefulness of cultured algae and the relationship of cells and stress within bioreactors. Cell motility for suspended cells and chemically induced movement, chemotaxis, are reviewed. Previous studies using microchannels and motile cells are thoroughly reviewed with a justification for the chosen design for this project. The choice of polydimethylsiloxane (PDMS) for the fabrication material of the microchambers is also justified.

Chapter 3 summarises the materials and methods used in the project. Experimental methods and protocols are detailed. It sets out the assumptions and imposed constraints for the COMSOL Multiphysics 4.3b (COMSOL AB, Stockholm, Sweden) software simulations of the convective and diffusive transport within the microfluidic device. The mesh size and applicability of a 2D model of a 3D system is validated.

In Chapters 5 - 8 results from this project are presented.

Algae cultures need agitation to provide mixing and aid mass transfer. Agitation can be provided by aeration, either with air or carbon dioxide. Chapter 4 is the report of the experimental rheology exploration of algae whole cell cultures of *Nannochloropsis* sp. and *Tetraselmis impellucida* with an analysis of theoretically imposed shear from bubbles of different sizes.

In this project a microfluidic device was designed and developed that allowed a con-

centration gradient to be maintained, and by changing the design geometry and operating parameters allows manipulation of the concentration gradient and the flow regime within the central chamber to create conditions favourable to study for motile cells. A schematic is shown in figure 1.1(a). Motile cells can exhibit chemotaxis, movement in response to a chemical signal [Ahmed et al., 2010]. However, motile cells can start to tumble, and flow with the bulk convection over a critical liquid velocity [Marcos and Stocker, 2006].

Chapters 5 and 6 are the results and analysis of numerical simulations of a microfluidic device of different designs and under different theoretical operating conditions. These results are useful for designing experimental microfluidics.

In Chapter 5 COMSOL simulation results were analysed to ascertain the effect of the geometry of the microfluidic device on three key features - the time for the concentration gradient to reach steady state, the shape of the concentration gradient and the flow regime within the central chamber.

Chapter 6 uses an optimised geometry, from the previous chapter, to study the effect of flow rate in the inlet channels and the inlet/outlet configuration, on the same three key features as the previous chapter.

PDMS channels were then fabricated, a protocol for filling the chambers was developed and characterised experimentally. Chapter 7 contains the experimental results from the characterisation of the fabricated PDMS channels, using dye as a visual indication of the concentration gradient. Recommendations have been made to make more robust and improved devices.

In Chapter 8 whole cell cultures are introduced into the central chamber of the microfluidics device under different media conditions. There is a discussion of the issues with getting motile algae into the chamber.

Chapter 9 brings together all the conclusions from the project, and Chapter 10 outlines prospective future work to extend the project.

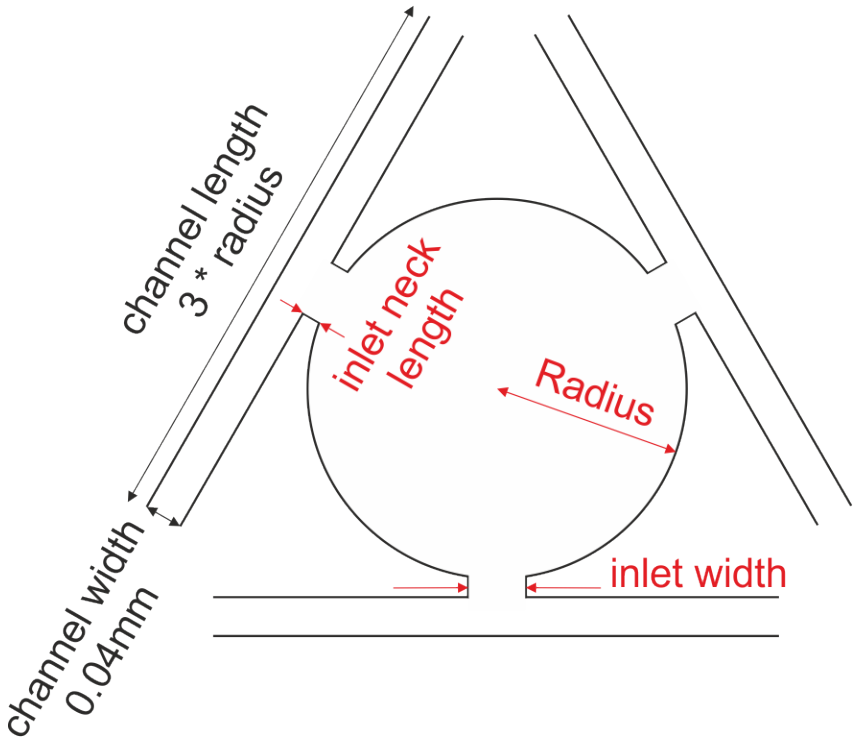

(a) Schematic of geometery. Three inlet/outlet channels and a circular central chamber

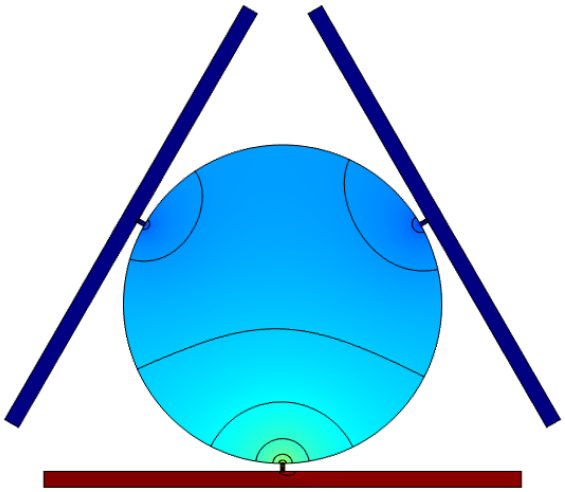

(b) Concentraion profile within a central chamber, with one inlet as a source and two outlets as sinks

Figure 1.1: Microfluidic device capable of maintaining and manipulating a concentration gradient

Chapter 2

Literature Review

2.1 Uses for algae

Microbes produce a huge array of valuable products. In their natural state they will only produce small amounts, useful for their own benefit. However, cultivated under the right conditions microbes will produce larger amounts that can be harvested and purified for use in medicine such as penicillin [Barrios-Gonzalez et al., 1988] or foods e.g. citric acid [Xu et al., 1989], monosodium glutamate, alcohol, and cosmetics [Mata et al., 2010]. Recent research, driven by the desire for an alternative to fossil fuels, has evaluated microalgae as a feedstock for biofuel [Gouveia and Oliveira, 2009, Daroch et al., 2013, Greenwell et al., 2010]. There has been research on all stages of the cultivation process from bioreactor design [Schenk et al., 2008], developing methods to increase lipid content in microalgae cells to act as the raw ingredient for biodiesel [Griffiths and Harrison, 2009], the best method for breaking cell walls and extraction of the oil [Lee et al., 2012, Steriti et al., 2014] to choice of algae strain [Rodolfi et al., 2009]. Microalgae has benefits as a feedstock over traditional feedstocks, of oil crops, waste cooking oil and animal fat. Microalgae is a non-food feedstock and does not compete for arable land, needs approximately 100 times less land area than agriculture crop feedstocks, uses water that is unsuitable for human consumption [Mata et al., 2010]

and can be continually harvested providing a steady year round supply of raw feed [Chisti, 2007, Rawat et al., 2013]. These unique properties of algae provide an opportunity to meet global market demand for transport fuels without competing with other technologies and sectors for scarce resources. Chisti [2007] and Schenk et al. [2008] both agree that microalgae appear to be the only source of biodiesel that has the potential to completely displace fossil diesel and meet global demand for transport fuels.

For the experimental results chapter 4 two algal species *Nannochloropsis* sp. (Nanno) and *Tetraselmis impellucida* (Tetra) were explored purchased from Marine Biological Association of the UK, Plymouth, strains 588 and 429 respectively. Both are salt water algae.

Tetra was chosen as the *Tetraselmis* sp. is a candidate for producing lipids to be converted into biodiesel [Mata et al., 2010]. It's also a motile algae [Jaouen et al., 1999].

Nanno was chose for its high lipid content, which makes it desirable as a feed stock for biodiesel Chiu et al. [2009].

2.2 Cell motility

Motile cells have many different ways of moving [Cappuccinelli, 1980]. Prokaryotic or bacteria cells use flagella (Figure 2.1 (a) to (c)), either one or many. Eukaryotic cells use cilary movement or flagellar movement or amoeboid movement. Amoeboid movement is not considered any further, as it is effective for locomotion in a non-liquid environment, but not applicable to cells in suspension. Figure 2.1 d) is the method that both Tetra and Nanno use to swim. They have flagella on one pole, that are used to pull themselves forward.

Although having similar names bacteria flagella and eukaryotic flagella are structurally different and use different methods for movement [Bray, 2001]. Bacteria flagella are rigid helical structures that are rotated by a motor in the cell wall. Eukaryotic flagella use uniform undulations usually from base to tip. Cilia are structurally similar to eukaryotic flagella, but there tends to be more of them and they use biphasic beating; a fast effective stroke and a slow recovery stroke slightly out of phase with the next cilia [Ishikawa, 2009].

Cheomtaxis is the ability of organisms to sense gradients in their chemical environment and adjust their motile behaviours accordingly. Purcell [1976] discusses that cells do not move to 'scoop-up' more nutrients; they cannot move fast enough. *"To increase their food supply by 10% [the cell] would have to move 20 times faster than it normally swims."* Also stirring the local environment is far out stripped by diffusion according to Sherwood's number, so cells are not actively trying to alter their surroundings. However, they do possess the ability to sense their environment and therefore increase nutrient uptake by moving up a concentration gradient. Cells are also able to sense detrimental circumstances and move down a concentration gradient to escape.

2.3 Microchannels and motile cells

Weibel et al. [2007] states the field of microtechnology is beginning to impact on microbiology. Microfluidics is the manipulation of fluids on a micrometer scale [Whitesides, 2006].

Microfluidic devices can be used to study carefully controlled concentration gradients. Clever geometries allow gradients to be maintained and manipulated [Wegrzyn et al., 2012]. Fleming Glass et al. [2008] summarised that microfluidic environments are well suited to vary the concentration of the environment surrounding a cell. Due to the inherently small length scales in microfluidics, flow is often laminar, with a Reynolds number less than 1. The size of microchannels also lends itself well to study celluar chemotaxis. Its scale of size is well matched to the physical dimensions of microganisms - individual cells can be tracked. Devices have been designed to facilitate diffusion in the absence of convection, allowing concentration gradients to develop without flow-induced shear stress [Du et al., 2009].

Previously published works have used microchannels to study cell suspensions. Kolnik et al. [2012] used many individual chambers with small inlets to a main perfusion channel. Adherent shear sensitive mammalian cells within the small chambers are subjected only to low flow velocities. The concentration in the chamber is dependant on the concentration in

the main perfusion channel and also the entrance width. Although it was mentioned that the time to equilibrium could be controlled using the entrance width, the control of the concentration gradients through changing the entrance width was not explored. Du et al. [2009] studied attached shear sensitive mammalian cells using evaporation to drive transport and develop a concentration gradient.

Motile cells in suspension have also been studied. Rusconi et al. [2014] used a serpentine polydimethylsiloxane (PDMS) channel to demonstrate hydrodynamic shear and how it can trap motile suspended cells in high shear regions. Ahmed et al. [2010] used diffusion through a hydrogel to create a concentration gradient in a test channel, which had no convective flow within it, particularly suitable for studying bacterial chemotaxis. However diffusion must happen through agarose gel. Mao et al. [2003] produced a device that uses 22 outlets at different positions to capture cells according to their migration. Bulk flow was used to push cells along a relatively long channel, 18 mm, which may have affected a cell's ability to migrate. Ahmed and Stocker [2008] experimentally verified chemotaxis theory using PDMS fabricated channels. They create a concentration gradient of a chemo-attractant in 60 μm wide microcapillary and track cell velocity. The concentration gradient is created using a one off injection, meaning the concentration gradient changes slowly over time.

Microfluidics has been used to study cell motility in controlled and predictable vortices. Marcos and Stocker [2006] used a PDMS microfluidics channel to study the ability of algae and bacteria cells to resist advection in vortices of different strengths. It was found that cell are only able to be actively motile up to a critical flow speed. After this critical speed, which is related to the cell swimming speed, is exceeded the cells travel by advection, tumbling in the flow.

Motility of cells has been combined with PDMS microfluidics to create a diagnostic tool for heavy metal contamination Zheng et al. [2012]. The algae motility of the suspended cell populations was evaluated for varying concentrations of copper and cadmium. As the concentration of heavy metal increased, the cells motility gradually decreased.

2.3.1 Controlled diffusion microchamber

A common disadvantage of both Ahmed et al. [2010] and Mao et al. [2003] geometries is the restriction to a one dimensional concentration gradient. Atencia et al. [2009] addressed this issue and used a geometry that allows chemotaxis to be studied in a two-dimensional chemical gradient, within a central chamber, called a microfluidic palette, shown in figure 2.2). Atencia's claimed benefits for the device include not only a 2D gradient, but also a quick equilibrium time. An absence of hydrogels and membranes through which molecules have to diffuse means that even without bulk flow, time to reach steady state is relatively short [Atencia et al., 2009]. A feature that is drawn attention to by Ahmed et al. [2010] is the ability to quickly switch chemicals in the three feeder channels, so chemical gradients can be altered during experiments.

Flexibility in the set up is provided by 3 inlet/outlet channels. One source and two sinks allows a gradient to develop in 2D. Source and sink channels are interchangeable making it possible to study the effect of a changing concentration gradient on chemotaxis. It is possible to have two or three source channels with different chemoeffectors in each, to explore the effect of different combinations across a full range of concentrations. Three inputs is the maximum which allows all combinations of diffusive species to be represented. Although there is scope for more inlets, three provide enough flexibility without over-complication and redundancy. Flow rates and flow direction in the three channels can be varied independently.

Ahmed et al. [2010] points out that a limitation of the device is the complex shape of the gradient. In Chapter 5 of this work a numerical model has been developed to find the optimum dimensions of a diffusion chamber for a given application. Flexibility in the set up of the microfluidics device means that inlets can be arranged in different configurations, and has been explored in chapter 6.

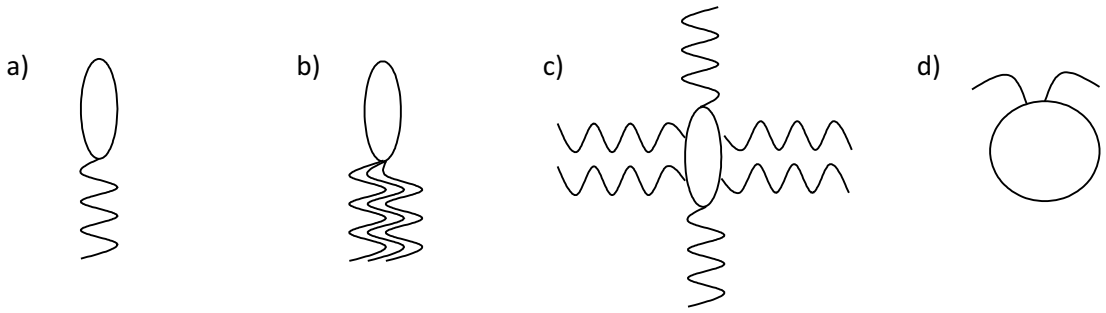

Figure 2.1: Flagella distribution on micro organisms a) polar flagellated bacterium with a single flagellum b) bundle of flagella on a pole c) bacterium with flagella over the entire surface d) eukaryotic micro algae with 2 flagella. Adapted from Cappuccinelli [1980]

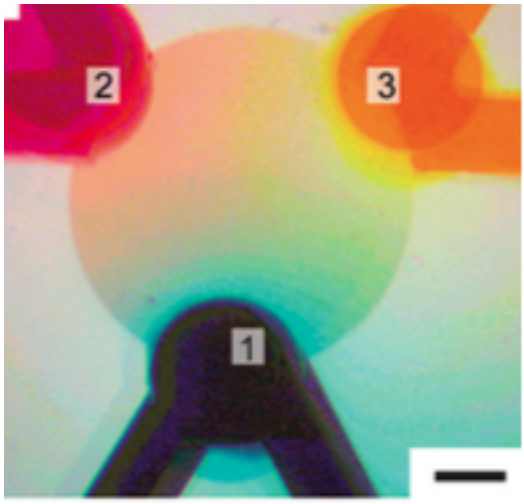

Figure 2.2: Atencia et al. [2009] working palette, three different coloured dyes, diffuse to create a 2D concentration

2.4 Microchannels fabricated from PDMS

For experimental work, microfluidic devices were fabricated to obtain data on real working conditions. This data is reported in chapters 7 and 8, and the fabrication methods in chapter 3. The choice of material for the microfluidic devices was polydimethylsiloxane (PDMS). There are several reasons to choose PDMS as the material. Weibel et al. [2007] assures readers the techniques of soft lithography are sufficiently easy to learn so that it is possible to experiment without a major investment in time and resources. It is also quick; it is possible to go from design to working device in less than two days [Whitesides, 2006]. PDMS is biocompatible leading Whitesides [2006] to suggest that it might ultimately be possible to embed microfluidic devices *in vivo*. This means that it will be suitable to study living cells in suspension.

Polymers, in contrast to silicon and glass, are inexpensive, as are the techniques for forming channels; channels can be formed by moulding or embossing rather than etching.

The transparency of PDMS allows simple and readily available microscopy techniques to be used in the visualisation, such as bright field [Ahmed et al., 2010].

2.5 Rheology theory

Rheology is the study of the flow of matter. A model Hookean solid is described by $\tau = G\gamma$, where τ is the shear stress, G is the Young's modulus and γ is the strain [Tanner, 2000]. There is no time dependence between the application of a force and the resulting deformation. All deformation as a result of an applied stress is instantaneous. A model Newtonian liquid is described by $\tau = \mu\dot{\gamma}$ where μ is the viscosity, $\dot{\gamma}$ is the strain rate and there is linear time dependence. A stress applied to a liquid will deform continuously as long as the stress is applied. These two models are the ideals at opposite ends of the spectrum of ideal materials.

2.5.1 Elasticity and Maxwell fluids

A Maxwell viscoelastic fluid is a model fluid, which has both a viscous and an elastic component [Goodwin and Hughes, 2008]. It is best represented by a spring and a piston in series as shown in figure 2.3.

Mathematically it can be described by

$$\frac{\partial \gamma}{\partial t} = \frac{1}{G}\frac{\partial \tau}{\partial t} + \frac{1}{\mu}\tau \tag{2.1}$$

For small observation times, T, the observed material properties are dominated by the spring. The spring extends but the piston does not have time to react; it appears to act as a solid. As T increases, the piston has time to react and it appears more fluid like. Deborah number is the dimensionless number that describes what kind of behaviour is observed, $De = \tau/T$. A high Deborah number corresponds to solid behaviour, and a low Deborah number to fluid like behaviour.

Rotational rheology is a technique that is used to explore a material's rheological properties. A sample is loaded between the two plates of a rheometer. One plate imposes a continuous stress. The strain is measured from the resultant amount of rotation.

If a Maxwell fluid is subject to constant stress in a rheometer i.e. $\frac{\partial \tau}{\partial t} = 0$ then equation 2.1 will reduce to $\dot{\gamma} = \tau/\mu$, and will appear to act as a Newtonian fluid. If μ is constant under a range of stresses, we must investigate whether the material is Newtonian, or has an elastic component and is a Maxwell fluid. This is done with an oscillatory test. The sample is subject to a harmonically varying time dependant strain, figure 2.5.

$$\gamma = \gamma_0 cos(\omega t) \tag{2.2}$$

For a solid described by $\tau = G\gamma$ there is no time dependence, so the stress response to the

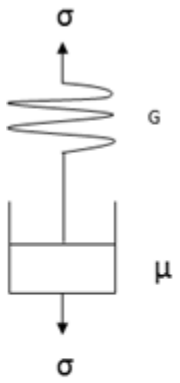

Figure 2.3: Spring and piston in series representing a Maxwell fluid

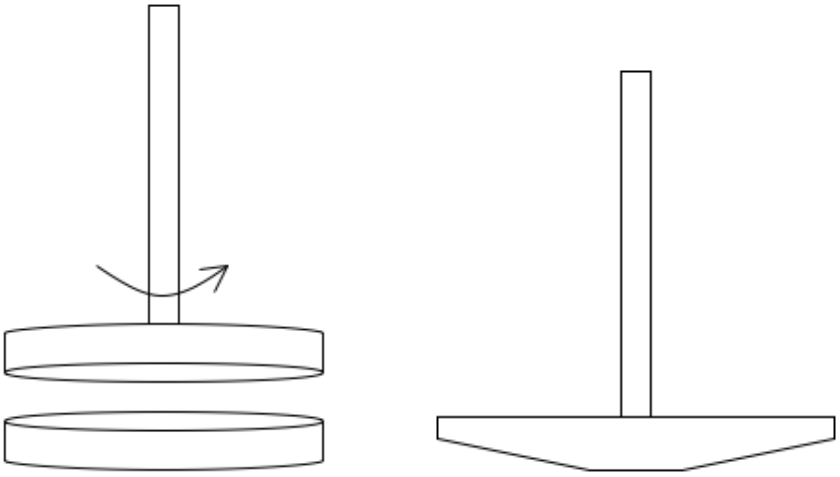

(a) Schematic of rheometer parallel plates (b) Schematic of rheometer cone plate

Figure 2.4: Schematic of the choice of rheometer plates

shear is in phase, shown in figure 2.5 ,

$$\tau = \tau_0 cos(\omega t) \tag{2.3}$$

where ω is angular frequency and t is time.

For a viscous fluid, where $\tau = \mu\dot{\gamma}$, where by differentiating equation 2.2 the stress response is dependent on strain rate:

$$\tau = \tau_0 \omega sin(\omega t) \tag{2.4}$$

so γ and τ are 90° out of phase, figure 2.5. Anything with a phase angle of $0° < \delta < 90°$ has both viscous and elastic components The phase angle is only a relative measurement of the elastic and the viscous component, and does not give enough information. We must calculate absolute values for the elastic and viscous components. $G^{'}$ is the elastic modulus

$$G^{'} = \frac{\tau_0}{\gamma_0} cos\delta \tag{2.5}$$

and $G^{''}$ is the storage modulus where

$$G^{''} = \frac{\tau_0}{\gamma_0} sin\delta \tag{2.6}$$

Realistically equation 2.1 for a Maxwell fluid will only be a good approximation within a certain range of τ and γ, called the linear viscoelastic envelope.

2.5.2 Modelling cells in suspension

Viscosity of a solvent can be changed by the dissolving of a solute. Einstein's assumptions lead to equation 2.7 for intrinsic viscosity [Tanner, 2000] [Neuenschwander, 1999], which describes the effect of particles on viscosity.

$$\eta_f = \eta_s(1 + 2.5\Theta) \tag{2.7}$$

Where $\eta_f$and η_s are the viscosity of the fluid and the solvent respectively and Θ is the volume fraction occupied by the particles.

Equation 2.7 is based on identical, neutrally buoyant, inertia-less rigid spheres. The equation is only valid for volume fractions up to 0.03. It also assumes passive particles, which encompasses the following; the particles are not self propelling and particles do not possess dipoles, either magnetic, electrical or gravitational i.e. where the geometric centre and the centre of mass do not coincide. Previous published research tackles some of the assumptions that cannot be applied to cell suspensions, such as Brenner [1970] which explores particles with dipoles, Batchelor [1970] slender particle theory and Hatwalne et al. [2004] model for active particles. Although not originally written with cells in mind, Brenner [1970] models particles that have dipoles. Brenner investigated general dipoles, including magnetic and electrical, but used gravity as the example. The torque produced by the requirement that the dipole and the external field align hinders free rotation. A schematic is shown in figure 2.6. This results in a greater rate of mechanical energy dissipation and, hence, a larger apparent viscosity than would exist in the absence of such couples.

For a bottom heavy particle the apparent viscosity is predicted by equation 2.8.

$$\eta_f = \eta_s(1 + 4\Theta) \tag{2.8}$$

The intrinsic viscosity has been increased from a value of 2.5 in Einstein's correlation to a value of 4. It was then predicted at some critical shear rate $\dot{\gamma}_c$ the torque is overwhelmed, and the spheres begin to rotate freely.

$$\dot{\gamma}_c = \frac{\rho g h}{3\eta_s} \tag{2.9}$$

where ρ is density. The assumption that the particles are neutrally buoyant still holds,

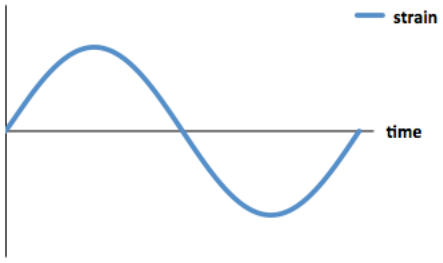

(a) strain wave imposed in the material

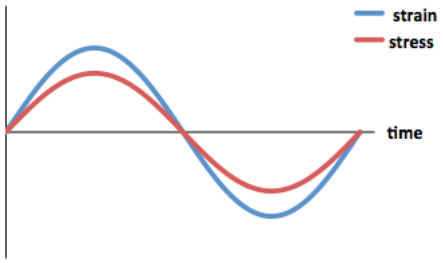

(b) The in-phase stress reaction from a Hookean solid

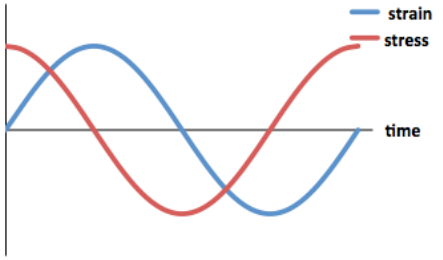

(c) The 90° out of phase reaction of a Newtonian fluid

Figure 2.5: Strain responses to sinusoidal stress of a Newtonian liquid and a Hookean solid

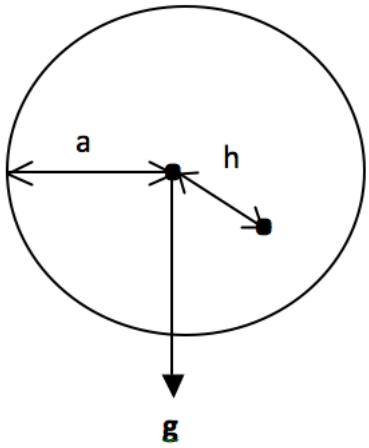

Figure 2.6: Bottom heavy particle. a is the radius, g is the direction of gravity, h is the distance between the geometric centre and the centre of mass. Reproduced from Ishikawa [2009]

so there is no difference in the fluid density and the particles density. As $\dot{\gamma}$ is increased and becomes larger than $\dot{\gamma}_c$, η_f decreases rapidly, asymptotically approaching the limiting value of $\eta_f = \eta_s(1 + 2.5\Theta)$

This has been applied by Ishikawa et al. [2006] to algae cells. Certain motile algae cells are bottom-heavy, enabling them to swim on average vertically upwards in still water. This bottom-heaviness provides the cell with a self righting mechanism causing it to move in the preferred direction even if temporarily rotated by flow.

Most fundamental studies consider suspensions of monodisperse spheres. This assumption is not always applicable to cell suspensions.

Extensional flow can be imagined as a rod of material being extended homogeneously along its x-axis. Although some cells are spherical e.g. *Nannochloropsis* sp., many are not such as *E-coli* which are rod shaped. Systematic data on semi-dilute and concentrated systems with well-defined shapes other than spheres is still quite rare Mewis and Wagner [2009]. Long slender particles have been considered by Batchelor [1970]. These particles were straight and rigid and had a length that was large compared to its breath, but had an arbitrary cross section. Lubansky et al. [2005] extend Batchelor's theory to more specific shapes, either ellipsoidal or cylindrical particles, and improves the predictive capability of Batchelor's theory when compared with measurements found in the literature for different rod-like polymer solutions. It should also be mentioned that the effect of the type of flow, e.g. shear flow versus extensional flow, could be extremely pronounced with non-spherical particles. Only limited data of this nature is available for well-defined systems.

A few theoretical and computational models have also been developed to predict the effective rheology of active suspensions. Hatwalne et al. [2004] considered the hydrodynamics of particles that exert a force on the ambient fluid. Again his theory was not specifically for cells but made interesting predictions that other numerical and experimental papers have, somewhat, confirmed. Hatwalne's model predicted an effective increase in viscosity for 'puller' particles but a decrease in viscosity for 'pushers'. Hatwalne seemed unaware that

this describes algal cells and bacteria respectively.

Ramaswamy [2010] explains the mechanism by which motile cells affect viscosity figure 2.7. *Consider a collection of filaments endowed with contractile or extensile force dipole. A modest imposed shear flow. Contractile filaments will then pull back on, and extensile filaments push out on, the flow that oriented them. The result is a higher stress/rate ratio, that is, a viscosity, for contractile filaments, and lower for extensile filaments*

The effect of pusher and puller microorganisms on viscosity has been confirmed by two experimental papers. Sokolov and Aranson [2009] is the first published paper to have taken direct measurements of shear viscosity of bacterial suspensions. *Bacillus subtilis* was centrifuged and resuspended in clean media. The viscosity was probed directly by measuring the viscous drag exerted on a rotating magnetic particle. They estimated that the viscosity for suspensions of motile *Bacillus subtilis* was reduced by up to a factor of seven compared to that of a suspension of non motile *Bacillus subtilis*. Rafai et al. [2010] uses a rheometer to measure the viscosity of suspensions of *Chlamydomonas Reinhardtii*, a motile microalgae. After being grown for two days the cells are centrifuged and resuspended in fresh media. It's confirmed that puller microbes increase the viscosity. This is also recognized by Ewoldt et al. [2010]. Shear thinning was observed Rafai et al. [2010], as predicted by Hatwalne et al. [2004]. However, Rafai et al. [2010] tried to develop a hypothesis based on Brenner [1970] bottom heaviness to explain the shear thinning observed. It is not unusual for photosynthetic algae to have an asymmetric mass distribution to act as a primitive gravity sensing device, to cause the organism to swim vertically upwards Pedley and Kessler [1992]. For *Chlamydomonas Reinhardtii* the gravitational and geometric centres do not coincide, so there will be some torque developed when a flow is applied.

However, it should be noted that a calculation on a very slightly eccentric particle shows that the critical torque is exceeded for all of the data presented in Rafai et al. [2010]. $\dot{\gamma} = 2.97s^{-1}$ the lowest value for strain rate in Rafai's et al. paper was 4 s^{-1}, so there is no data for the cells whilst they are still resisting rotation. If this cell suspension was to follow

Brenner's predictions the shear thinning observed would plateau at shear rates above $\dot{\gamma}_c$ to an apparent viscosity that corresponds to an intrinsic viscosity of 2.5. The plateau at high shear rates in Rafai et al. [2010] work corresponds to an intrinsic viscosity of 4.5. Brenner [1970] work is not applicable, because live cells are not passive; they are motile and exert a stress on the fluid. Dead cells have an intrinsic viscosity of 2.5 ± 0.1 [Rafai et al., 2010] presumably acting as passive particles.

2.5.3 Modelling bubbles within whole cell culture

Characterising the rheology of whole cell algae samples straight from the reactor without cleaning or purification is important in understanding how to optimise growth conditions. To date current research has only recorded data for cells that have been centrifuged and re-suspended in clean media (Sokolov and Aranson [2009] and Rafai et al. [2010]). This however does not give an insight into the rheology of whole cell cultures; the fluid as it is in the reactor including cells, broken and dead cells, media, extracellular polymers and contaminates. Chapter 4 investigates the rheology of whole cell culture, straight out of the flask with no processing.

The efficiency of growing algae is strongly affected by nutrient and CO_2 availability, heat distribution and mixing. Aeration is the most common method of satisfying these four requirements. Bubbles rising through the bioreactor culture will impose a shear rate and as whole cell culture does not display a Newtonian nature, apparent viscosity depends on this shear rate.

Hayashi and Tomiyama (2009) argue that for a single spherical bubble in a pure system the drag coefficient, $C_{(D_0)}$is

$$C_{(D_0)} = 16/Re \tag{2.10}$$

where Re is the Reynolds number given by $Re = \frac{\rho u d}{\mu}$.

This is valid for intermediate Reynolds numbers, $0.083 < Re < 200$. Wallis [1969] gives

a more comprehensive guide to bubbles of all sizes and therefore Reynolds numbers and is summarised in table 2.1.

	Terminal Velocity	Range of applicability
Region 1	$u_{b_\infty} = \frac{2a_b^2(\rho_f - \rho_g)}{(9\mu_f)}$	$Re_b < 2$
Region 2	$u_{b_\infty} = 0.33g^{0.76}\frac{\rho_f}{\mu_f}^{0.52}a_b^{1.28}$	$2 < Re_b < 4.02G_1^{-2.214}$
Region 3	$u_{b_\infty} = 1.35\frac{\sigma}{\rho_f Re_b}^{0.50}$	$4.02G_1^{-0.214} < Re_b < 3.10G_1^{0.025}$ or $16.32G_1^{0.144} < G_2 < 5.75$
Region 4	$u_{b_\infty} = 1.18\frac{g\sigma}{\rho_f}^{0.25}$	$3.10G_1^{-0.25} < Re_b$ and $5.75 < G_2$

Table 2.1: Terminal velocity of single gas bubbles in liquids reproduced from Wallis [1969]

Where

$$G_1 = \frac{g\mu_f^4}{\rho_f\sigma^3} \tag{2.11}$$

$$G_2 = \frac{ga_b^4u_{b_\infty}^4\rho_f^3}{\sigma^3} \tag{2.12}$$

Where g is gravitation field, a_b is bubble radius, u_b is bubble rise velocity, u_{b_∞} is terminal bubble rise velocity, Re_b is the Reynolds number of a rising bubble and ρ_f and ρ_g are the densities of the fluid and the gas respectively. Regions 1 to 4 describe bubbles getting progressively bigger in diameter. Wallis [1969] explains that for small bubbles the effects of surface tension and viscosity are important. However, for very large bubbles the effects of surface tension and viscosity are negligible.

2.6 Cells and stress

Shear stress within bioreactors can have a positive effect [Merchuk, 1991]. Heat and mass transfer are increased with convective mixing, which improves cell kinetics. They would otherwise rely on molecular mechanisms, which are slow in comparison.

However, excessive shear can damage suspended cells, leading to a loss of viability and even disruption. Merchuk [1991] summarises the interrelationship of cell kinetics and shear

in a bioreactor in figure 2.8. The viscosity of the whole cell culture in a reactor affects the fluid dynamics induced from mechanical agitation.

What constitutes the limit of positive effects of shear within a system is very variable. Turbulent eddies within the flow have been shown to be problematic, but the length scale of the eddies relative to the cell size is important. If a relatively large eddy forms in a region occupied by a suspended cell, the cell will be entrained and rotate and translate to reduce the net forces on its surface. However, for very small eddies the motion of the cell is limited and they experience more of the full force of the eddy [Croughan et al., 1987]. Croughan et al. [1987] recommends careful scale up from laboratory to industry scale, using power input per unit volume to avoid turbulent eddies of a detrimental characteristic length scale. However, optimising length scales of eddies alone is not enough to ensure cell damage is minimal. Cells of a similar culture can react very differently to the same level of shear. As such the following summaries are very general.

High shear influences the morphology of single celled microorganisms. For example *Aspergillus flavius* forms much shorter and highly branched mycelium [Merchuk, 1991]. Metabolite production is also altered, although it is unclear whether this is a direct result of shear on cells, or a by product of the morphology changes.

Plant cells are sensitive to shear because of their size; they are larger, so damage is expected at larger eddy sizes. Scragg et al. [1988] found that resistance to shear was not a fixed characteristic, and for certain cell lines of *Helianthus annuus* shear tolerance can develop when cultured under shear conditions. It's unclear whether the mechanism for this tolerance is because shear tolerance is not homogeneous throughout the culture; so the less tolerant cells are damaged and no longer able to replicate themselves, resulting in "survival of the most tolerant". Alternatively, it could be that the shear induces increased production of a metabolite that protects the cells.

Mammalian cells are particularly sensitive to shear as they do not have a rigid cell wall for protection like bacteria or plant cells. Under high shear, mammalian cells adopt an

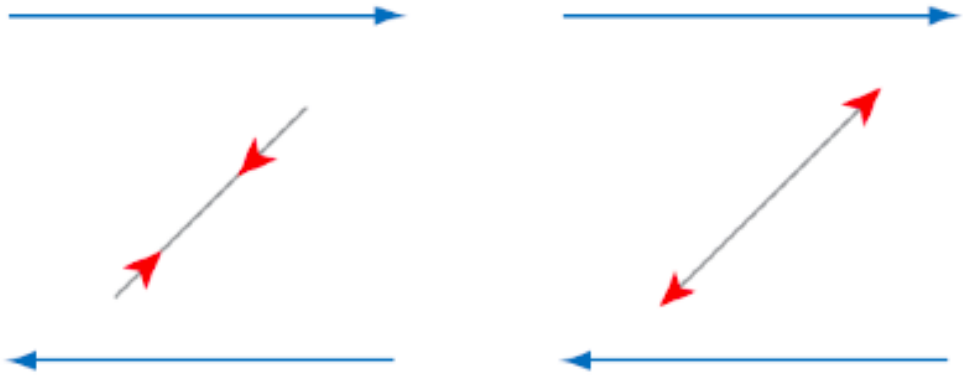

Figure 2.7: How activity affects shear. As a shear is applied, filaments line up, and either pull back or push out. Reproduced from Ramaswamy [2010]

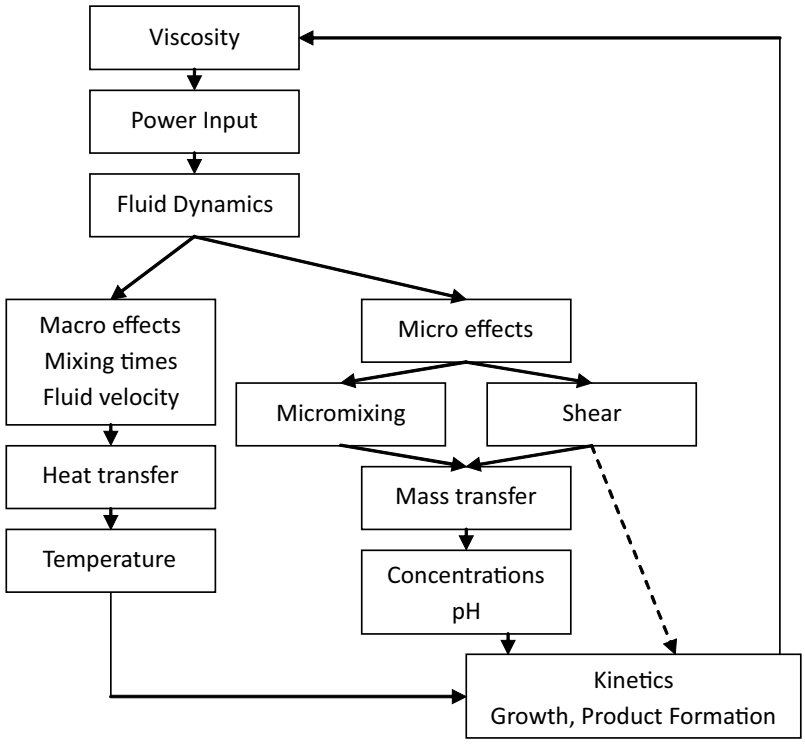

Figure 2.8: Interactions between fluid dynamics and kinetics in bioreactors, reproduced from Merchuk [1991]

elongated form and align themselves in the direction of flow [Croughan et al., 1987, Metallo et al., 2008]. Mammalian cells are so sensitive to shear, that surface aeration is preferred rather than sparging. A whole range of bioreactors have been developed that facilitate mass transfer without sparging. Zhang et al. [2008] developed shaken helical track bioreactors for Chinese Hamster Ovary cells. These are cylindrical vessels with a helical track on the inside wall.

Merchuk [1991] suggested that shear may directly affect cells and must be considered as one of the potential variables in the kinetic formulation of growth and product formation. This is represented as the dotted line in figure 2.8. But Merchuk [1991] highlights the almost total lack of information in this area. To the best of the author's knowledge none of the literature citing Merchuk [1991] has responded to the suggestion and investigated the direct affect of stress on cell kinetics.

Species specific tolerance of shear is shown by Chengala et al. [2010] study of *Dunaliella* and *Selenastrum*. Both are unicellular green algae, *Dunaliella* is motile, whilst *Selenastrum* is non-motile. It was found that small scale velocity gradients facilitate the accumulation of Selenastrum but inhibited the accumulation *Dunaliella*. Chengala et al. [2010] also investigated the kinetic responses of *Dunaliella* in moving fluids. They found that the speed of swimming was affected by the local fluid flow conditions. They also hypothesis that fluid flow *"very likely may"* have an effect on physiology.

Recent research into differentiation of human embryonic stem cells confirms how important shear stress is directly to cells. Metallo et al. [2008] studied the response of human embryonic stem cells. Sheared and static controls were compared. It was found that genes had altered transcription levels in response to applied shear. An applied shear rate changed activity within the cell. Yamamoto et al. [2005] also attest that stress can directly affect cells. Embryonic stem cells were shown to be flow sensitive and their proliferation and differentiation into vascular endothelial cells can be promoted by shear stress. Flow-induced shear can be problematic to cells because shear can affect cells' physical development, growth and

protein expression [Merchuk, 1991, Metallo et al., 2008], flow can affect motility [Kaya and Koser, 2012] and weakly adherent cells are easily displaced by shear [St. John et al., 1994].

2.7 Bioreactor designs used to cultivate algae

On a large scale algae cultures are grown using one of two methods, open ponds or closed bioreactors [Scott et al., 2010, Rawat et al., 2013]. Open ponds are typically a closed loop with recirculation from a paddlewheel, with a typical depth of 0.2 to 0.5 m. If CO_2 requirement is more than surface diffusion can provide, CO_2 sparging may be needed.

Closed bioreactors come in many designs, but they mostly optimise the use of light, by minimising the light path through the culture, thereby maximising the light cells receive [Carvalho et al., 2006, Rawat et al., 2013]. Tubular photobioreactors are regarded as the most suitable for growing algae. Tubular reactors are based on any array of tubes which have a small enough diameter, 15 cm to 20 cm, to allow light to penetrate through the whole culture. Circulation is by airlift pump, centrifugal pumps or bubbles [Brennan and Owende, 2010]. There are many permutations of closed bioreactors for algae culture, including helical tubular reactors that coil the tubes around a light source and horizontal tube reactors that consist of many parallel tubes angled to collect the most sunlight.

Open ponds have the advantage of being cheap to construct, but have the disadvantage of having limited control over the conditions the algae grow in, contamination, high evaporative losses, and the low cell concentration, maximum concentration achievable is 0.25 g l^{-1} d^{-1}, in part due to self shading of cells, meaning extensive land is needed. Closed bioreactors can be accurately controlled for temperature, pH and mixing and sparging can increase exposure to light and an increase in biomass production, of around 2.15 g l^{-1} d^{-1}, but comes at an energy cost. However, the costs of closed systems are substantially higher than open pond systems Carvalho et al. [2006].

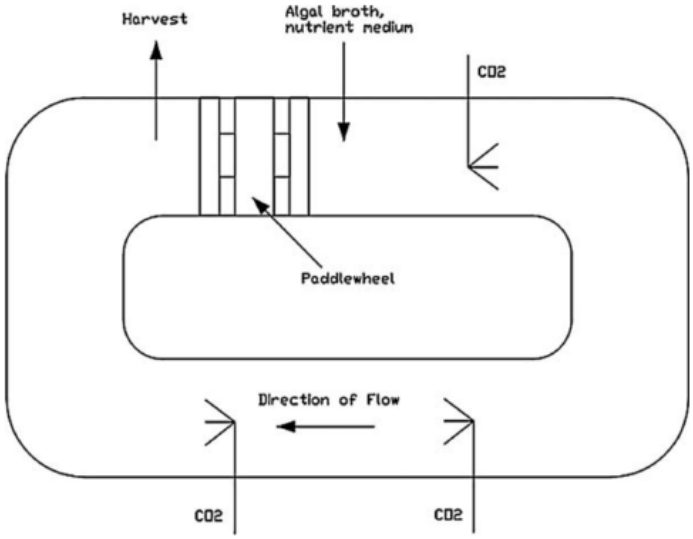

Figure 2.9: Schematic of an open pond used for culturing algae. Reproduced from Brennan and Owende [2010]

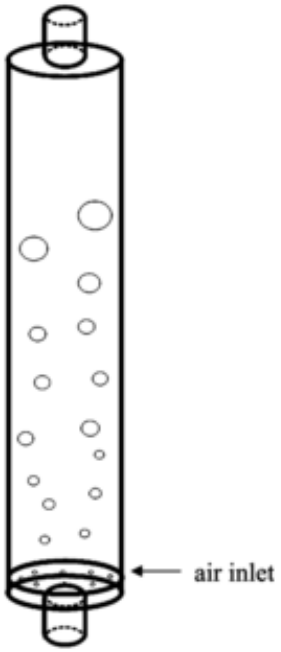

Figure 2.10: Section of a closed tubular photobioreactor. Reproduced from Carvalho et al. [2006].

Chapter 3

Materials and Methods

3.1 Simulations using COMSOL Multiphysics

COMSOL Multiphysics 4.3b (COMSOL AB, Stockholm, Sweden) was used to model the chosen microfluidic channel design shown in figure 3.1, using two physics packages, laminar flow and transport of dilute species. The device was approximated to a 2D system with the following range of dimensions:

- Radius which varied from 100 μm to 1000 μm.
- Inlet width a minimum width of 5 μm.
- The maximum ratio between inlet width and radius was set to 1. As the ratio increases above 1.7, the inlets overlap each other.
- Inlet neck length varied between 0 μm to 80 μm

The following constraints are imposed:

- The fluid is assumed to be water, which is a good approximation of the viscosity and density of many liquid media used in cell growth.
- Two inlets with an input concentration of 0M and one inlet with an input concentration

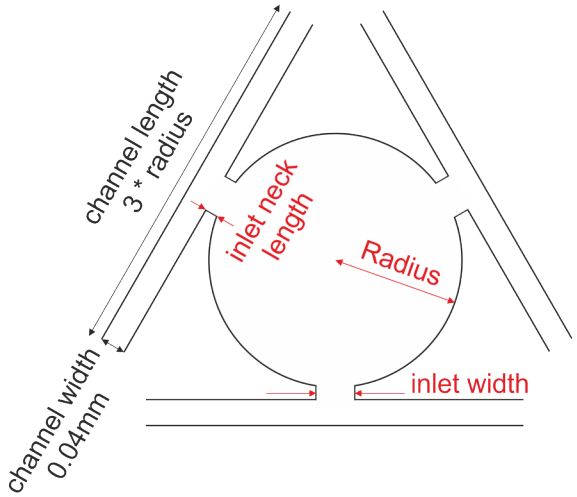

Figure 3.1: The particular geometry used in this study. Measurements specified with a black line are fixed for all simulations. Radius, inlet width and inlet neck length are adjustable lengths, represented by a red line.

set to 1M. It is assumed that the concentration is dilute, so that concentration can be treated as dimensionless.

- The temperature is set to 293.15 K.
- The diffusion coefficient is set to $10^{-9}m^2s^{-1}$, approximately the diffusion coefficient of sugar in water at 293.15 K [Jamshidi-Ghaleh et al., 2004].
- Inlet conditions were fully developed laminar flow.
- Boundary conditions at the wall were no slip and zero pressure at the outlets.
- A physics controlled mesh was chosen, using the preset 'extremely fine' density with a maximum size of $3.76 \times 10^{-5}m$.

The Navier-Stokes equations were used for the flow:

For steady state simulations

$$\rho(u \cdot \nabla)u = \nabla \cdot [-pI + \mu(\nabla u + (\nabla u)^T)], \tag{3.1}$$

$$\nabla \cdot (\rho u) = 0, \tag{3.2}$$

or for transient simulations

$$\rho(\frac{\partial u}{\partial t} + u \cdot \nabla u) = -\nabla p + \nabla \cdot [\mu(\nabla u + (\nabla u)^T)] \tag{3.3}$$

where ρ is the density, u is the velocity vector and p is pressure.

The equations used for transport were:

For steady state simulations

$$\nabla \cdot (-D_i \nabla c_i) + u \cdot \nabla c_i = 0, \tag{3.4}$$

$$N_i = -D_i \nabla c_i + u c_i, \tag{3.5}$$

or for transient simulations

$$\frac{\partial c_i}{\partial t} + u \cdot \nabla c_i = \nabla \cdot (D_i \nabla c_i) \tag{3.6}$$

where D is the diffusion coefficient, c is the concentration of the species and u is the solvent velocity field. Subscript i refers to species i, although in this work only single species diffusion is investigated.

Steady state is defined as 95% of the steady state value obtained from a study using a stationary solver, and is allocated the symbol t_{95}.

3.1.1 Validation of the COMSOL model

2D approximation of a 3D model

It is preferable to run the model in 2D, as it minimises computational time. A preliminary study, using a steady state simulation, was used to check that a 2D model was a good approximation of a full 3D model.

A 3D geometry was created by extruding a 2D geometry with a radius of 100 μm and

inlet width of 30 μm to a depth of 100 μm, so inlet/outlet channels had a rectangular cross-section. All other parameters and package settings were as stated in section 3.1.

The concentration profile in the chamber was used to evaluate discrepancies between the two models. The concentration in the 2D model was evaluated at the points indicated in fig 3.2. These same points were evaluated in three horizontal planes in the 3D model, at a depth of 33 μm, 50 μm and 66 μm. A percentage error between the 2D and each plane in the 3D model for the concentration was calculated for corresponding points. Comparing the three planes from the 3D model also provided a way to study the 2D nature of the chamber.

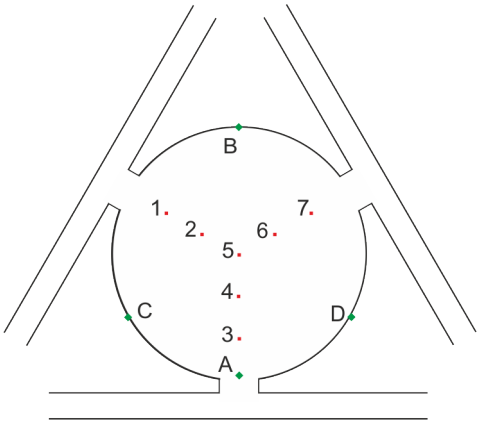

Figure 3.2: Points 1 to 7, which were used as evaluation points to check the validity of the 2D approximation in section 3.1.1. A, B, C and D were used to evaluate the concentration gradient in chapters 5 and 6.

These errors are presented in table 3.1. The discrepancy in concentration profiles from different planes is less than 0.12%, providing evidence that away from upper and lower boundaries, a 3D channel could be approximated by a 2D channel. The 2D model showed an average error of $2.6 \pm 0.3\%$ for all planes of the 3D model.

It has been confirmed that a 2D approximation will model the 3D concentration profile and flow adequately.

Mesh Size

A check of different mesh sizes was made to ensure the simulation results were not a product of the mesh. Figure 3.4 shows a similar concentration profile for 3 different mesh sizes typical of a 2D steady state simulation.

Table 3.2 summarises the comparative computational time for different mesh sizes, and the associated error. Preset mesh densities were tested for accuracy against the most dense mesh, described as 'extremely fine'. Errors were calculated by comparing the concentration at points 1 to 7 (figure 3.2) to the corresponding value of the finest mesh, and taking the sum of the errors squared. Coarser, less dense meshes show an erratic pattern of accuracy, i.e. coarser has an unexpectedly low error. Densities of normal and finer have a steady increase in accuracy. It was found that for a small trade off of computing time (2 seconds), that accuracy was improved between the mesh densities 'extra fine' and 'extremely fine'. Consequently 'extremely fine' meshes were chosen for all simulations.

	Percentage Error						
Depth	1	2	3	4	5	6	7
66 μm	3.07	2.75	1.99	2.36	2.53	2.57	2.79
50 μm	3.16	2.81	1.99	2.39	2.60	2.55	2.76
33 μm	3.02	2.74	1.87	2.41	2.57	2.58	2.72

Table 3.1: Percentage error between 2D model and different depths within 3D. Placement of points 1 to 7 in figure 3.2

	Extremely fine	Extra Fine	Finer	Normal	Coarser	Extra Coarse	Extremely Coarse
Number of elements	38576	34930	13384	3740	1608	1332	993
Time to solve, sec	29	27	12	8	6	7	6
Σ(% error)^2 of extremely fine	-	0.0094%	0.012%	0.022%	0.00049%	4.00%	0.018%

Table 3.2: Errors for different mesh densities for a device with a 100μm radius and a 30μm inlet width

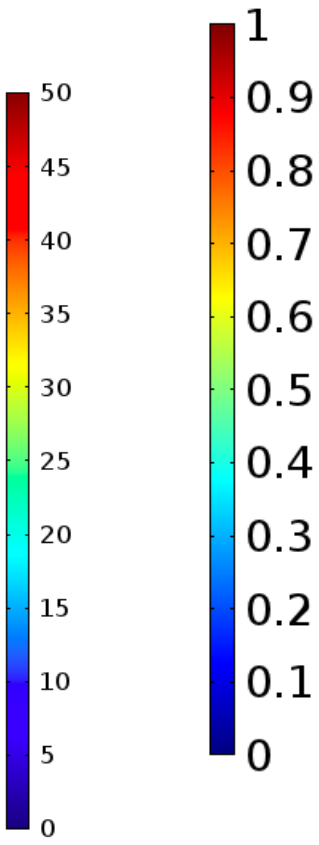

(a) Velocity colour scale, $\times 10^{-6} ms^{-1}$

(b) Concentration colour scale, M.

Figure 3.3: These colour scales for concentration and velocity are used throughout the reporting of results of simulations, in chapters 5 and 6

3.2 Algae and media

All glassware used for making media or culturing was soaked in 3 % Decon solution overnight, scrubbed, rinsed three times with tap water, rinsed three times with DI water to remove any residues of surfactant. They were left to air dry and autoclaved using indicator tape to ensure sterility, to reduce the risk of contamination.

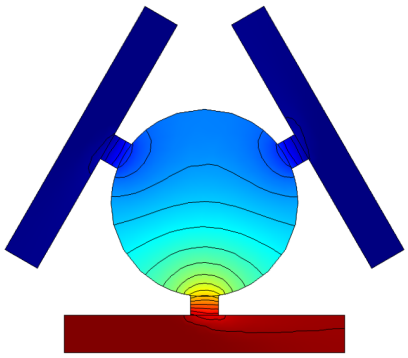

(a) 1000 elements

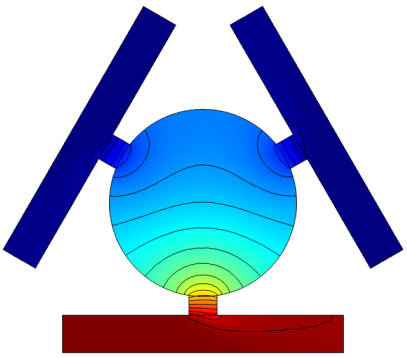

(b) 3700 elements

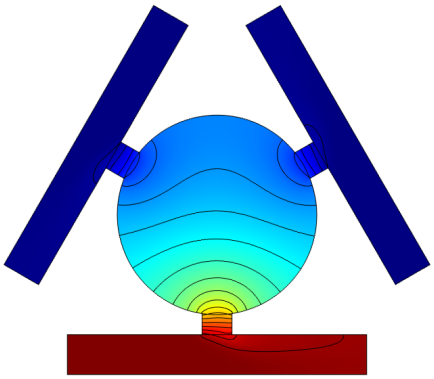

(c) 38500 elements

Figure 3.4: Three different mesh densities, all showing very similar concentration profiles. The finer the mesh, the smoother the profile. Colour legend figure 3.3.

3.2.1 *Nannochloropsis* sp. and *Tetraselmis impellucida*

For the experimental results chapter 4 two algal species *Nannochloropsis* sp. (Nanno) and *Tetraselmis impellucida* (Tetra) were explored purchased. Both are salt water algae.

Tetra was chosen as the *Tetraselmis* sp. is a candidate for producing lipids to be converted into biodiesel [Mata et al., 2010]. It's also a motile algae [Jaouen et al., 1999].

Nanno was chose for its high lipid content, which makes it desirable as a feed stock for biodiesel Chiu et al. [2009].

The algae cultures used in chapter 4 were predominately maintained by Aimee Guha-Roy.

Two algal species *Nannochloropsis* sp. (Nanno) (PLY 588, Plymouth Culture Collection, UK) and *Tetraselmis impellucida*(Tetra) (PLY 429, Plymouth Culture Collection, UK) were explored.

The Nanno was cultured in Erdschreiber's Medium (ES) media; salt water with soil extract and nutrients added. Tetra was cultured in a mixture of 50% ES media and 50% f/2 media. f/2 media is salt water with several nutrient solutions added. The ES media was purchased from Plymouth Culture Collection. The f/2 media is made to CSIRO protocol, in a laminar flow hood. Apart from the differing media they were grown under the same conditions. The incubator (Innova 4230 refrigerated incubator shaker, New Brunswick Scientific) was held at $15°C$ and the 500 ml flasks were swirled by hand once a day. The light source was located at the back of the incubator, so samples were rotated on a daily basis to make sure exposure to light was shared. Estimates of cell concentrations were made using a haemocytometer. Typical culture had a viability of 50 % and a concentration of 20×104 cells/ml which corresponds to a volume fraction of 0.0013 %.

Whole cell samples for rheometry testing in chapter 4 were extracted directly from a freshly swirled flask with a pipette and loaded in the rheometer.

Algae used in chapter 8 were *Tetraselmis* sp., (66/24, CCAP, SAMS Research Services Ltd., Argyll, UK).

Following an incubator failure, it was necessary to incubate the flasks at room temperature on a North facing window sill. They were swirled once a day to mix and re-suspend cells. Cells were found to be difficult to subculture, so were used in motility studies within 2 weeks of purchase.

3.2.2 Making f/2 media

f/2 stock solutions were purchased from CCAP (SAMS Research Services Ltd., Argyll, UK) and diluted to the correct concentrations in artificial sea water (AS). AS is made using DI water and reef crystals aquarium salt at a concentration of 35 g/l. The media was then filtered through a 0.22 μm pore filter under vacuum into sterile media bottles. This media can be stored in the refrigerator for up to 12 months.

The trace elements and vitamins provided by the f/2 stocks are listed in table 3.3.

	per litre
Na_2 EDTA	4.16 g
$FeCl_3.6H_2O$	3.15 g
$CuSO_4.5H_2O$	0.01 g
$ZnSO_4.7H_2O$	0.022 g
$CoCl_2.6H_2O$	0.01 g
$MnCl_2.4H_2O$	0.18 g
$Na_2MoO_4.2H_2O$	0.006 g
Cyanocobalamin (Vitamin B12)	0.0005 g
Thiamine HCl (Vitamin B1)	0.1 g
Biotin	0.0005 g
$NaNo_3$	0.075 g
$NaH_2PO_4.2H_2O$	0.00565 g

Table 3.3: f/2 stocks, amounts to be added to 1 litre of AS

f/2 media with added sodium alginate

1 % w/w sodium alginate was dissolved in warm, approximately 30° C, DI water. Double concentration f/2 media was made and filtered. 1 % sodium alginate was added to double strength media and DI water was added to dilute the salts to the appropriate strength i.e. that of f/2 media and either 0.1 % or 0.4 % alginate.

3.3 Fabricating PDMS Microfluidic devices

The microfluidic devices that were used in chapters 7 and 8 were fabricated from PDMS using soft lithographic methods (McDonald et al. [2000], Weibel et al. [2007], Friend and Yeo [2010]). The devices were designed using CorelDRAW X6 (Corel Corperation, Canada) and several devices with different geometries were printed using a high resolution onto transparent film (Micro Lithography Services Ltd, Essex, UK) with a dark field and bright features to make a mask, figure 3.5. Having several devices on one wafer speeds up fabrication, by creating several devices per PDMS curing. Inlet/Outlet channel lengths were chosen so that needles inserted into the ports were far enough away from the area of interest, so when visualising the finished microfluidic device did not interfere with the microscope condenser.

Negative photoresist SU8 (MicroChem Corp., USA) was applied to a 10 cm diameter silicon wafer. Spin coating was used to get an even 100 μm thick layer. The mask was placed on top of the SU8 coated wafer and the wafer was exposed to UV light for 30 seconds to polymerise the exposed regions. It was then baked and unpolymerised SU-8 washed off with ethanol. Thanks goes to the Prof Dirks Aarts laboratory, Chemistry Department, Oxford, for the use of their facilities. A detailed standard operating procedure (SOP) is in appendix A.

Embossed channels are made by pouring a 8:1 mix of PDMS and curing agent on top of the silicon wafer and SU-8 mould, and placing under vacuum to get rid of air bubbles and cured for 4 hours at 65°, before being peeled off and cut to size. Literature does not properly detail the method of containing uncured PDMS on top of the wafer. Protocol suggestions were using masking tape around the edge of the wafer or a Petri dish with the wafer in the bottom. Masking tape proved to not create a proper seal against the silicon, and leaked PDMS. Retrieving the brittle silicon wafer undamaged from the bottom of a Petri dish filled with cured PDMS was often unsuccessful. Waxed paper, folded into a shallow box secured with masking tape, was most successful at containing the PDMS and peeling back the paper allowed for easy access to the wafer.

Inlet/outlet ports were punched in the appropriate places using a hollow blunt needle. Individual PDMS microfluidic devices, with inlet/outlet ports cored out, were permanently bonded to glass slides by exposure to oxygen plasma. The SOP for plasma cleaning in appendix B.

Preliminary experiments to characterise the chambers had a DI water syringe swapped to one containing food dye, but it was found that the contrast was too low between the water and dilute food dye. Neat food dye had a higher viscosity than water that affected the flowrate in the narrow inlet channels. Microfluidic device characterisation experiments were completed using 1 wt % rhodamine-B. Rhodamine-B was chosen for the large contrast, and the possibility of utilising florescence. For the experiments in chapter 7 fluorescence microscopy was not used; bright field provided enough contrast.

3.4 Experimental characterisation of a maintained concentration gradient

3.4.1 Data acquisition

Data was collected using a computer controlled inverted microscope (Nikon Eclipse TI 2000 Microscope), equipped with a camera. .avi files were obtained using $\times 4$ objective. For the capture of swimming cells the microscope was optimised to maximise frame rate. Cell tracks were analysed using ibidi chemotaxis tool [Asano et al., 2013] and ImageJ [Schneider et al., 2012].

3.5 Rheological characterisation of whole cell cultures

The effective viscosity of whole cell cultures were explored with an Anton Paar MCR 301.

Cone and plate geometry, fig 2.4, for the top rotating plate is usually preferable over the parallel plate geometry because the shear rate is constant throughout the volume of fluid. A

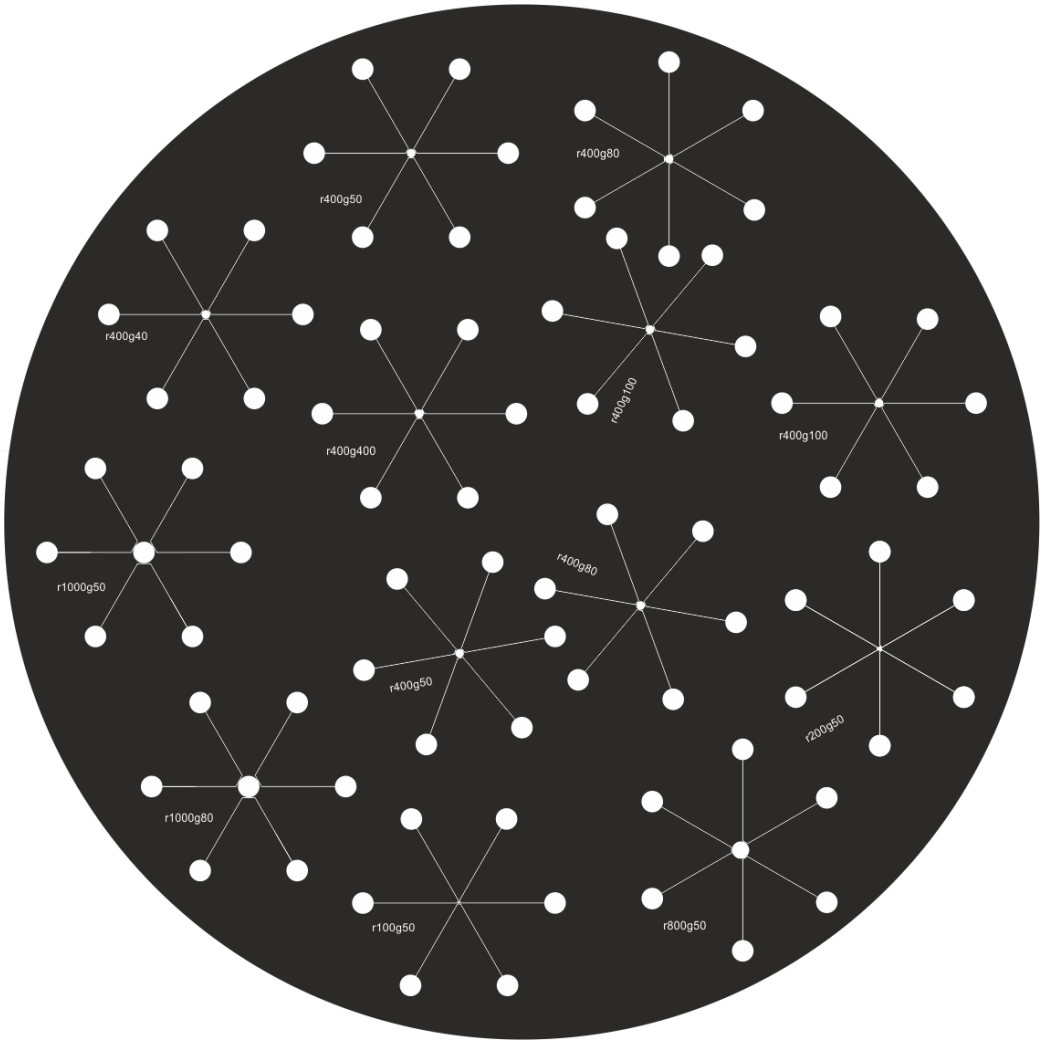

Figure 3.5: This is the design used on the mask that overlaid the SU-8 on the silicon wafer. This mask consists of 13 separate devices, with designs with central chamber radii ranging from 200 μm to 1000 μm and inlet widths from 40 μm to 400 μm. Labels such as r400g50 refer to a radius of 400μm and an inlet width of 50μm

shear stress is imposed by one of the plates rotating and the associated shear rate measured so the apparent viscosity can be calculated, according to $\eta = \tau\ \dot{\gamma}$. However, particulate material in fluids may possibly get stuck on the apex and distort data. This is a problem if the particulate size is in the same order as the gap and a parallel geometry should be chosen. For the results reported in chapter 4 the cells are approximately 30 times smaller than the gap. A 75 mm diameter cone and plate geometry was chosen, with a truncation of 151 μm. Measurements were made at 20 °C. The shear rates were increased from 0.1 s^{-1} to 1000 s^{-1} and decreased back to 0.1 s^{-1} in cycles. Whole cell cultures of Nanno were cycled once and Tetra, were cycled several times.

Chapter 4

Shear Effect of Bubbles Rising Through a Whole Cell Culture

Characterising the rheology of whole cell algae samples straight from the reactor without cleaning or purification is important in understanding how to optimise growth conditions. To date current research has only recorded data for cells that have been centrifuged and re-suspended in clean media [Sokolov and Aranson, 2009, Rafai et al., 2010]. This however does not give an insight into the rheology of whole cell cultures; the fluid as it is in the reactor including cells, broken and dead cells, media, extracellular polymers and contaminates.

Two algal species *Nannochloropsis* sp. and *Tetraselmis impellucida* were explored in this piece of work. Whole cell cultures of both species were subject to rotational rheology.

Bubbles are often use to aerate and agitate cultures. The shear from bubbles, with different radii, rising were theoretically calculated. The shear from the bubbles was compared to the steady shear viscosity of the whole cell algal cultures.

4.1 Modelling bubbles rising through whole cell culture

Mathematica (Wolfram Research, Inc., Illinois) was used to automate calculations of theoretical bubbles rising. Drag co-efficient, C_{D_0}, is described by

$$C_{D_0} = \frac{2f}{A\rho_l u_b^2} \tag{4.1}$$

$$f = 4/3\pi a^3 g\Delta\rho \tag{4.2}$$

$$A = 4\pi a^2 \tag{4.3}$$

Where a is the bubble radius, u_b is the bubble rise velocity, ρ_l is the liquid density, $\Delta\rho$ is the difference between the liquid and the gas density. These equations assume spherical bubbles. Equation 4.1 can be reduced to

$$C_{D_0} = \frac{2a\Delta\rho g}{3\rho u_b^2} \tag{4.4}$$

Hayashi and Tomiyama [2009] report that for spheroid bubbles at intermediate Reynolds number have a drag coefficient

$$C_{D_1} = \frac{16}{Re_b}(1 + 0.15Re_b^{0.687}) \tag{4.5}$$

Where Reynolds number for the rising bubble, Re_b, is

$$Re_b = \frac{(\rho_l u_b a)}{\eta_l} \tag{4.6}$$

where η_l is the viscosity of the surrounding liquid. The predicted limit of validity is $0.083 \geq Re < 200$. $C_{D_0}/C_{D_1} = 1$ was solved for u_b for a = 1 mm, 5 mm, 10 mm, 50 mm and

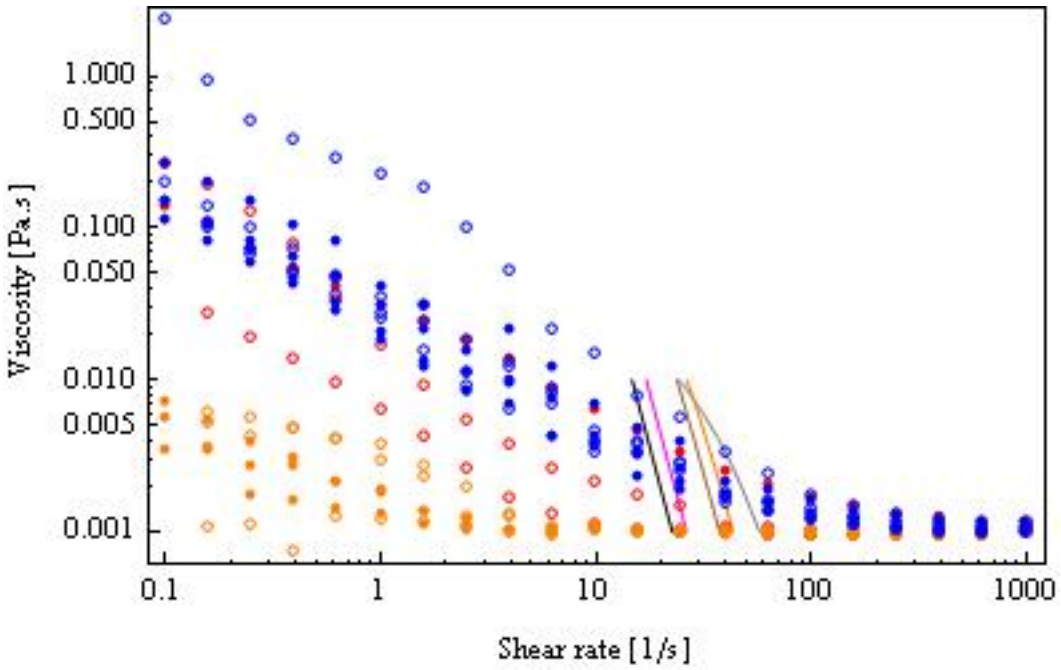

Figure 4.1: Shear thinning of a whole cell Tetra culture. Red orange and blue show sample 1, 2 and 3 respectively. Open symbols show the viscosity whilst the shear is being increased, closed symbols whilst the shear is being decreased. Solid lines represent the modelled imposed shear rate of a rising bubble of different diameters, black 100 mm, pink 50 mm, brown 10 mm, orange 5 mm and grey 1 mm

100 mm, and for η_l between 0.001 and 0.1 Pas. The Mathematica code used for these calculations is in appendix C.

4.2 Results

Figures 4.1 and 4.2 show the viscosity of the Tetra and Nanno suspensions at different shear rates. The theoretical shear rates imposed by different sized bubbles are indicated by the solid lines.

4.2.1 Rheology of whole cell culture

Shear thinning is the general trend observed for both whole cell cultures, plateauing at 0.001 s^{-1}. This was also observed for an algae suspension by Rafai et al. [2010]. Rafai et al. attributed this shear thinning to a phenomena first described by Brenner [1970], that

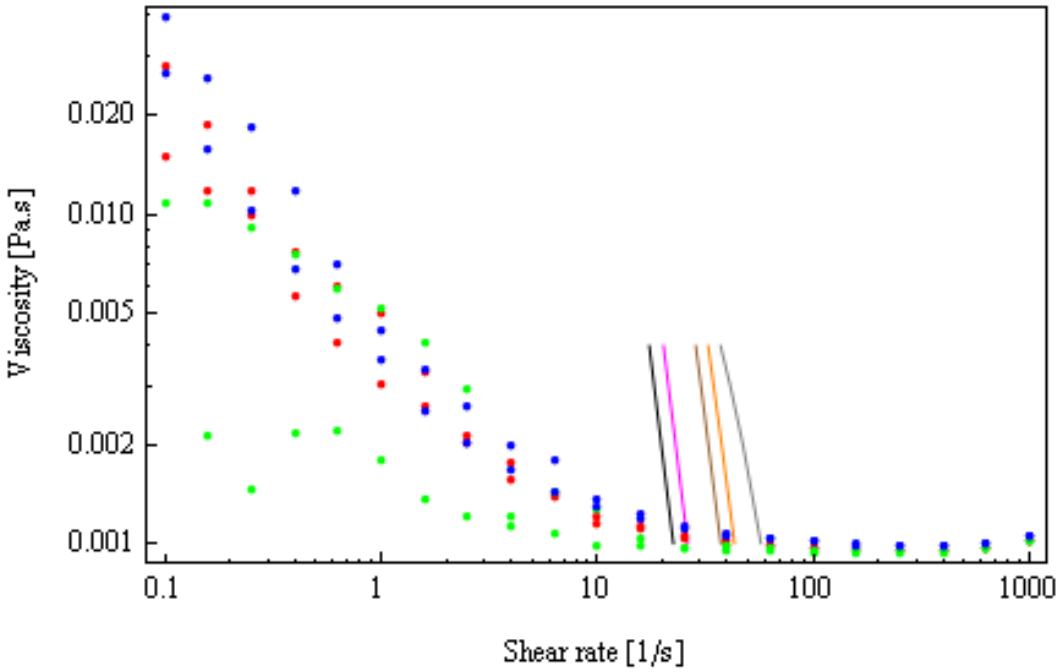

Figure 4.2: Shear thinning of a whole cell Nanno culture. Red, orange and blue show samples 1, 2 and 3 respectively. Open symbols show the viscosity whilst the shear is being increased, closed symbols whilst the shear is being decreased. Solid lines represent the modelled imposed shear rate of a rising bubble of different diameters, black 100 mm, pink 50 mm, brown 10 mm, orange 5 mm and grey 1 mm.

bottom heaviness causes hindered rotation which results in a viscosity equal to equation 4.7,

$$\eta_f = \eta_s(1 + 4\phi) \tag{4.7}$$

until a critical shear is exceeded, and then the viscosity falls to that described by Einstein [Neuenschwander, 1999] in equation 4.8.

$$\eta_{fcrit} = \eta_s(1 + 2.5\phi) \tag{4.8}$$

However, as discussed in chapter 2, Brenner [1970] is not applicable. Shear rates of less than 3 s^{-1} should correspond to a plateau described by equation 4.7. However, Rafai et al. [2010] already shows shear thinning, and at high shear rates corresponds to an intrinsic viscosity of 4.5 instead of 2.5.

The volume fraction is so low in the suspensions of Tetra and Nanno, less than 0.002 % used in this experiment, there is only a 0.2% difference between η_f and η_{fcrit}. This would be indistinguishable from each other particularity over the noise of the experimental data.

This only strengthens the argument for Brenner [1970] work not being a significant factor in the shear thinning. If it was, the viscosity at low shear rates would be indistinguishable from the shear at high shear rates. As figure 4.1 and figure 4.2 show, the fluid is sensitive to shear rate displaying a range of different apparent viscosities over orders of magnitude.

The whole cell culture of Tetra exhibits hysteresis in figure 4.1. Hysteresis occurs due to structural changes in the material when an increasing and then a decreasing shear rate are applied Tanner [2000]. Usually as the shear is increased the structure is degraded, leading to a comparative reduction in viscosity when the shear is decreased. This is the plausible explanation for the hysteresis observed in the Tetra samples.

However, samples 1 and 3 for the Nanno showed a converse situation. The viscosity during loading i.e. that is as the shear is increased, is lower compared to the unloading, during which the viscosity increased. Adesanya [2010] suggests increasing shear can induce gradual

changes in the aggregate structure. Aggregation of the cells may increase the viscosity.

Small shear rates can go below the sensitivity of the equipment, which can result in noisy data. It is a possible explanation that the hysteresis trend observed is just a product of noisy data. However, it is observed in 2 of the 3 samples of Nanno. The increasing stress may have encouraged the cells to align and form a structure, that would increase the viscosity on the unloading.

4.3 Theoretical shear rate from bubbles rising through whole cell culture

The solid lines on the figure 4.1 and figure 4.2 indicate the calculated shear rate from bubbles rising through the cell suspension using the method described in section4.1 and the Mathematica code in appendix C. As indicated in the methods, bubbles of different sizes impart different shear rates. Figure 4.2 shows that apparent viscosity of Nanno suspension is independent of bubble diameter. Bubbles rising of any diameter, have a shear rate above 20 s^{-1}, and is in the region where the apparent viscosity of the whole cell culture has plateaued. No matter what the bubble size the viscosity of the media surrounding the bubbles corresponds to approximately $0.001s^{-1}$.

Figure 4.1 shows the Tetra sample has a bigger variation in viscosity at all shear rates. Some data sets take longer to plateau. This means that the theoretical shear from bubbles of different diameter have been shown to induce different apparent viscosities.

4.4 Conclusions

The apparent viscosity of whole cell cultures of Nanno and Tetra was measured using rotational rheometry. Hysteresis was observed in both Nanno and Tetra cultures; Nanno showed an increase in viscosity during the loading. All samples showed shear thinning behaviour, but the mechanism of this behaviour is unclear. The shear caused by bubbles rising through

a whole cell culture has been modelled. When aerating bioreactors for algae it is concluded that bubble size is not an important factor when trying to predict shear rate viscosity. Viscosity change from the shear input from bubble rising is 10^{-3} Pas to 10^{-2} Pas for Tetra suspensions and negligible for Nanno suspensions.

Chapter 5

Designing and Characterising a Microfluidic Device for a Controlled Concentration Gradient

In section 2.5.2, it was discussed how the motility of cells can affect the rheology of a suspension of cells, and chemo-effectors, chemicals that induce chemotaxis in cells, is identified as a way of manipulating cell movement. Both of these, motility within media, and chemotatic movement could be explored using the device detailed in this chapter. The geometry of the device used is in fig 5.1(a), and inlet/outlet ports are arranged as in fig 5.1(b). The central chamber is served by three inlet/outlet channels within which flows a solution which is diffused into the central chamber via the inlets. Diffusive dominant transport is desirable if studying motile cells, which are unable to actively swim above a critical flow rate and instead tumble and move with the convective flow. This chapter seeks to theoretically characterise the effects of geometry and design on performance.

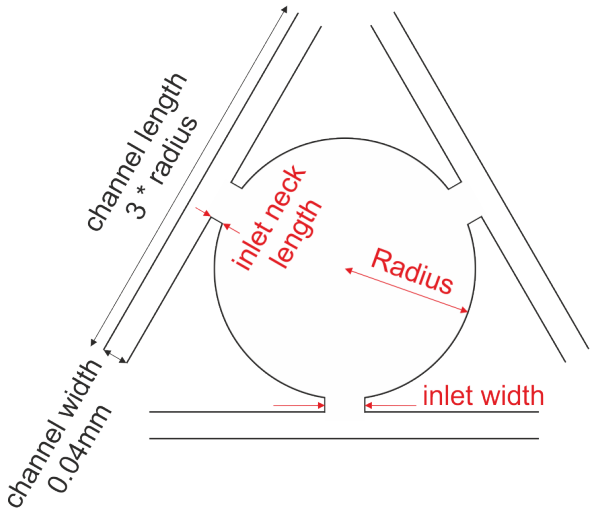

(a) Schematic of microfluidic channel. Measurements specified with a black line are fixed for all simulations. Radius, inlet width and inlet neck length are adjustable lengths, represented by a red line.

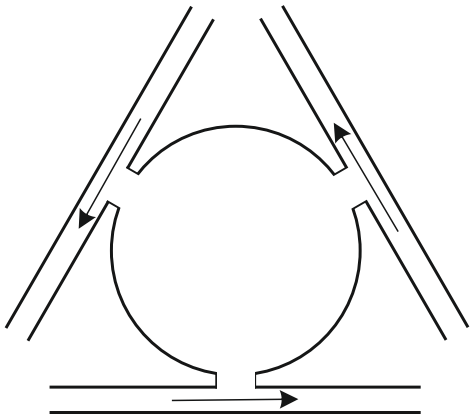

(b) Arrangement of the inlet channel flows

Figure 5.1: The design of the microfluidics device used in the COMSOL models

The effect of the diameter of chamber, inlet width and inlet neck length on the time to reach steady state, the flow profile and the shape and range of the concentration gradient have been explored. The geometry has been optimised for the desired outputs. With a view to fabricating a device for uses in practical experiments, a case study will be provided optimising for short steady state times. For studying cell motility in mind, low convective flow is desirable, and for the study of chemotaxis a symmetrical concentration gradient that has a large range would be suitable.

5.1 Time to reach steady state

It may be desirable to ensure that equilibrium times within the device are much shorter than the characteristic process times of the subject being studied. It may also be desirable to minimise the time to reach steady state to minimise experiment duration. Steady state is defined as 95% of the steady state value obtained from a study using a stationary solver, and is allocated the symbol t_{95}.

5.1.1 Effect of radius on time to reach steady state

The times to reach steady state at the centre of chambers with the same inlet width and increasing radius were compared. An inlet width of 50 μm was chosen for a range of radii, from 100 μm to 500 μm. An inlet width of 240 μm was chosen for a range of radii, from 500 μm to 1000 μm. The steady state times are plotted on figure 5.2, which shows that an increase in radius increases the time to steady state with a linear relationship between $log(r)$ and $log(t_{95})$, where r is radius and t_{95} is the time to reach steady state as defined in section 3.1. A gradient of 2 for equations for the lines of best fit confirms that the model performed as expected and adheres to the Einstein-Smoluchowski relation $D = d^2/2\tau$ where D is the diffusion coefficient, d is the distance and τ is a time step Atkins [1982], showing that the transport into the chamber is predominately diffusion controlled. However, the result shown here is 2.1, which might be an indicator that there is a small amount of convective transport into the central chamber. Convective flow within central chambers is looked at in section 6.1.3.

5.1.2 Effect of inlet width on time to steady state

Figure 5.2 also indicates that inlet width affects time to reach steady state. A central chamber with a radius of 500 μm takes 1150 seconds and 340 second to reach t_{95} for inlet widths of 50 μm and 240 μm respectively.

Figure 5.3 shows as inlet width increases, time to steady state decreases - a wider inlet

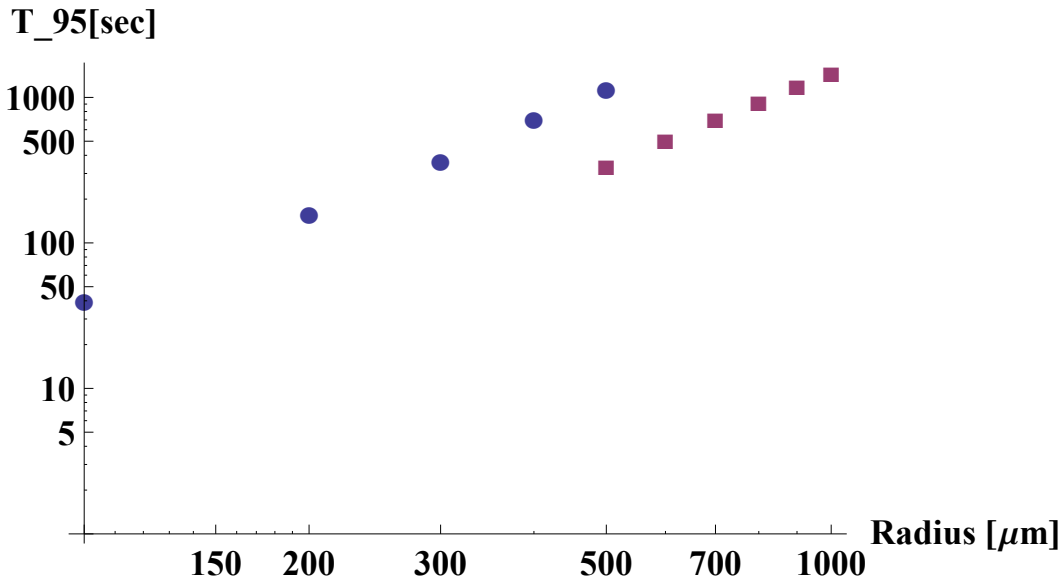

Figure 5.2: The effect of radius size on equilibrium time at the centre of the chamber. Circles : 50 μm inlet, Squares : 240 μm inlet. The equations for linear regression are $log(t_{95}) = 2.1log(r) - 1.14$ and $log(t_{95}) = 2.1log(r) - 2.5$.

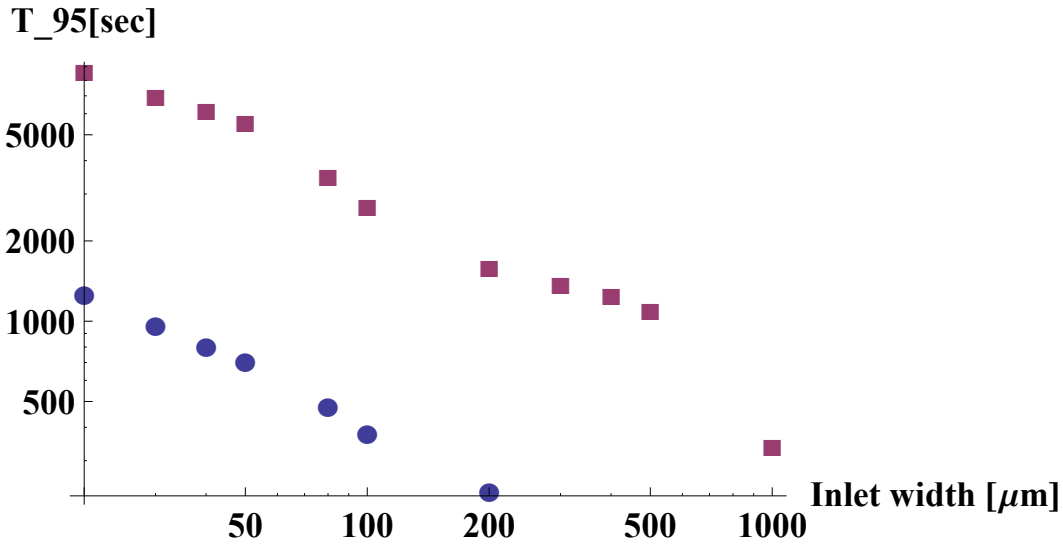

Figure 5.3: The effect of inlet width on equilibrium time at the centre of the chamber. Circles: 400 μm radius, squares: 1000 μm radius

allows more transport with a dependency on inlet width of 0.75.

5.1.3 Effect of inlet neck length on time to reach steady state

The inlet neck length was varied from 0 μm to 80 μm on devices with a central chamber radius of 400 μm and a variety of inlet widths. The effect of inlet neck length on the time to t_{95} is shown in figure 5.4. Having a small inlet neck length reduces the time to reach steady state. The effect is more pronounced for narrower inlets. A longer length of neck is an extra resistance to the mass transport.

How the ratio of the inlet width to the length relates to t_{95} is shown in figure 5.5. For inlets with an aspect ratio of below 2, a small decrease in the aspect ratio has a significant effect on the increasing t_{95}. Figure 5.6(a) demonstrates that there is low convective flow within the central chamber, so mass transport to the centre is diffusion dominated. At inlet aspect ratios above 2, there is little decrease in t_{95} with increasing aspect ratio. Figures 5.6(b) and 5.6(c) show that convective transport have become dominant.

It is recommended, for applications that require low convective flows within the central chamber, that the aspect ratio of the inlet is kept below 2. However, any decrease below 2 should be considered against the steep increase in t_{95}.

5.2 Characterisation of the concentration profile within the central chamber

The geometry of the device affects the concentration profile within the chamber. Steady state simulations were used to explore the concentration profile under different conditions. Figure 5.7 shows the concentration profile with changing inlet width. Inlet width affects both the range and the symmetry of the concentration profile.

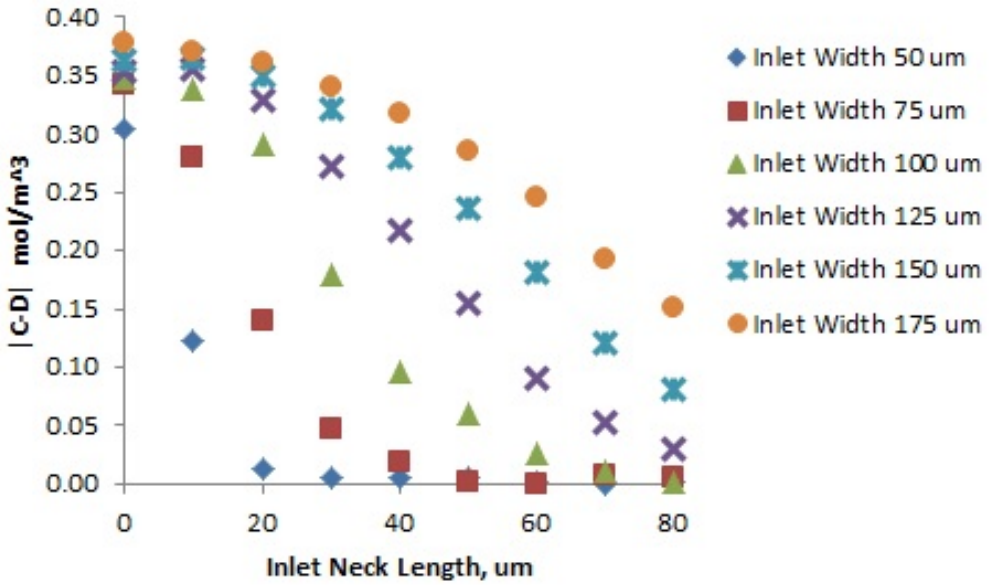

Figure 5.4: The effect of changing inlet neck length on the time to reach steady state, for inlet widths of 50 μm, 75 μm, 100 μm, 125 μm, 150 μm and 175 μm

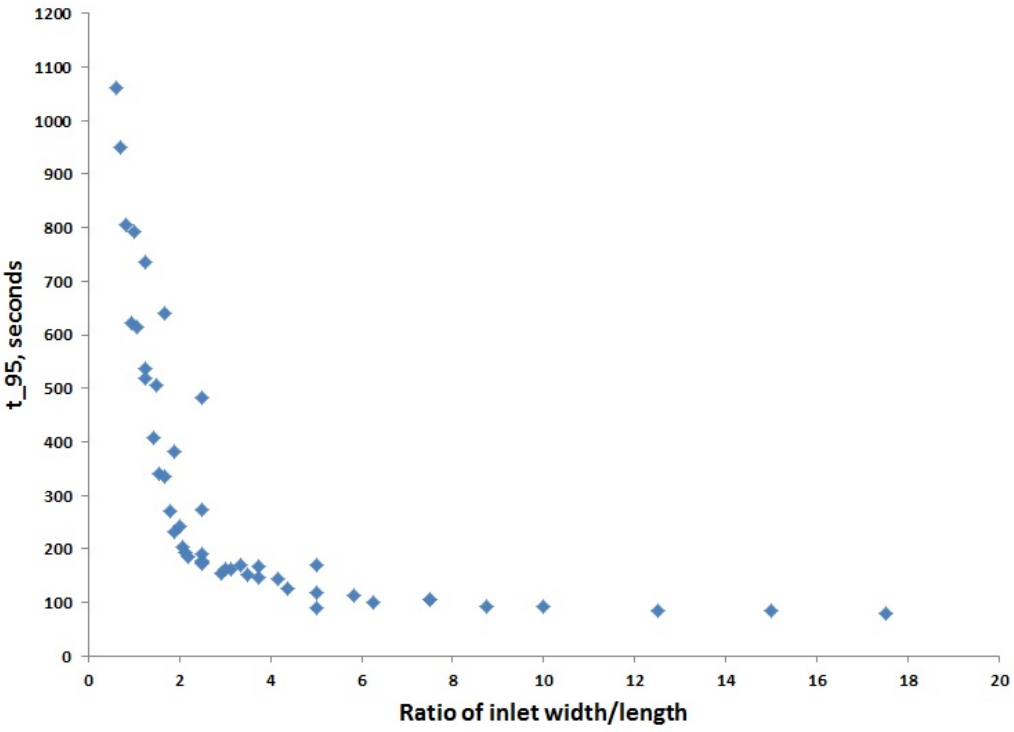

Figure 5.5: Aspect ratio of the inlet

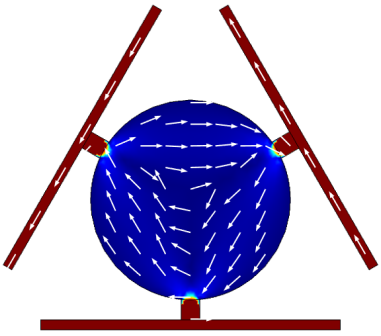

(a) Inlet aspect ratio of 0.94

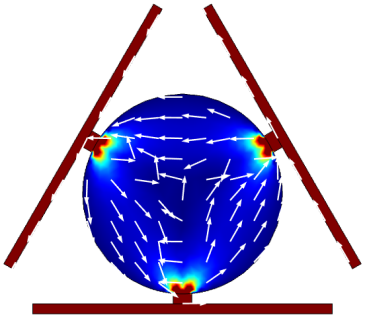

(b) Inlet aspect ratio of 1.88

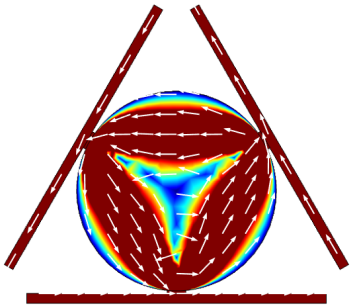

(c) Inlet aspect ratio of 7.5

Figure 5.6: As the aspect ratio of the inlet increases, the convective transport becomes dominant.

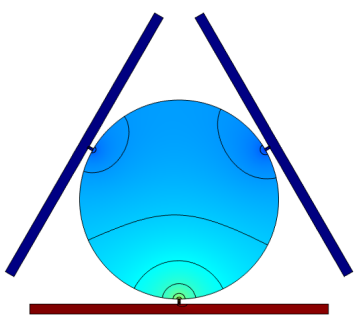

(a) Inlet width 10μm

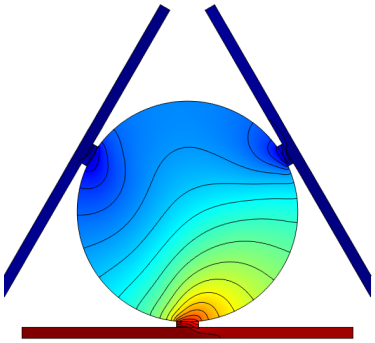

(b) Inlet width 80μm

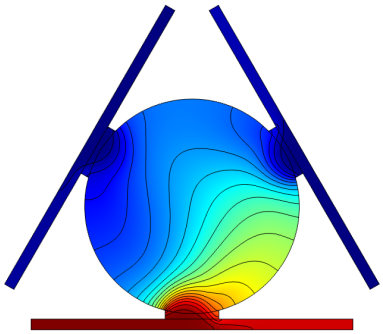

(c) Inlet width 200μm

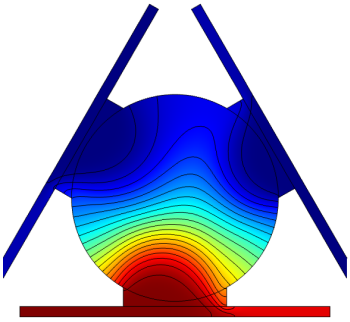

(d) Inlet width 400μm

Figure 5.7: Chambers with a radius of 400 μm. Inlet width changes the characteristics of the concentration profile.

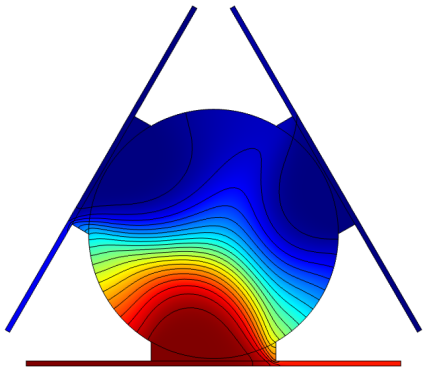

Figure 5.8: Concentration profile within a central chamber with a radius of 1000 μm, an inlet width of 1000 μm and an inlet length of 10 μm

5.2.1 Concentration range

In sections 5.2.1 and 5.2.2 the height of the inlet is 10 μm.

Within the central chamber, it is possible to manipulate and maintain a concentration gradient. For studying the effect of different concentrations of a chemo-effectors on the chemotaxis of cells, it may be desirable to have as wide a concentration range as possible within the central chamber.

Figure 5.9 shows the concentration range is largely insensitive to radius length. Above a radius of 400 μm the concentration range within the central chamber remains stable. However, inlet width does affect the concentration range for radii below 400 μm. The larger the inlet width the greater the concentration range. The concentration range for an inlet width of 1000 μm has the same range as 800 μm, suggesting there is a limit to inlet width affecting the concentration range.

5.2.2 Concentration profile symmetry

Symmetry of the concentration gradient within the central chamber is a desirable trait.

Figures 5.7 also demonstrates the asymmetry that arises as the inlet width increases.

A representative value of symmetry was calculated by taking a numerical difference of the concentration between points C and D, as indicated on figure 3.2, and are plotted on

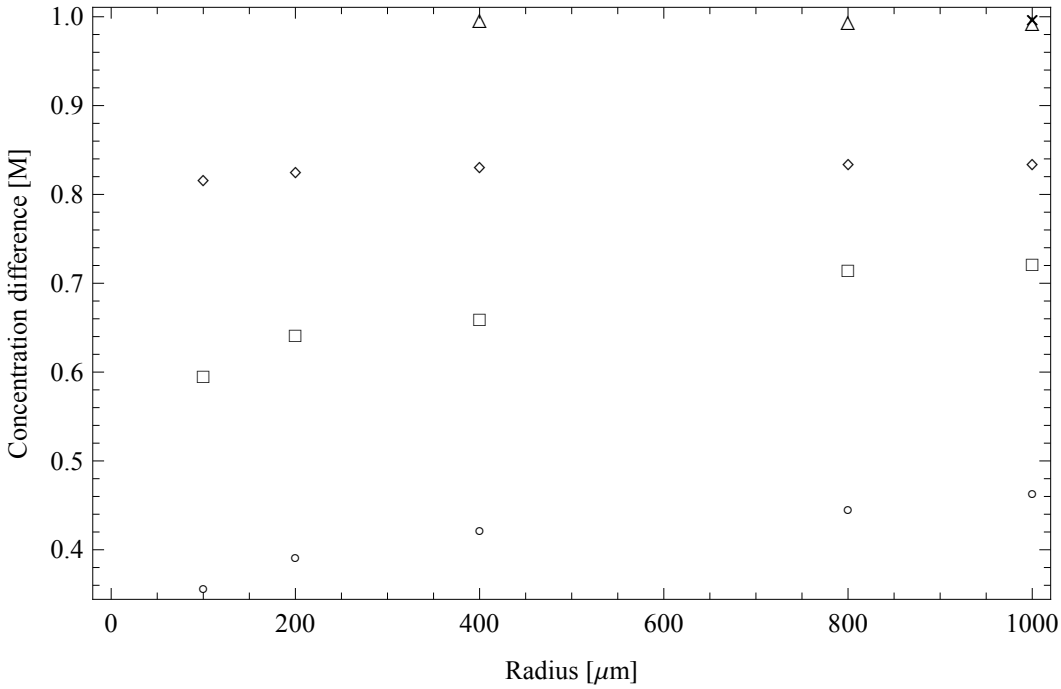

Figure 5.9: Concentration range is the difference in concentration between points A and B from figure 3.2. Inlet widths of 10 μm (Circle), 40 μm (Square), 100 μm (Diamond), 400 μm (Triangle), and 1000 μm (Cross)

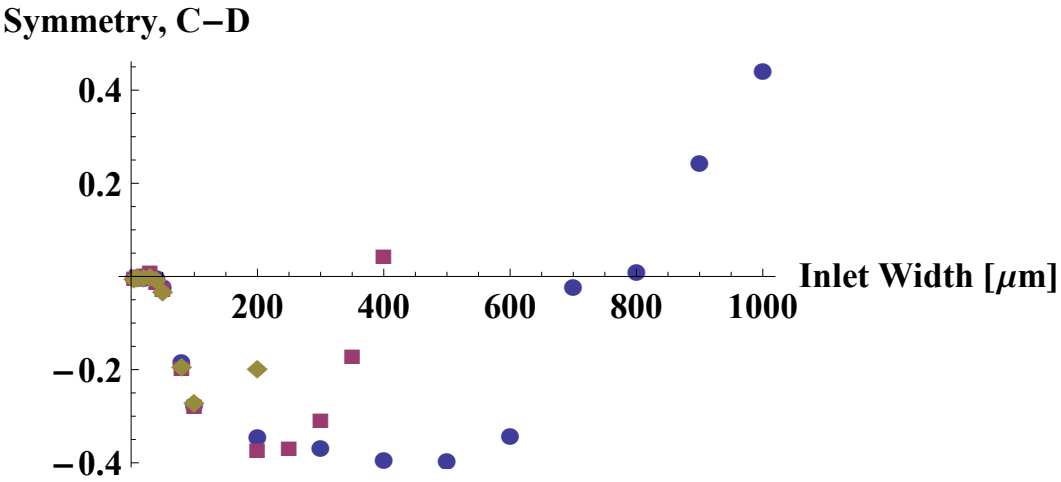

Figure 5.10: Symmetry within the chamber depends on the inlet width. Circle: 200 μm radius, Square: 400 μm radius, Diamond: 1000 μm radius

figure 5.10. Figure 5.10 shows that the concentration profile within the central chamber stays almost symmetrical, with a $C - D$ value of approximately 0 for inlet widths below 50μm. The difference between the concentration at points C and D is zero to 4 significant figures. This is the expected numerical error from the meshing of the simulations.

At inlet widths between 50 μm and 200 μm there is a steep decline in symmetry, to nearly -40% of the maximum difference. The difference in concentration between C and D stops declining at an inlet width equal to half the radius length. Above inlet widths greater than half the radius the value of C - D increases and returns to a value closer to zero. Eventually, at inlet widths approximately equal to the radius length, the value of C - D is close to zero. However, this is not an indication of returning symmetry. It is an artefact of the changing shape of the concentration gradient.

Figures 5.7(b) and 5.7(c) show the changing shape of the concentration gradient. At an inlet width of 80 μm and 200 μm the concentration gradient displacement is in the direction of flow, i.e. an increase in concentration to the right of the inlet. At an inlet with of 400 μm, which corresponds to an inlet width to inlet length ratio of 1, the concentration at points C and D are similar. However, the gradient around the inlet mouth is uneven, and is uneven above the centre point.

For a radius of 1000 μm the concentration difference between C and D tends towards zero at inlet width of 800 μm. Again, this is an artefact of the concentration gradient shape and not an indication of a return to symmetry. Figure 5.8 shows the concentration profile for a chamber with a radius of 1000 μm and an inlet width of 1000 μm.

The critical inlet width, above which there is an asymmetric concentration profile, is the largest inlet width that corresponds to a value if C - D approximately equal to zero. For inlet lengths of 10 μm, this significant asymmetry within the chamber can be avoided by having inlet widths below a critical inlet width of 50μm.

5.2.3 Effects of inlet neck length on concentration profile

Figure 5.11 shows that the inlet neck length can affect the concentration gradient profile. The larger the inlet neck length, the more symmetrical the concentration gradient profile.

At this range of inlet neck length and inlet widths, there is a limit to a larger inlet helping to even out the concentration gradient. At the largest inlet neck length, 80 μm, the critical inlet width can be increased from 50 μm to 100 μm.

The critical inlet width can be increased by increasing the inlet height. An inlet width of 100 μm and inlet neck length of 80μm is a recommendation if concentration profile symmetry is an important feature.

5.3 Characterisation of the flow profile within the central chamber

One of the intended benefits of the device is low convective flow within the central chamber, so it important to understand how the geometry of the device affects the flow profile.

5.3.1 Effect of inlet width on flow profile

Figure 5.12(a) to 5.12(c) show the flow profiles within chambers of radius 1000μm. An increase in inlet width leads to an increase in the magnitude of the flow within the central chamber. With a 5μm inlet the flow within the chamber is very low, in the order of $10^{-10} ms^{-1}$ and the inlet mouth approximates a point source.

When the inlet is increased to 300 μm, a circular flow around the chamber is established (figure 5.12(b)), with a flow velocity in the order of $10^{-5} ms^{-1}$. The small amounts of higher flow near each inlet is why the concentration becomes asymmetric. The inlet length provides some resistance to the convective flows and helps maintain low convective flows, and therefore symmetry of the concentration gradient.

At an inlet width of 1000μm, a flow pattern is established with vortices around each inlet,

shown in figure 5.12(c). It is possible to see that flow into the central chamber is higher than in the inlet channels immediately adjacent to the inlet mouth. The transport into the chamber is no longer diffusion dominated and the purpose of the microfluidic chamber to minimise convective flow, and allow diffusive transport to dominate in the central chamber, is defeated. At this large inlet width, the velocity immediately inside the inlet mouth reaches as high as 60 $\times 10^{-6} ms^{-1}$. Marcos and Stocker [2006] report that the motility of *P. haloplanktis* is not affected up to flow magnitudes of 36 $\times 10^{-6} ms^{-1}$, after which cells begin to tumble with the flow, up until 182 $\times 10^{-6} ms^{-1}$, when advection of cells dominates.

5.3.2 Effect of radius on flow profile

The radius also affects the flow profile. Figure 5.13 has a radius length of $100 \mu m$ and an inlet width of 100 μm. This inlet is smaller than the inlet featured in figure 5.12(b), but already has an established circular flow. Convective flow is discussed more fully in chapter 6.

5.4 Design considerations

There are many trade-offs to consider when designing a diffusion chamber. The variables investigated in this chapter are the geometry of the chamber radius, the inlet width and inlet neck length.

As shown in section 5.1.1, the time to reach steady state is proportional to the radius$^{2.1}$.

Equilibrium time can also be minimised by increasing the inlet width (time to reach steady state α inlet width $^{0.7}$). However, there is a critical inlet width, above which has the undesirable side effect of skewing the concentration profile. Keeping the gap size smaller than 50 μm minimises the the concentration gradient skewing and minimises the convective flow and circular flows within the chamber.

The concentration range available in the central chamber is insensitive to radius, but highly sensitive to inlet width up to 400 μm after which the concentration range is at a

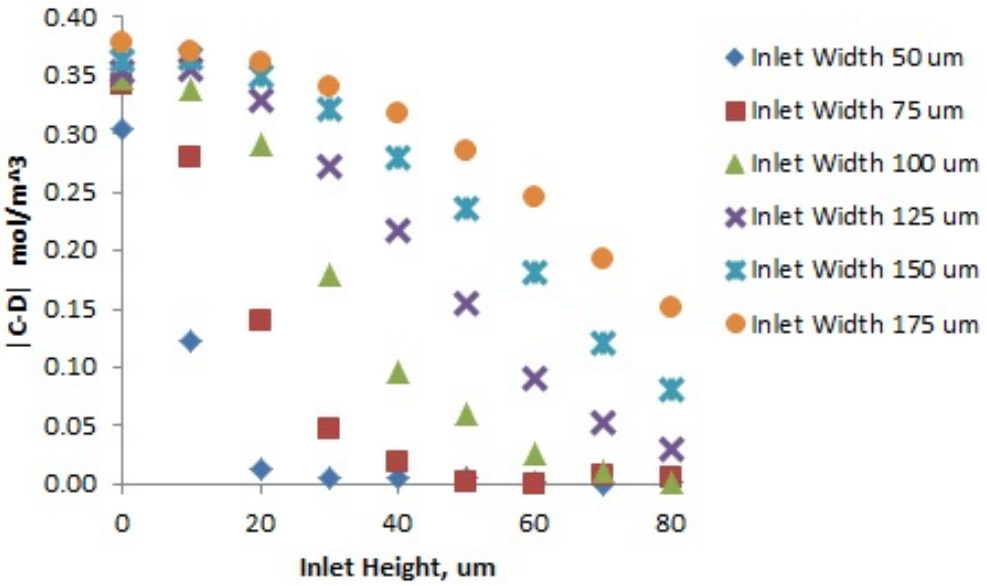

Figure 5.11: The critical inlet width, after which the concentration gradient becomes asymmetric within the chamber, is increased by increasing the inlet neck length.

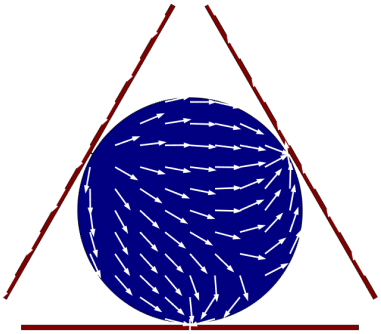

(a) Inlet width $5\mu m$

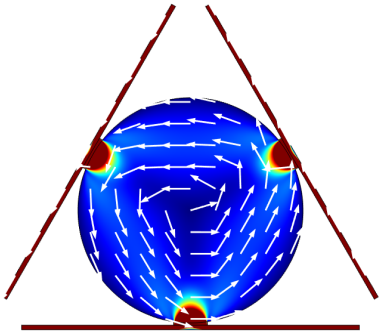

(b) Inlet width $300\mu m$

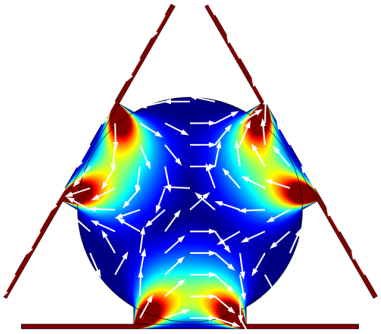

(c) Inlet width $1000\mu m$

Figure 5.12: Radius of 1000 μm. The colour is an indication of the magnitude of velocity and arrows show the direction of flow at their tail.

maximum.

Inlet width was the most important consideration to the symmetry of the concentration gradient. Inlet widths over 50 μm caused significant asymmetry. The critical inlet width can be increased by increasing the inlet length. However, this has an the impact of increasing t_{95}.

Inlet widths greater than the critical inlet width should only be used if the benefits (e.g. reduced time to steady state, ability to migrate in desirable microbes) are critically essential.

A balance must be struck for the inlet neck length. t_{95} is increased with reducing inlet aspect ratio, i.e. width/length. Above an aspect ratio of 2 there is no appreciative reduction in t_{95}. Increasing height both increases the t_{95}, an effect undesirable for experimental work, and increases the symmetry of the concentration gradients, a desirable feature for concentration gradient predictability.

5.5 Summary

A diffusion chamber in which it is possible to maintain a concentration gradient has been characterised. The effect of the geometry of the central chamber radius length and inlet design on equilibrium times, the concentration profile and the flow profile have been analysed. Geometry can affect the range of concentrations available within the central chamber and the symmetry of the profile. It was found that changing the central chamber size affected the time to steady state, with a dependence on radius$^{2.1}$, but radius did not quantitatively affect the concentration range.

From the results in this chapter it is recommended chamber radius is designed to control time to steady state and inlet width is kept below 50 μm. An inlet width below 50 μm gave a symmetrical concentration gradient, whilst inlet widths above 50 μm significantly affect the symmetry and predictability of the gradient.

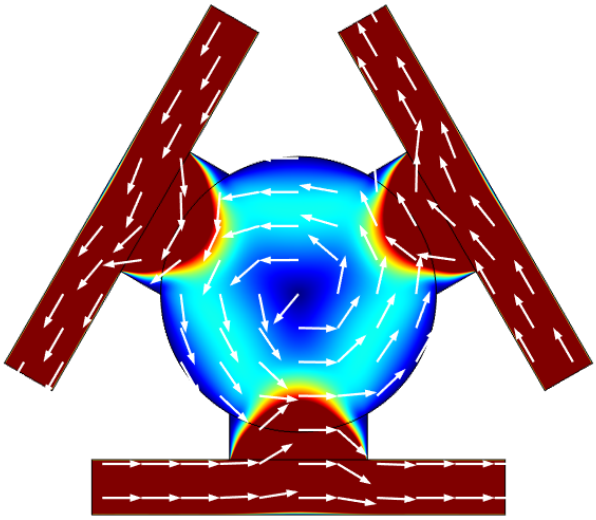

Figure 5.13: Flow profile within a central chamber that had dimensions of radius 100 μm and inlet width 100μm

Chapter 6

Characterising the Operational Conditions on a Controlled Concentration Gradient

In the previous chapter, chapter 5, the design was optimised for a microfluidic device that has a central chamber within which is a low convective flow and a maintained concentration gradient. This is a useful tool to study cell motility, particularly chemotatic movement. This chapter focuses on optimising the operation of the devices, to achieve the desired concentration and flow profile.

Numerical simulations, completed in COMSOL, are used to explore microfluidics with a geometry similar to figure 5.1(a). In this chapter aspects of the inlet flow are varied. The effect of the configuration of inlets and outlets is explored. Inlet channels can be configured one of three ways, as shown in figure inlet/outlet ports are arranged as in fig 6.1. It is also possible to arrange the inlets in a mirror image, and as such have a configuration in which all the inlets flow clockwise. An inlet configuration with all clockwise flow has the same physical conditions as anticlockwise, so has been deemed redundant, and is not simulated. The effect

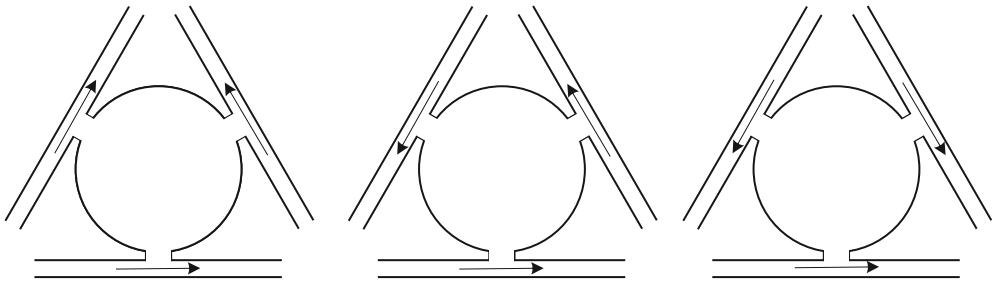

(a) Two sink channels flowing up, Up

(b) All channels flowing anticlockwise, Anti

(c) Two sink channels flowing down, Down

Figure 6.1: The inlet/outlets can be arranged in three ways. The source channel is always the channel flowing from left to right

of inlet flow rate is explored on the time to reach steady state, t_{95}, the concentration profile and the flow profile within the central chamber.

6.1 Inlet configuration

This sections looks exclusively at the effect of inlet configuration. The inlet/outlet ports are flexible in their arrangement and can be in one of 3 configurations i.e. anti, up or down shown in fig 6.1. If the transport within the central chamber was exclusively diffusion, then the inlet configuration should not make a difference. However, as inlet width increases, and there is increasing bulk flow into the central chamber, the direction of the flow in the inlets will begins to have an effect.

6.1.1 The effect of inlet configuration on t_{95}

Figures 6.2 and 6.3 show the time to reach t_{95} at different points within the device, moving from the centre to the perimeter for devices with an inlet width of 80 μm with a central chamber that has a radius greater than 200 μm, at channel inlet speed of 0.0004 ms^{-1}. Figure 6.2 shows the t_{95} for a radius of 200 μm for the three possible configurations. Although t_{95} is not exactly in agreement between the three configurations, the difference can be accounted for by the resolution of the time steps of simulation. The transient solver evaluated the concentration every second, and t_{95} on figure 6.2 are within 2-3 seconds. Figure 6.3

shows the t_{95} of a device with a central chamber that has a radius of 1000 μm. The solver evaluated every 5 seconds. With a radius of 1000 μm the points are further away from the source of the solute, t_{95} for the three configurations differ significantly from the simulation resolution. Fig 6.3 demonstrates that as the radius gets larger and t_{95} increases, the difference between configurations becomes significant compared to the time step resolution. At the furthest point from the centre, at the far edge, using an Anti configuration saves 150 seconds, or is 4 % quicker than Up.

If minimising the time to reach steady state is of a high priority, the Anti inlet configuration should be considered.

6.1.2 The effect of inlet configuration on concentration profile

The concentration gradient was affected by the configuration but only at inlet widths above 50 μm.. Fig 6.4 shows qualitatively the profiles.

The concentration range present in the central chamber has been evaluated by taking the concentration at the bottom edge minus the concentration at the top edge of the chamber as shown in figure 5.1(a). This value changes significantly between the three configurations only for inlet widths above 50 μm. Above 50 μm, there is convective flow in the central chamber, which means that the inlet configuration had an effect on the velocity at the central. This is explored more in detail in section 6.1.3. In comparison to the Anti inlet configuration, the concentration gradient in a central chamber with Up inlet configuration is affected by having a smaller concentration range as the convective flow drags solute towards the perimeter opposite the solute inlet, so there is a higher concentration. Conversely, Down had a greater concentration range, as the convective flow at the centre point is towards the source of the solute, therefore reducing, or possibly eliminating, diffusive transport of the solute, so has a lower concentration of solute at the perimeter directly opposite the solute source.

The symmetry of the concentration profiles is not affected at inlet widths below 50 μm

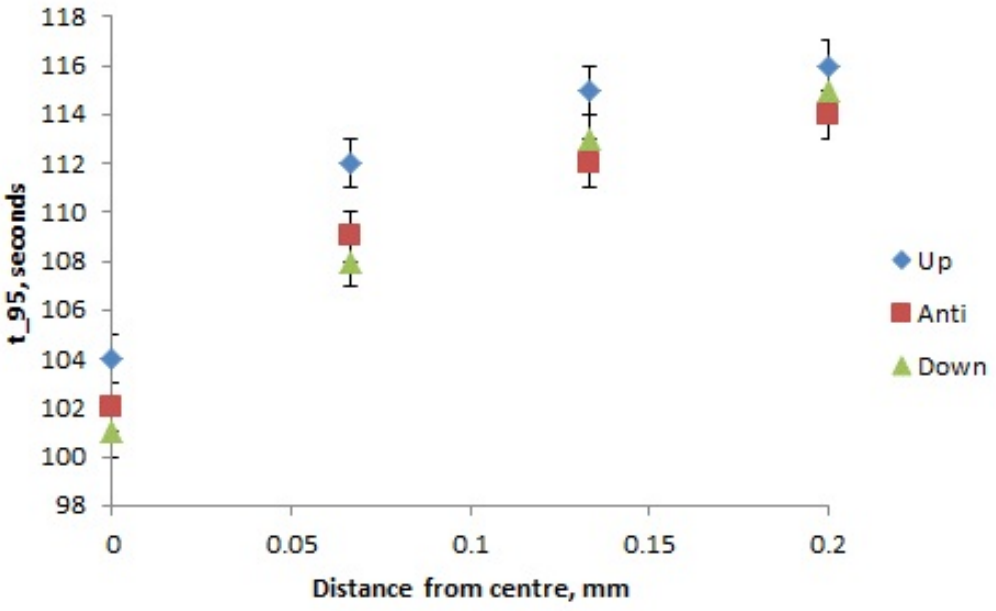

Figure 6.2: Time to Steady State radius 200 μm, inlet width 80 μm. The step size for time points was 1 second

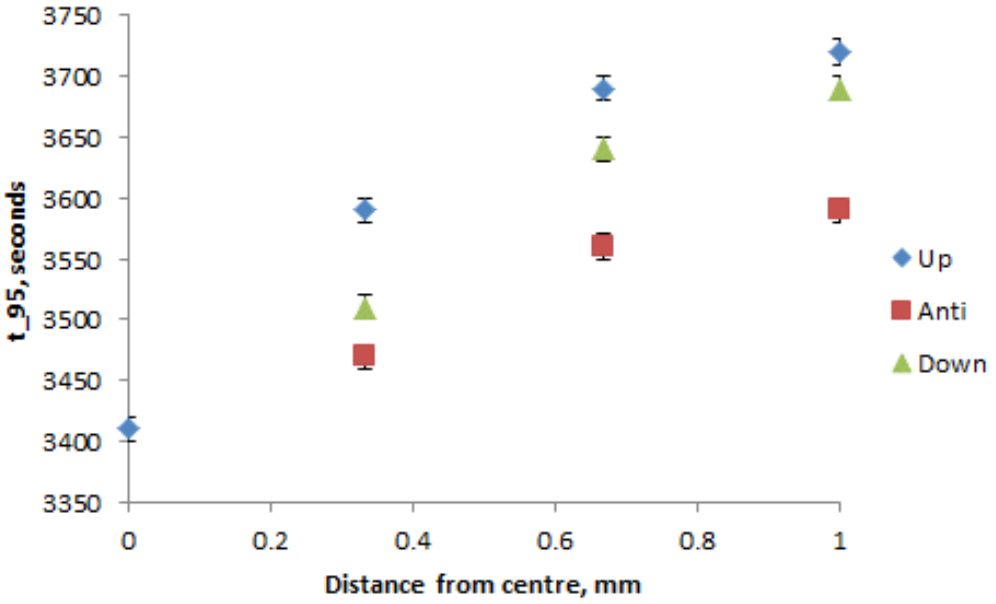

Figure 6.3: Time to Steady State radius 1000 μm, inlet width 80 μm. The step size for time points was 10 seconds

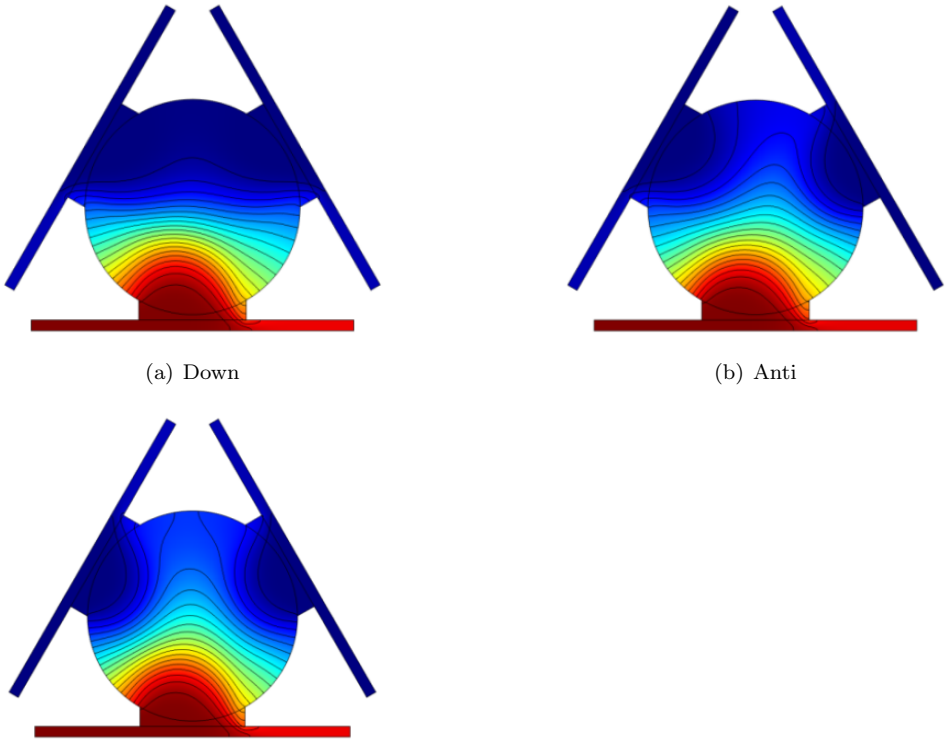

(a) Down

(b) Anti

(c) Up

Figure 6.4: Concentration profile for a chamber with radius 400 μm and a large inlet width of 400μm

by the inlet configuration. From the previous chapter, chapter 5, it was recommended that inlet widths below 50 μm are used.

6.1.3 The effect of inlet on speed profile within the central chamber

The velocity at the centre point of the chamber is affected by the inlet configuration, as shown in table 6.2. The chamber with Anti inlet configuration has a velocity magnitude two orders of magnitude lower than either the Up or Down configuration. At the centre point of the chamber, with all the inlet channels flowing anticlockwise, the tangential vector of velocity magnitude is zero, for a fully diffusive system. The simulations show a centre point velocity of approximately $10^{-8} ms^{-1}$. The radial vector is also zero, as at the centre $r = 0$. For chambers with a low convective flow, as r increases, $r \times v\theta$ remains low, and the velocity magnitude is low.

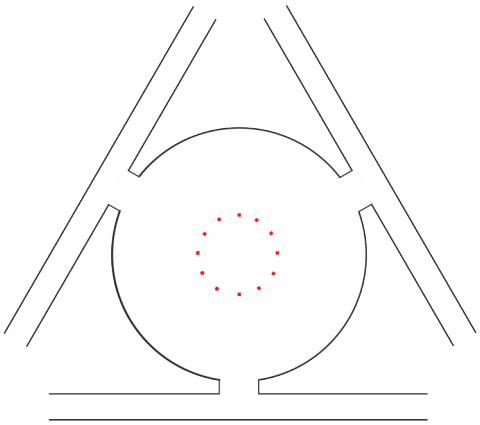

Figure 6.5: Points within the central chamber that the velocity is evaluated in figure 6.6

The Up and Down configurations have similar velocities to each other. However, Up and Down configurations result in a net vector at the centre, which results in approximately two orders of magnitude increase in speed at the centre point, when compared to the Anti configuration. Table 6.2 shows that the y components for Up and Down configurations at the central point were opposite and approximately equal.

The speed in the central chamber at points off-centre were also investigated. Speed was sampled at 12 points, all a distance of radius/3 from the centre, as shown in figure 6.5.

Fig 6.6 shows the speed at each point for 3 inlet configurations for a device with radius of 400 μm and inlet width of 5 μm. Although for specific points speed can be minimised by choosing a specific configuration, the configuration that minimises speed fluctuates from point to point.

Figure 6.8, showing arithmetic average of the speed confirms that inlet configuration has a small and fluctuating effect on flow rate inside the central chamber. The average of this speed was increased as the gap increased. There's no configuration that significantly minimises the overall convective movement within the chamber. There is no clear advantage or disadvantage for the speed profile within the central chamber attached to choice of inlet configuration.

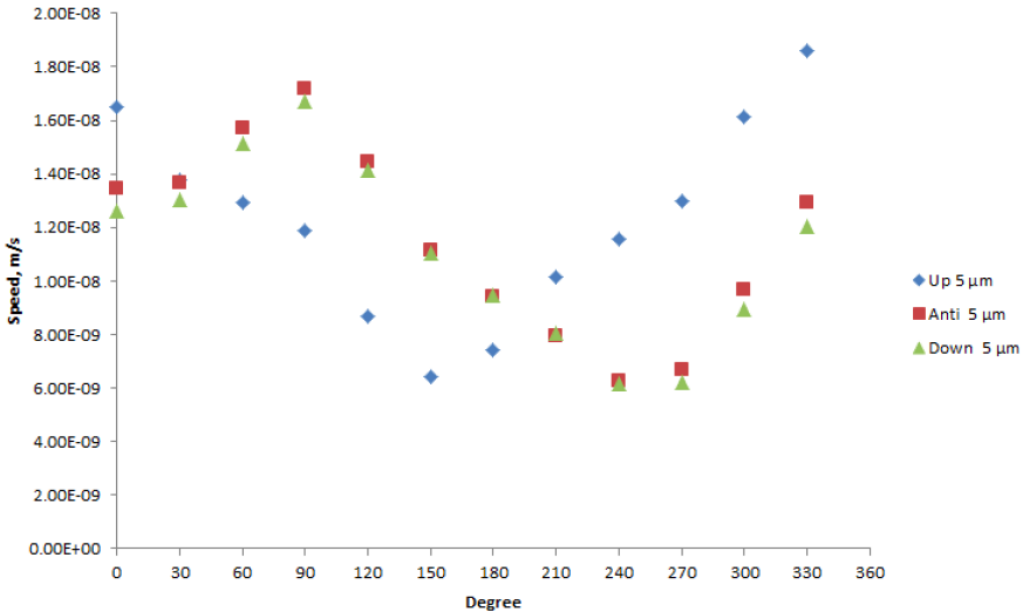

Figure 6.6: Speed at points indicated in figure 6.5, in a central chamber with a radius of 400 μm and an inlet width of 5 μm

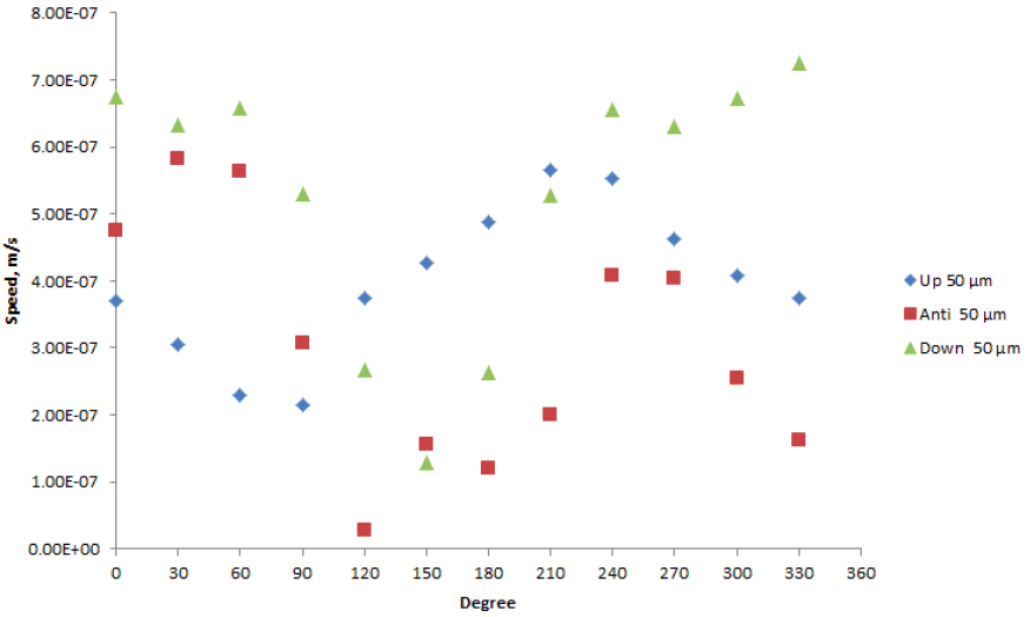

Figure 6.7: Speed at points indicated in figure 6.5, in a central chamber with a radius of 400 μm and an inlet width of 50 μm

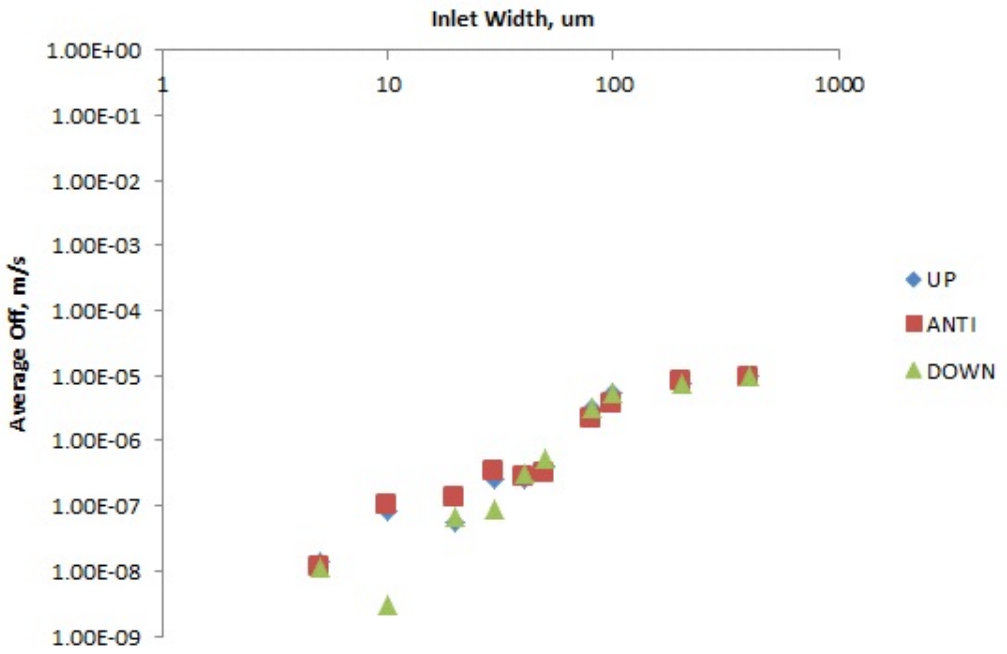

Figure 6.8: Average speed within the central chamber, average = $\Sigma speed/12$

6.2 Effect of inlet channel speed

In this section, the effect of the speed of the flow within the inlet channel has on the time it takes to reach steady state in the chamber, and the shape of the concentration profile are analysed.

6.2.1 The effect of inlet channel speed on t_{95}

The t_{95} when inlet channel speed varied between 0.0001 ms^{-1} to 0.1 ms^{-1}, and all channels have an equal flow rate, is shown on figure 6.9.

t_{95} is reduced with increasing inlet channel speed. This can be explained using the Sherwood number in equation 6.1.

$$Sh = \frac{s \times W}{D} \tag{6.1}$$

where Sh is the Sherwood number, s is the speed of flow in the inlet channel, W is the inlet width and D is the diffusivity.

Inlet Width	UP	ANTI	DOWN
5 μm	0.224	0.225	0.225
50 μm	0.570	0.560	0.554
400 μm	0.822	0.902	0.992

Table 6.1: The range of concentrations available within the central chamber, bottom concentration - top edge concentration, A-B from figure 3.2

	Vel Mag	x	y
Anti	8.93E-08	7.19E-08	5.30E-08
Up	6.26E-06	-3.12E-06	-5.42E-06
Down	6.34E-06	-3.27E-06	5.44E-06

Table 6.2: The velocity magnitude, and x and y components in at the centre point of the central chamber of with a radius 200 μm and 80 μm inlet

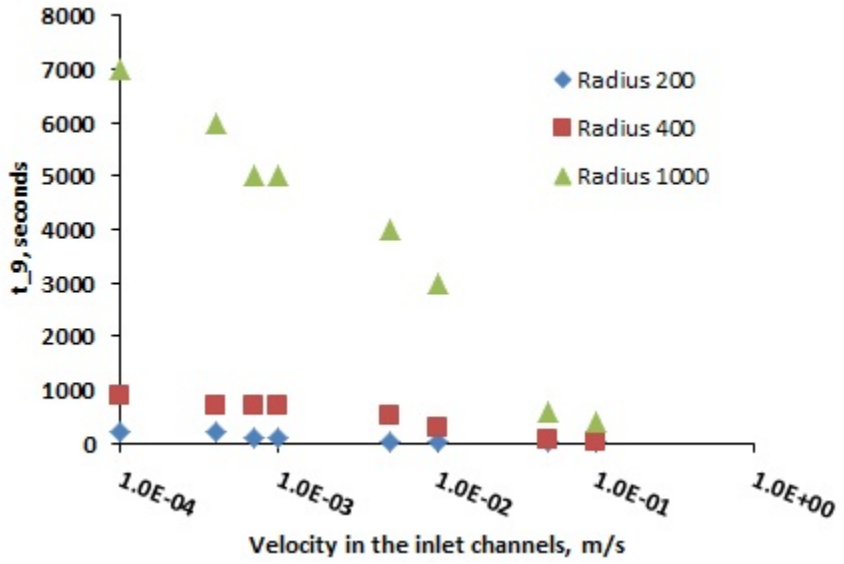

Figure 6.9: t_{95} with varying inlet channel speed

The Sherwood number is the ratio of convective to diffusive flow. In all the simulations results included in figure 6.9 the characteristic length, of inlet width, is the same. The diffusivity is also constant. The Sherwood number for the system is proportional to the speed in the inlet chamber. As the inlet speed increases, so does the Sherwood number, which is an indication of more convective flow, which is why the time to reach steady state is reduced.

6.2.2 Effect of varying the speed within the inlet channel on the concentration profile within the central chamber

In this section, the speed within the inlet channel is varied between 10^{-1}ms^{-1} to 10^{-4}ms^{-1} in a device with central chamber dimensions of 400 μm radius, 50 μm inlet width and 10 μm inlet neck length. Figure 6.11 show qualitatively the effect of flow rate within the channel on the concentration profile within the central chamber.

Previously it was discussed in chapter 5 for an inlet channel velocity of 0.0004 ms^{-1} that an inlet width below 50 μm kept the concentration profile symmetrical regardless of the radius length. However, figure 6.11 shows that the concentration profile is unsymmetrical, even with inlets of 50 μm, at inlet channel speeds of 10^{-2}ms^{-1} and above. The critical inlet width, above which the profile is asymmetric, is decreased with increasing speed in the inlet channels.

Figure 6.10 uses the same indicative value of concentration profile symmetry as in section 5.2.2, i.e. the difference in concentration between C and D. Concentration profile symmetry is evaluated for inlet channel speeds between 0.0001 ms^{-1} and 0.1 ms^{-1}. It shows that for a device with radius 400 μm and Anti inlet configuration the inlet width up to which the symmetry of the concentration profile is preserved is dependant on the flow speed in the channels. An increased speed in the channel decreases the critical inlet width.

The choice of inlet speed when operating the channels must take into consideration an appropriate critical inlet width.

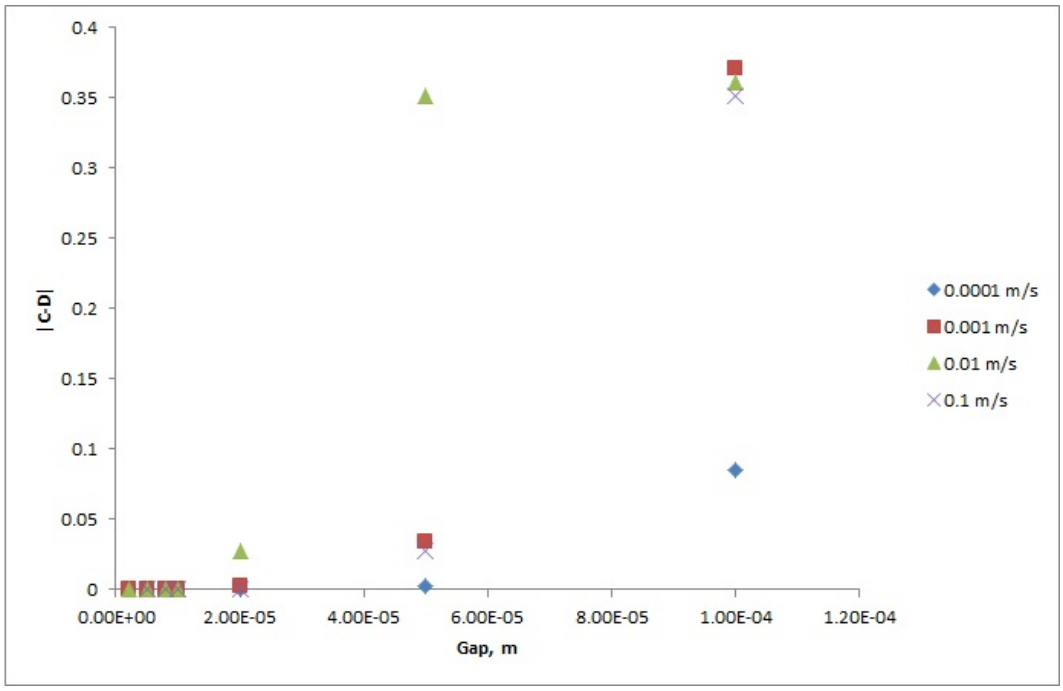

Figure 6.10: Symmetry of the concentration profile within the chamber with a radius of 400 μm

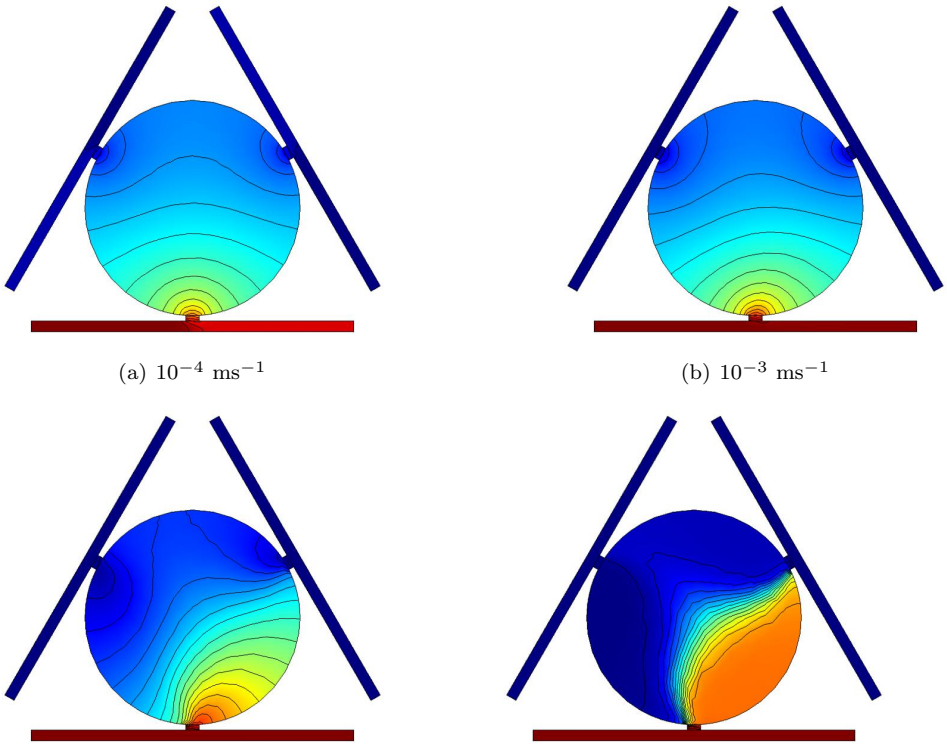

(a) 10^{-4} ms^{-1}

(b) 10^{-3} ms^{-1}

(c) 10^{-2} ms^{-1}

(d) 10^{-1} ms^{-1}

Figure 6.11: Concentration profile at different inlet speeds in a central chamber with a 400 μm radius and an inlet width of 50μm

6.3 Effect of inlet channel speed and configuration combined

In this section data is compared for devices that have both inlet channel speed and configuration as variables.

6.3.1 Effect of inlet channel speed and configuration on velocity profile

Motile cells are able to actively swim in quiescent flows. At low speeds they are still able to be actively motile, but above a critical flow speed, the cells cannot swim and advective transport dominates and cells tumble with the bulk flow. A low convection environment within the central chamber may be desired if studying suspended motile cells. The velocity profile within the central chamber varies depending on both the configuration and the inlet speed.

Figure 6.12 shows that speed at the centre point of the central chamber is greatly reduced at all inlet speeds by having an Anti configuration. The dependence of central speed on inlet channel speed is reduced by 2 orders of magnitude for the Anti configuration compared to Up and Down inlet configurations. This range shows a linear dependence, Down and Up have a gradient of 10^{-7} and Anti a gradient of 10^{-9}. For low convective flows at the centre of the chamber, an Anti inlet configuration is recommended, at any inlet speed.

Speed at the centre is not the only concern. For studying cell motility, and not cell advection, the maximum velocity magnitude in the chamber must be below that of the critical speed that induces tumbling of motile cells. Figure 6.13 shows how for a design choice of inlet width, and an operating choice of speed within the inlet channel, the maximum velocity within the central chamber can be controlled.

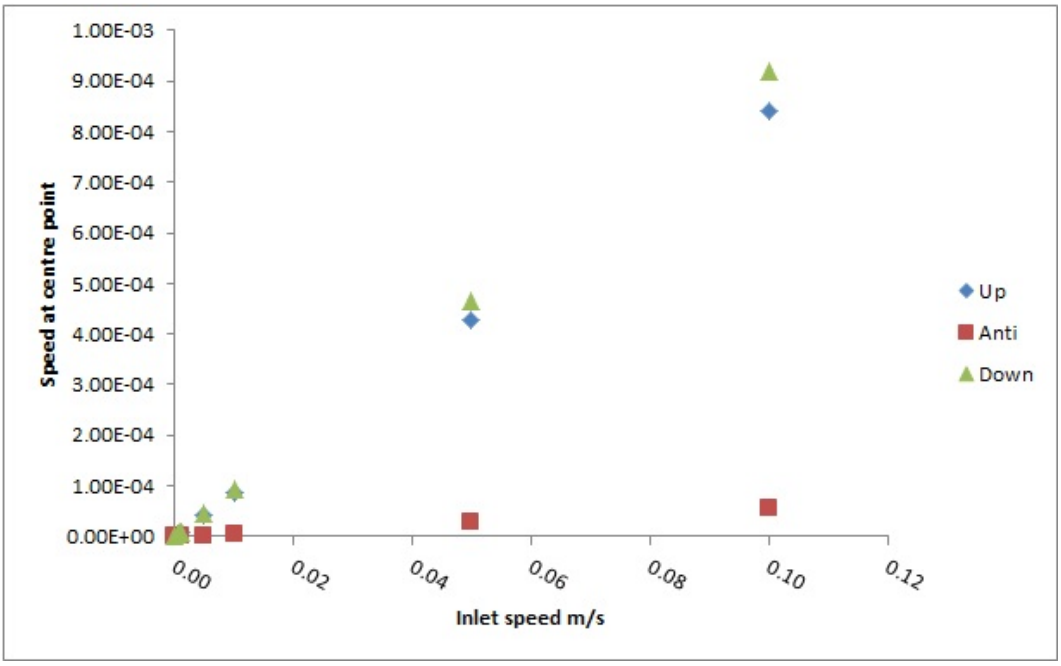

Figure 6.12: The velocity magnitude at the centre point of a chamber with a radius 400 μm, inlet width 80 μm and inlet length of 10 μm

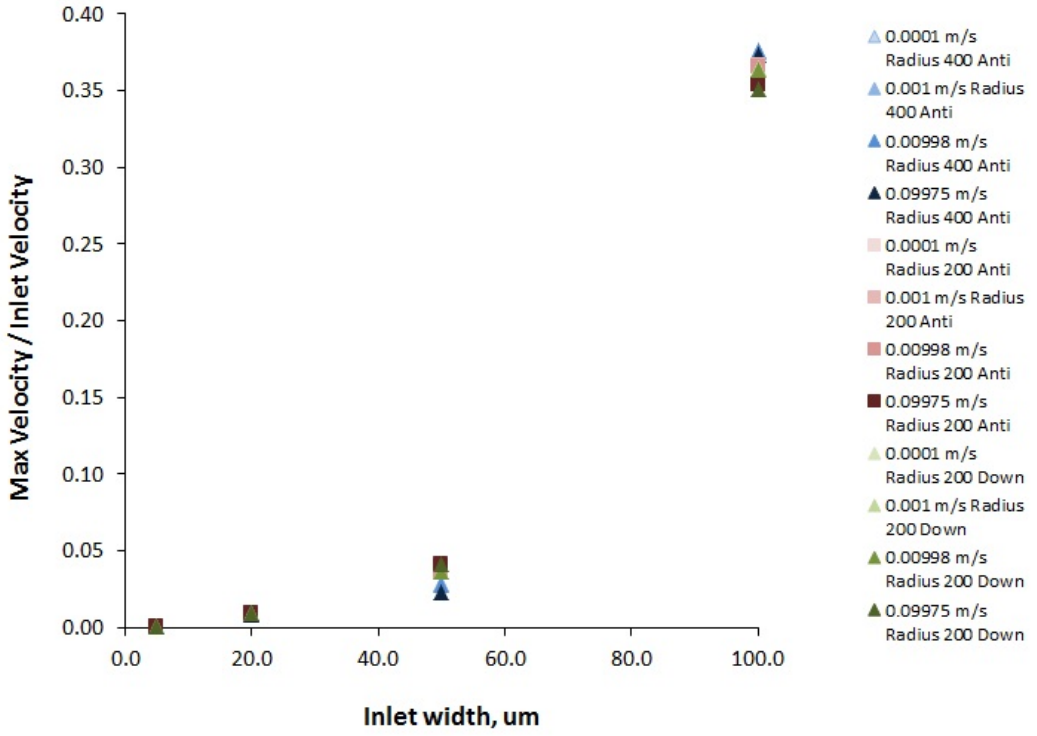

Figure 6.13: Controlling for the maximum velocity in the chamber by using the geometry of the inlet, and the speed within the inlet channels.

6.4 Summary

The operational parameters for a microfluidic device have been characterised. The effect of inlet channel configuration and speed within the inlet channels on the concentration profiles, flow profile and time to reach steady state within the central chamber has been analysed. Recommendations on operating the channels have been made. Inlet channel configuration is only weakly effective to t_{95}. At larger radii, over 1000 μm, it's beneficial to choose an Anti inlet channel configuration to minimise t_{95}.

It is possible to maximise the concentration range within the central chamber by choosing a Down inlet configuration.

The velocity magnitude at the centre of the chamber can be minimised by choosing an Anti inlet channel configuration.

Increasing the channel speed increases the Sherwood number, and the convective flow within the central chamber. Increasing the inlet channel speed decreases the critical inlet width for a symmetrical concentration profile.

It has been shown that for a design choice of inlet width, and an operating choice of the speed within the inlet channel, that the maximum velocity within the chamber can be controlled.

Chapter 7

Characterisation of Concentration Gradients within PDMS Microchannels

In this chapter, microfluidic devices were fabricated as described in section 3.3 and operated. Concentration gradients were maintained in the central chamber. Experimental data from microfluidics devices fabricated from PDMS, as described in section 3.3 was collected, to be compared to theoretical data from the numerical simulations calculated in COMSOL.

The design of the PDMS microfluidics had to accommodate certain practicalities. Using a microscope to visualise the central chamber required the inlet/outlet ports to be 3 mm from the central chamber, and the inlet/outlet channels to have a 120° bend. As well as allowing the light from the microscope condenser to not be obstructed by the port, these long channels also allow any irregularities in flow caused by the interface between the needles and the PDMS ports to even out.

7.1 COMSOL simulations conditions to replicate experimental design

Unlike the geometry used in 3.1, which had the inlet/outlet channels modelled as straight channels, the shape of the experimental PDMS channels has a bend in the channels. The effect of the corners on the simulation results was studied with the concentration profile as the indicative characteristic.

For an inlet channel speed of 0.0002 ms^{-1} and an inlet width of 50 μm the discrepancy in concentration gradient is less than 5 % between models with and without an inflection in the inlet/outlet channels. Speeds in the inlet channels of 0.0007 ms^{-1} and above had discrepencies greater the 10 %

The syringe pump used during the experiments had a minimum flow rate of 0.0288 ml hour^{-1}, which is a flow speed of 0.002 ms^{-1}. As the syringe pump flow rate is out of the range in which the COMSOL model is representative, it was chosen to modify the simulation geometry to be more similar to the experimental channels. An example of the geometry with the inflections in the inlet channels in shown in figure 7.1.

Following the recommendation in chapter 5 the devices were designed to have inlet widths of 50-80 μm. However, the imprinted PDMS has a lower resolution than the SU-8 stamp. This resulted in the experimental chambers having unexpectedly large inlet widths and small neck lengths. For example, fig 7.2 shows a device that was expected to have a radius 400 μm and inlet width of 80 μm, but actually has inlet width of 190 μm.

Results in chapter 5 showed that inlet width significantly impacts concentration profile and t_{95}. Therefore inlet widths were measured from microscope captured stills and this dimension used in the simulation, so that the experimental data had a comparative simulated data set. The neck height was set to zero. The dimensions of the experimental channels are in table 7.2.

The diffusion coefficient was changed to $4.2 \times 10^{-10} m^2 s^{-1}$ [Gendron et al., 2008], to

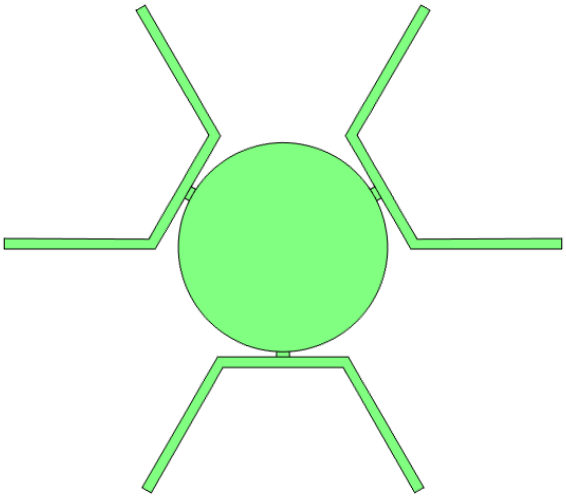

Figure 7.1: Schematic of the geometry used in the numerical simulations used as a comparison to experimental data.

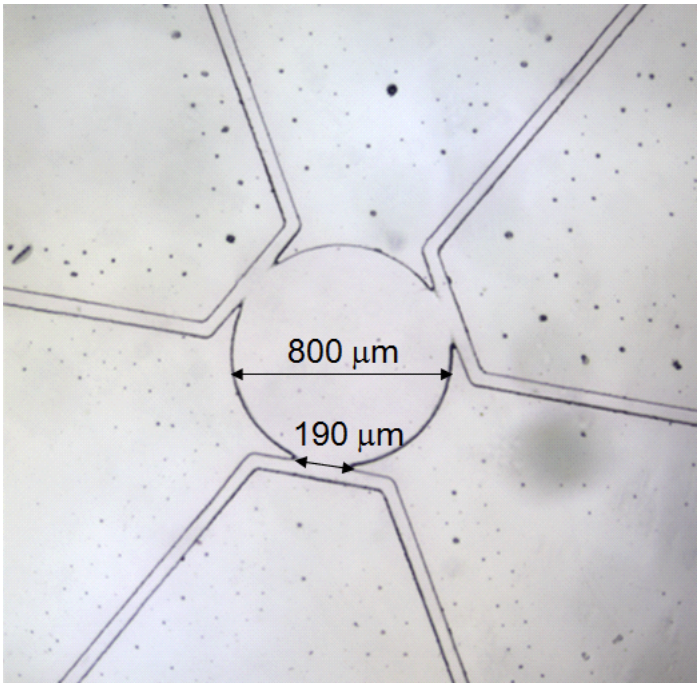

Figure 7.2: Experimental geometry

match that of rhodamine-B in water.

In summary, simulation conditions are as follows

- inlet channel speed is 0.002 ms^{-1}
- the geometry of the neck was zero, and the inlet width was set to match the experimental conditions
- Diffusion coefficient $4.2 * 10^{-10} m^2 s^{-1}$

Otherwise, all simulation conditions are kept the same as in section 3.1, and t_{95} is defined as 95% of the steady state value, obtained from a study using a stationary solver.

7.2 Experimental Procedure

In these experiments, all flows were anticlockwise.

A protocol was developed for filling the chambers

For filling the chambers

1. Three pieces of Polytetrafluoroethylene (PTFE) tubing of 0.8 mm ID, cut to the same length. In one end insert a blunt needle with a hub fitting for a syringe, 0.9 mm OD. In the other end insert a blunt needle shaft, 0.9 mm OD and insert the needle into the PDMS inlet ports.
2. Three pieces of PTFE tubing of 0.8 mm ID, cut to the same length. In one end insert blunt needle shaft, 0.9 mm OD. Insert the needle into the desired PDMS outlets ports, and place the free ends into a reservoir at least 15 cm above the device, to create a back pressure.
3. Fill three 1 ml syringes with DI water
4. Expel bubbles from the syringes
5. Fit syringes to the needle hub, from step 1

6. Set the syringe pump flow rate to 40 ml hour^{-1} until the tubing is primed, approximately 30 seconds

7. To fill the central chamber, lower the flow rate to 4 ml hour^{-1} for approximately 1 minute

8. To rid the central chamber of bubbles, increase the flow rate to 40 ml hour^{-1} for 10 - 20 seconds, until all the bubbles are dissolved.

9. Set flow rate to 0.0288 ml hour^{-1}, and allow the flows to equilibrate for at least 5 minutes.

   Preliminary experiments to characterise the chambers had a DI water syringe swapped to one containing food dye, but it was found that the contrast was too low between the water and dilute food dye. Neat food dye had a higher viscosity than water that affected the flowrate in the narrow inlet channels. Microfluidic device characterisation experiments were completed using 1 wt % rhodamine-B. Rhodamine-B was chosen for the large contrast, and the possibility of utilising fluorescence. For the experiments in this chapter fluorescence microscopy was not used; bright field provided enough contrast.

   Extra steps were followed for testing the steady state time for the rhodamine-B solution

   Introducing rhodamine-B into channels

10. A fourth syringe was filled with 0.45 μm filtered 1 % rhodamine-B in DI water solution and fitted with a needle and hub, PTFE tubing matching the length of the other inlets, and a needle shaft.

11. After step 9 is satisfied, pipette a drop of DI water on an inlet port, remove one on the needles from the inlet port, and replace with needle delivering rhodamine B. The drop of water reduces the likelihood of bubbles being introduced into the chamber.

    To get repeats from the same device, the flushing protocol was used.

Device	t_{exp}, secs					t_{95}, secs
A	33					61
B	72	64	76	138	556	238
C	32					875
D	1080	50	156			249

Table 7.1: Comparison of experimental times to reach steady state and simulation t_{95}. The dimensions of devices A, B, C and D are in table 7.2

.

Device ID	radius, μm	inlet, μm
A	100	50
B	400	80
C	800	50
D	400	80

Table 7.2: Dimensions of experimental chambers

Flushing channels

12. Remove Rhodamine-B needle from PDMS inlet port and replace with DI water

13. Set flowrate to 10 ml hour^{-1} for 2 - 3 minutes until all visible traces of dye were removed

14. Reduce flowrate to 1 ml hour^{-1} for 10 minutes

7.3 Results

7.3.1 Experimental times to reach steady state

Estimates of the experimental time to steady state, t_{exp}, were made by taking t_0 to be when the dye front first reaches the central chamber entrance and t_{final} to be when the front crosses the centre point i.e. $t_{exp} = t_{final}$ - t_0. Examples of these are shown in figure 7.3. t_{exp} are presented in table 7.1 alongside t_{95} from simulation results.

t_{exp} were found to be not reproducible. They neither correlated with the time to reach steady state produced by the simulation or made reproducible results with repeats in the same device, or runs in devices with similar geometry.

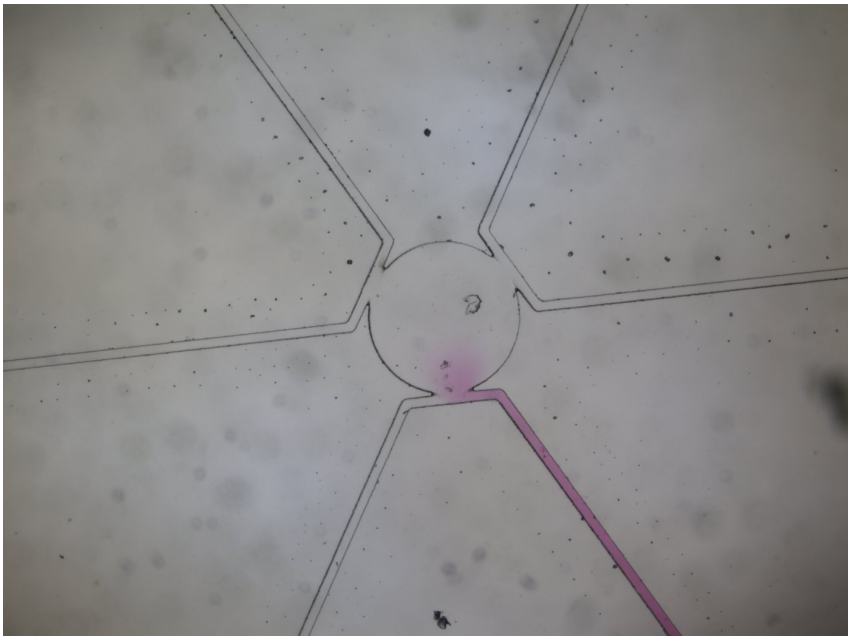

(a) The frame of the video corresponding to t_0

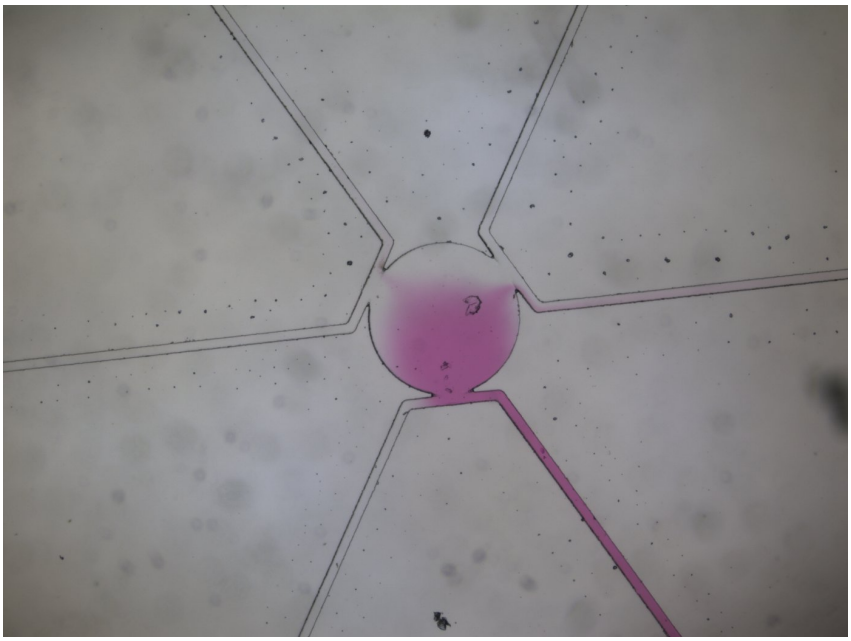

(b) The frame of the video corresponding to t_{final}

Figure 7.3: Experimental concentration gradients developing

7.3.2 Experimental concentration gradients

It was found that concentration gradients can be maintained for minutes at a time. However, concentration gradient profiles were not consistent between repeats in the same device. Fig 7.4 are frames from the videos showing that different profile shapes form in the same device on repeats.

Figures 7.4(a) and 7.4(b) show the concentration gradient inside device B. The pictures show quite different shaped concentration gradients, with the bulk of the rhodamine-B solution exiting via different outlet channels. The same can be seen in figures 7.4(c) and 7.4(d) for device C.

Some videos show how unstable the flow within the inlet channels is. There is clearly back flow of water into the channel that the rhodamine-B solution is exiting. This is shown in figure 7.5. It can be seen that the inlet channel the rhodamine-B solution is dark pink. In the next frame of the video, approximately 0.2 seconds later, the mouth on the inlet is pale pink, showing a decrease in concentration and the flow of water into the rhodamine-B inlet channel.

The pressure must be lower in the inlet channel than any of the outlet channels. This could be because the syringe pumps produce a slightly unsteady pulsile flow. Working at the very lower end of the syringe pump capabilities exacerbates this problem.

More evidence of unsteady flow from the syringe pump is that in some cases, a faint pink concentration gradient can be seen preceding the dark pink gradients. It could be that the rhodamine-B solution from within the needle has moved along the inlet channel and into the chamber by diffusion though the inlet channels, ahead on the bulk flow. This suggests that the flow is pulsile.

Figures 7.6(a) and 7.6(b) show the shape of the concentration gradient at steady state within the central chamber in both the experimental chambers and the simulations. Although the simulation predicted the concentration gradient skewed to the right, with a higher concentration on the right hand side of the chamber, the experimental gradient is

skewed to the left.

The simulation's velocity profile, figure 7.6(c) shows an anticlockwise flow vortex in the central chamber. For the experimental result, the vortex within that chamber cannot be an anti clockwise vortex. This points to uneven inlet flows/ pressures.

All these differences to the simulations suggest that there were uneven, and unsteady flows within the inlet channels. Perhaps these were caused by operating the syringe pump at the very lower part of its range, stiction in the syringes or irregularities within the inlet channels caused by deformation during the fabrication process.

A preliminary simulation was completed, to confirm the role of convective flow within the experimental chambers. Figure 7.7 shows the theoretical concentration gradient inside a central chamber when the source and sink inlets are unbalanced. The source inlet channel has a velocity of 0.001 $ms^{-}1$, and the two sink channels have a velocity of $0.0004ms^{-}1$. The theoretical concentration gradient echoes the experimental concentration gradients seen in figures 7.4(b) and 7.4(d). This confirms that the experimental chamber is experiencing convective flow.

7.4 Conclusion

PDMS microfluidic channels were designed, fabricated and a protocol for filling the chambers was developed. Experimental chambers were found to have different geometries than expected, due to a loss of resolution between the design and fabrication process. A new geometry for the device has been used for the numerical simulations. With a faster flow rate in the inlet channels due to the limitations of the syringe pump, it was required that the inflection in the experimental channels was represented in the numerical simulations.

Concentration gradients of rhodamine-B were established and maintained within the PDMS devices. These concentration gradients and times to reach steady state were not reproducible. It had been suggested that increasing the neck length would help restrict the convective flow into the chambers. It was also suggested that a syringe pump that was

capable of small flows would help eliminate some of the pulsing in the flow in the inlet channels.

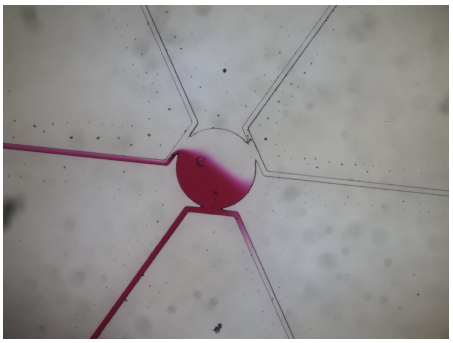

(a) Concentration gradient in device B

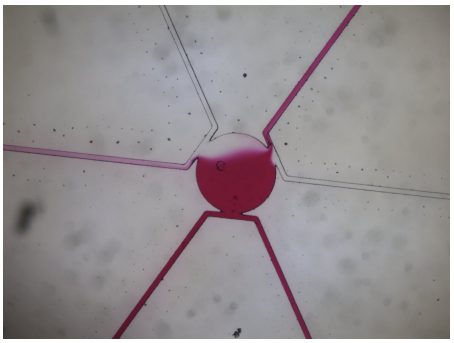

(b) Concentration gradient in device B

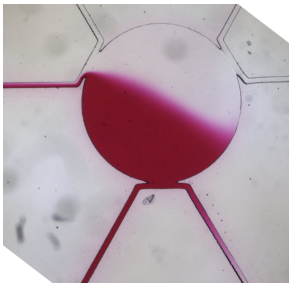

(c) Concentration gradient in device C

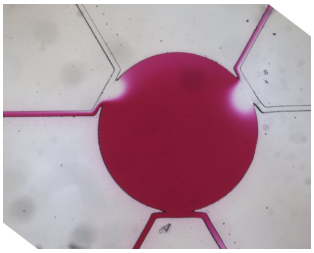

(d) Concentration gradient in device C

Figure 7.4: Different shaped concentration profiles in the same device.

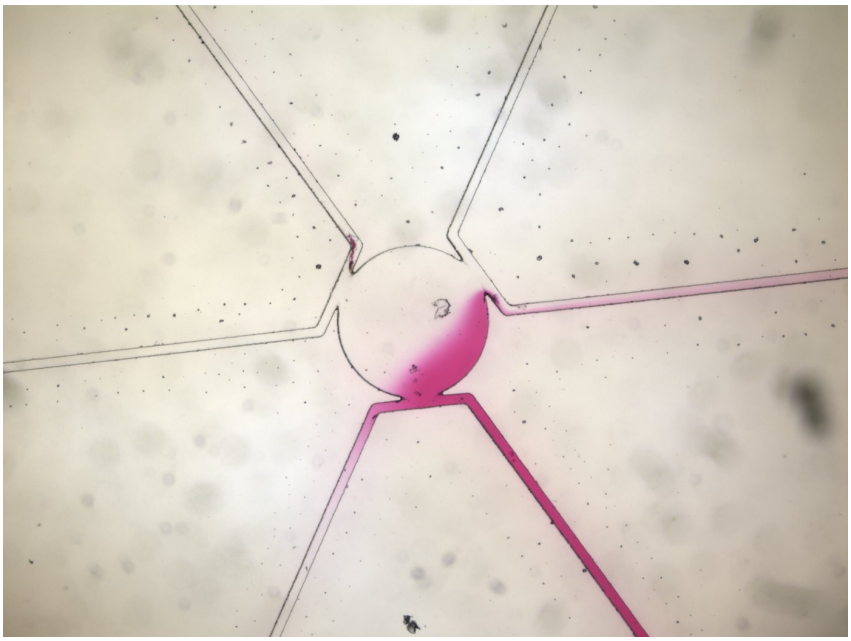

(a) Rhodamine-B solution flowing into the chamber

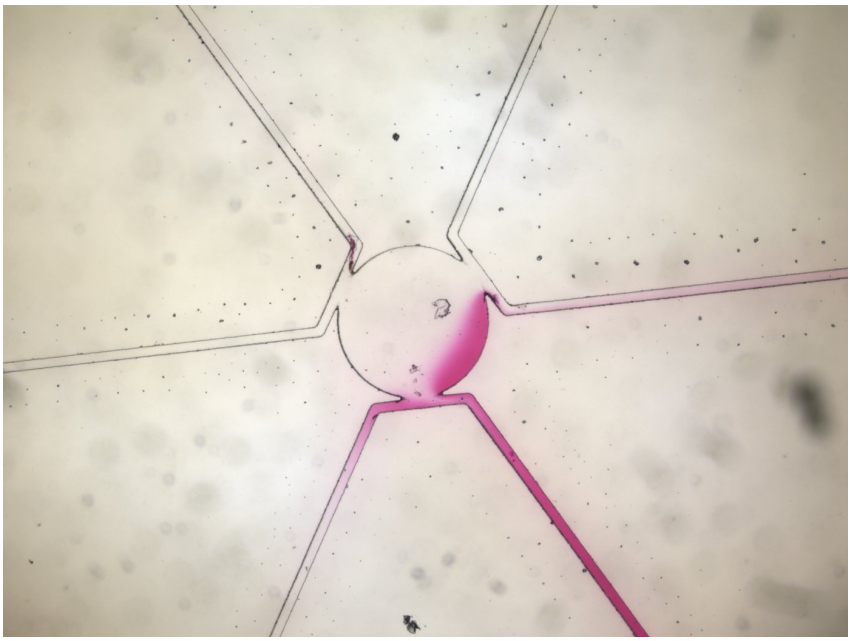

(b) Rhodamine-B solution being washed back into the inlet

Figure 7.5: Back flow into the inlet channel

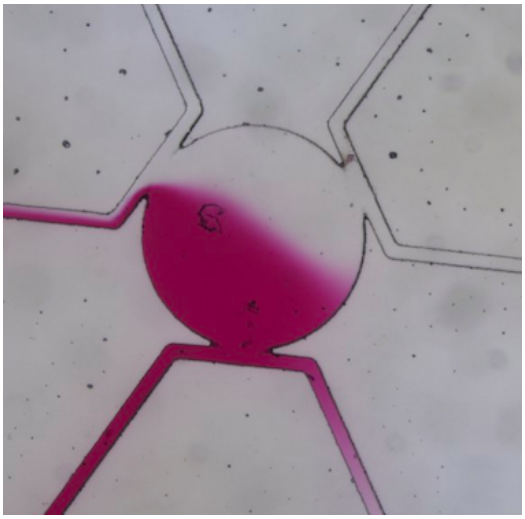

(a) Experimental geometry and concentration profile

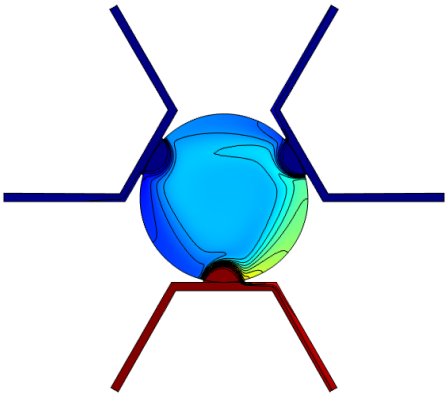

(b) Simulated concentration profile

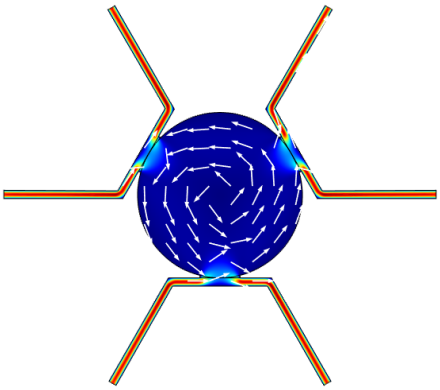

(c) Simulated velocity profile

Figure 7.6: Comparing experimental and simulated steady state concentration profiles. Radius 400 μm, inlet width 194 μm

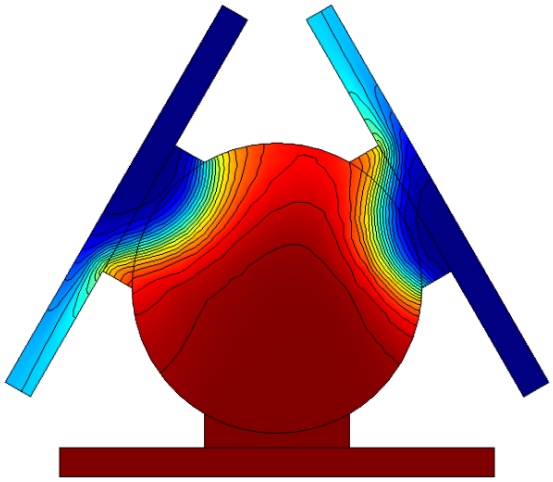

Figure 7.7: Numerically simulated convective flow. Source channel velocity of 0.001ms^-1 and sink channel velocities of 0.0004ms^-1

Chapter 8

Tetraselmis sp. swimming characteristics in media with varying alginate content

Mass culturing of algae is of interest particularly for the lipids contained within the cells as a source of raw component of biodiesel. Also of interest are other high value products, such as pharmaceuticals and food additives [Mata et al., 2010], that algae naturally produce. A large part of the energy cost of maintaining cultures is mixing. Mixing helps to reduce self-shading, and maximise the interception of light by cells. Bulk transport also facilitates a homogeneous culture, for temperature and nutrients. Some algae strains are self propelling, and are photo- and chemotatic, so they can direct their swimming according to light and chemical stimulus.

In this chapter the Tetra whole cell cultures are introduced into a microfluidic device, to study their motility in media with different concentrations of alginate. Numerical simulations were preformed to characterise and optimise the microfluidic device for design and operation in chapters 5 and 6. The concentration gradients were experimentally explored in

chapter 7, and a protocol for filling the devices was developed.

Experiments on motile cells are usually done using refined or concentrated cell cultures[Sokolov and Aranson, 2009] Rafai et al. [2010]. Fragments of lysed cells, and extracellular polymers are removed from the sample by centrifuging whole cell cultures and re-suspending the cells in clean media. This chapter's aim was to use whole cell cultures, which is representative of the algae culture straight from the flask with no processing. This is the fluid that must be understood to improve optimisation of photobioreactors.

The media, which is enriched with alginate to change its rheological properties, is subject to rotational and oscillatory rheological testing, to ascertain its elasticity and viscosity. Alginate was chosen to change the rheology of the media as a small amount can change the rheology, and it was thought not to be toxic to the Tetra cells Bozeman et al. [1989]. It was thought to be a good proxy for extracellular polymeric substances (EPS), and for fragments of lysed cells. f/2 media was prepared as either f/2, f/2 + 0.1% sodium alginate or f/2 + 0.4% sodium alginate. The *Tetraselmis* sp. code (66/24, CCAP, SAMS Research Services Ltd., Argyll, UK) was cultured at room temperature in f/2 media. To ensure maximum motility the culture was used within two weeks of delivery.

Proof of concept is presented for visualising cells within a disposable PDMS microfluidic device with the design shown in figure 8.1. A protocol was developed for getting motile cells into the central chamber, which allowed analysis of cell motility.

8.1 Media Rheology

Rotational rheometry was used to evaluate the steady shear viscosity of the media. The steady shear viscosity is of interest because of the conditions within the microfluidic chamber. Ideally, there would be very little shear flow in the central chamber, so the zero shear viscosity would be applicable. However, as demonstrated in chapter 7, there is significant convective flow, so the steady shear viscosity is more applicable. Figure 8.2 shows the steady shear viscosities for the enriched f/2 media.

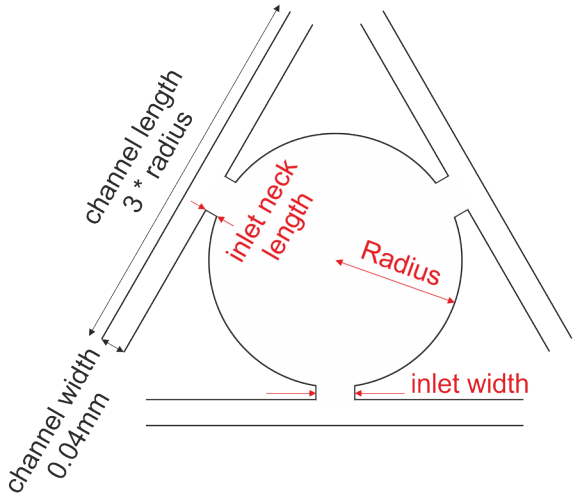

Figure 8.1: Schematic of the geometry used in this study. A central chamber served by three inlets

For f/2 media the steady shear viscosity was 1.11 mPas. For a volume fraction of dissolved solutes of 0.35 %, equation 8.1, discussed in section 2.5.2, predicts a fluid viscosity of 1.8 mPas. However, equation 8.1 does not hold above very dilute solution. Very dilute is considered to be approximately 0.1 %. It should not be expected that equation 8.1 models the situation well.

$$\eta_f = \eta_s(1 + 2.5\Theta) \tag{8.1}$$

The viscosity of the media for 0.1 % alginate was 1.4 ± 0.01 mPas and 0.4 % alginate was 9 ± 0.5 mPas. The alginate polysaccharide has increased the viscosity.

The oscillatory rheology of three different mediums, f/2, f/2 + 0.1% sodium alginate, f/2 + 0.4 % sodium alginate was tested with a frequency sweep. Oscillatory rheometry tests gives the phase angle, δ, of the media with changing angular frequency. These are shown in figure 8.3. The phase angle is a ratio of a material's viscous components and the elastic components, as detailed in section 2.5.1. A material with a phase angle of 90° exhibits only a viscous component, a material with a phase angle of 0° exhibits only an elastic component.

f/2 media, having only dissolved salts, has no significant elasticity, as expected. The aquarium salt solution, with only simple low molecular weight ions dissolved, does not have

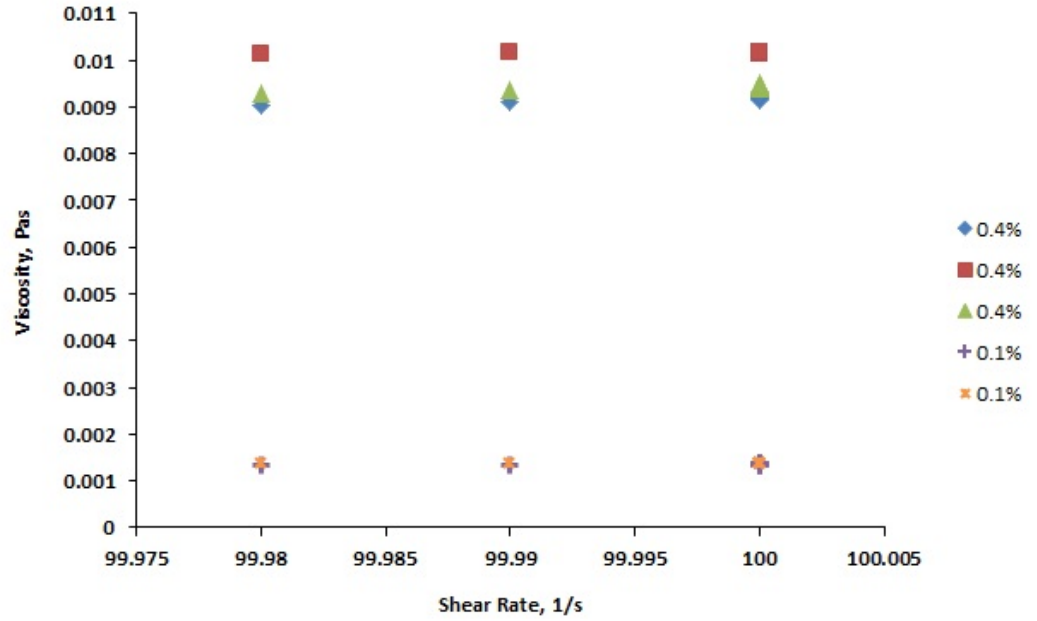

Figure 8.2: Steady shear viscosity of f/2 enriched with alginate.

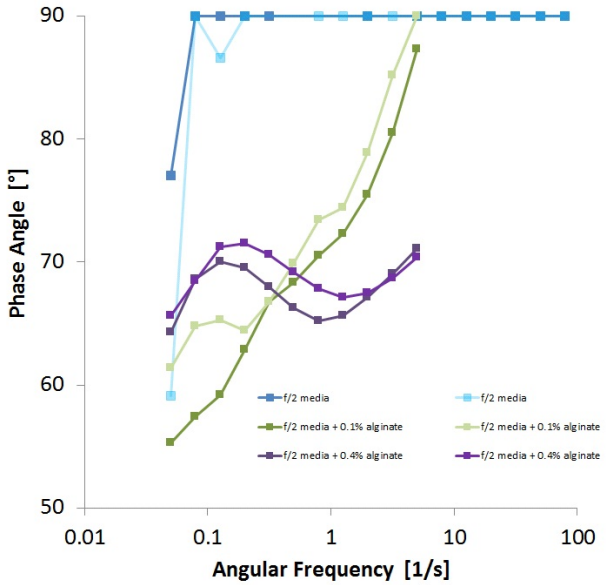

Figure 8.3: The relative elasticity of f/2 media with increasing alginate concentration

an elastic component.

Both the 0.1 % and 0.4 % alginate show an elastic component for the range of angular frequencies tested. As alginate content increases the elastic component is present at a wider range of frequencies.

8.2 Motile *Tetraselmis* sp. in the central chamber

The filling protocol that was developed in chapter 7 from section 7.2 was adapted to fill the chambers with f/2, m/f + 0.1% and f/2 + 0.4%.

A protocol was established for getting algae cells into the microfluidic central chamber.

Protocol for introducing *Tetraselmis* sp. whole cell culture

The 3 syringes from step 3 of the filling protocol should be filled with f/2 media with the desired amount of added alginate. A fourth syringe should be filled with *Tetraselmis sp.* whole cell culture that has been swirled to re-suspend any aggregated cells and fitted with a needle and hub, and a needle shaft.

After step 9 has been satisfied, i.e. the flow has equilibrated from the filling of the chambers at the high flow rate of 40 ml hour^{-1}, pipette a drop of f/2 media on an inlet port, remove one on the needles from the inlet port, and replace with syringe delivering whole cell culture.

This protocol enabled cells to enter the central chamber and be visualised using light microscopy.

With current designs, the inlet width was much larger than anticipated. Figure 8.4 shows the particular central chamber used. The central chamber has a radius of 300 μm, and the inlet has a width of 70 μm and no discernible neck.

As predicted in chapter 5, this meant that with the syringe pumps infusing at 0.0288 ml hour^{-1}, the cross flow was sufficient to make the cells tumble. It was decided to change the operating conditions to prevent the cells only being transported by advection, and not being able to actively swim. Data was collected with no flow in the inlet channels so that

the cells were able to swim. Once the whole cell culture had reached the central chamber, the flow in the inlet channels was switched off, by turning off the syringe pumps. By doing this, cells were able to actively swim within the central chamber.

Figure 8.5 shows the swimming tracks for actively swimming cells in each of the different media, with no flow in the inlet channels.

Bacterium use either run-tumble, or forward-reverse pattern [Luchsinger et al., 1999]. Marine bacteria have been found to use the mode forward-reverse-flick [Xie and Altindal, 2011]. However, very little is known about microalgae motility. Tetra cells do not swim in a direct line, shown in figure 8.5. However, they were not observed to run and tumble like *E.coli* [Xie and Wu, 2014]. The Tetra were observed to move with an indirect path, but without a tumble phase.

Figure 8.6(a) shows the speed of swimming cells. The swimming speed is decreased with increasing alginate content in the media. It has been shown that the algae swim more slowly, dropping from 200 μm sec^{-1} to 135μm sec^{-1}.

Figure 8.6(b) shows the directness of the path the algae takes.

Directness is a measure of the cell path [Asano et al., 2013]. It's represented by $D = \frac{d_{straightline}}{d_{cellpath}}$ where $d_{straightline}$ is the minimum distance between the cell starting and end point and $d_{cellpath}$ is the length of the actual path taken by the cell. Cell tracks become less direct with increasing alginate content in the media.

This supports the hypothesis that increasing alginate concentration hinders the motility of the cell. There is evidence that concentrations of alginate much higher than this are not toxic to algae cultures [Bozeman et al., 1989]. Assuming that the flagella on the cells are not damaged somehow by the presence of alginate, the evidence in this chapter supports the suggestion that whole cell culture, with lots of EPS, can increase the energy cost of mixing culture, through an increase in viscosity and a decrease in cell motility.

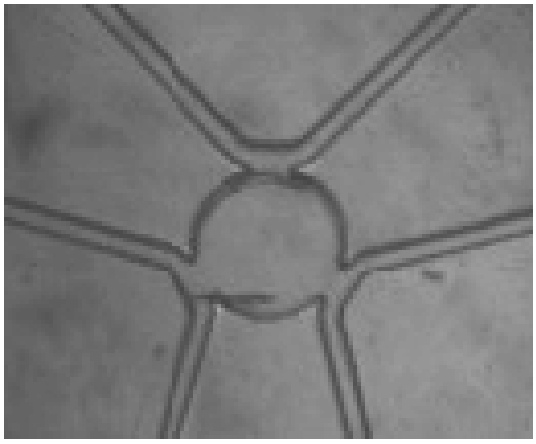

Figure 8.4: Microfluidic chamber used to visualise motile Tetra cells

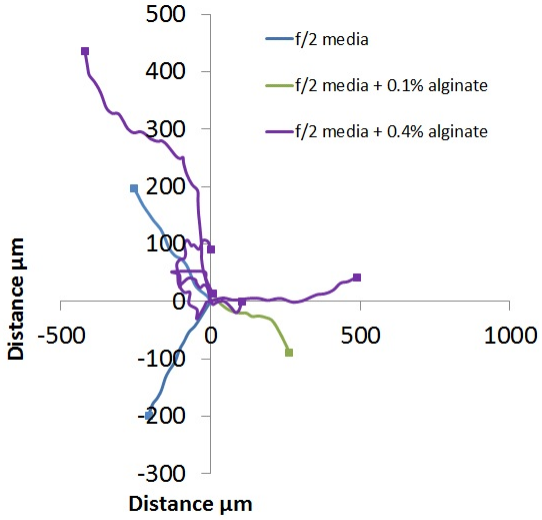

Figure 8.5: Paths of actively swimming cells, normalised so every cell starts at (0,0)

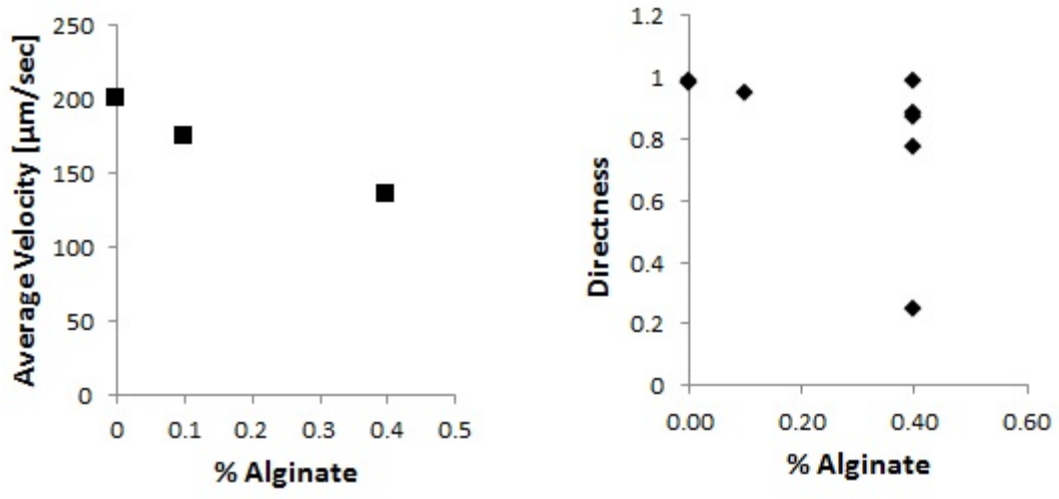

(a) Effect of the addition of alginate on the average velocity of cells

(b) Effect of the addition of alginate on the directness of the cell path

Figure 8.6: Effects of alginate in f/2 media on the swimming characteristics on Tetra whole cell cultures

8.3 Conclusion

Media enriched with alginate was rheologically characterised. Alginate adds an elastic component, which increases with increasing alginate concentration. The alginate also raises the steady shear viscosity from 1.1 mPas for f/2 media to 9 mPas for f/2 with 0.4 % alginate added.

The filling protocol developed in chapter 7 was adapted so whole cell culture containing motile cells were able to be visualised within the central chamber. The motility of the cells was analysed, in three different media, f/2, f/2 + 0.1% alginate and f/2 + 0.4% alginate. It has been found that increasing alginate content of the media restricts swimming velocity and decreases the directness of the cells' path.

Chapter 9

Conclusions

A microfluidic tool, capable of maintaining a concentration gradient, has been characterised, optimised for study of cell motility, fabricated and proof of concept presented for maintaining concentration gradients and visualising motile cells within the chamber.

Whole cell cultures, instead of centrifuged and re-suspended cells, were used in this project as they are more representative of the cultures within photobioreactors.

The rheology of whole cell culture was characterised using rotational and oscillatory rheometry. It was found that cultures of Tetra and Nanno were shear thinning. This has implications for the motility of cells, when bubbles are used to aerate and mix photobioreactors, as the shear from the bubbles rising could affect the viscosity that the cells experience. However, theoretical modelling of bubbles from 1 mm to 100 mm in diameter were found to impart a shear that correlates to the high shear plauteau viscosity. Culture surrounding the bubbles of any size experience the same viscosity.

Numerical simulations of the microfluidic device, for both geometric and operational considerations, were preformed and recommendations made, with a case study for using the device as a tool to study cell motility.

The inlet neck length and width can be used to restrict convective flow into the central chamber, and enable diffusion dominated transport. It is recommended that the ratio of

inlet width to length be less than 2. To minimise the time to reach steady state the central chamber should be designed to have a radius of less than 400 μm.

The inlet channel configuration can be optimised to maximise the concentrations available within the central chamber, by using a Down inlet channel configuration. The inlet channel configuration can also minimise the velocity at the centre point by using Anti configuration, but overall no configuration decreases the maximum velocity within the central chamber.

Channels were fabricated from PDMS and a protocol was developed for filling them. A concentration gradient was maintained within the central chamber. Suggestions for improving the PDMS microfluidic channels in the design stage were over emphasising the neck length and decreasing the inlet width, to compensate for the loss of resolution between the SU-8 wafer and the PDMS channels.

Proof of concept is presented for using the microfluidic tool to visualise the motility of whole cell cultures.

Media enriched with alginate was rheologically characterised. Sodium alginate was used to alter the rheological properties of the media.

Motile cells were recorded in the central chamber, by using an adapted filling protocol from chapter 7. The motility of the cells was analysed, in three different media. It has been found that increasing alginate content of the media restricts swimming velocity and decreases the directness of the cells' path.

This thesis has demonstrated that microfluidic devices have the potential to study cell motility. The design developed in this thesis allows a concentration gradient to be maintained and chemotaxis to be analysed.

Chapter 10

Future Work

This chapter outlines some areas that could extend the current project.

10.1 Additions to the COMSOL simulations

Simulations completed in COMSOL all had balanced flows in the three inlet channels. Inducing controlled convection within the central chamber would be possible by having uneven channel flowrates. This would allow convective transport within the central chamber, without having to increase the inlet width. This has the potential to decrease the time for concentration gradients to reach steady state.

10.2 Redesigning the channels

The current design for the channels did not take into account the unexpected reduction in resolution between the pattern on the photoresist mask and the PDMS channel. This meant that the neck and inlet dimensions were not as expected. Results from chapter 5 prove that the geometry is an important factor affecting the time to reach steady state and the shape of the concentration gradient. A redesign of the photoresist mask should overemphasise the height of the neck, which would make allowances for the PDMS resolution around tight

corners and allow for the inlets to be sufficiently narrow. It should be possible to have inlets as narrow as 40 μm. The width of the inlet channels was 40 μm, and this dimension was consistent and reliable.

10.3 Characterisation of concentration gradients and flow profiles

Pulsating flows, created by using the syringe pump at the lower end of its capabilities, made it hard to experimentally characterise the concentration gradients in the PDMS channels. Using a syringe pump capable of smooth μl min^{-1} flow rates would aid the characterisation of the experimental concentration gradients.

In this project, only data on the experimental concentration gradient was collected. Using fluorescent tracer particles, the flow regime within the chamber could also be characterised.

10.4 Improving the cell count within the central chamber

Getting a high enough concentration of cells within the central chamber was a problem. The disposable polypropylene syringes used in chapter 8 had a rubber seal on the plunger. Some aggregation of cells on the rubber seal was observed, which lowered the concentration of cells entering the inlet port. This could possibly be overcome by pre-coating it in oil using glass syringes that don't use rubber seals.

For future experimental work the algae *Dunaliella tertiolecta* may be chosen. It is a possible candidate as a feed stock for biofuel [Gouveia and Oliveira, 2009]. It also is described as easy to cultivate due to its tolerance in conditions [Chengala et al., 2010, Rodolfi et al., 2009]

10.5 Using the channels to study chemotaxis

A concentration gradient across the central chamber of a chemo-effector could be used to study chemotaxis of motile cells. The additive effect of up to three chemo-effectors, one in each inlet channel, could be studied in one device. This could be used to identify chemo-attractants or chemo-repellents for specific species. It could also be developed into a diagnostic tool, by calibrating cell responses to standardised concentrations of chemo-effectors and measuring the chemotatic response to unknown concentrations. This is not only applicable to motile algae, but to bacteria as well.

10.6 Microfluidic bioreactors

It may be possible to use the central chamber, not only for the study of motile cells, but also to study the growth of cells. Using the capability of the device to maintain a concentration gradient, the central chamber could be used as a microbioreactor within which cells are grown in incrementally different concentrations.

Appendices

Appendix A

SOP Wafer Master Template Manufacturing and Silanization

Protocol- SU8 (2007, 2010 and 2015) Wafer Master Template Manufacturing and Silanization Created by Julian George

SU-8 cross-links when exposed to 350-400nm UV light, (365nm is recommended). Upon exposure, a strong acid is formed, which is used to catalyse the thermally driven cross-linking during the post bake exposure step.

Recommended program

1. Remove SU-8 from fridge, dispense 5ml per wafer and allow the SU-8 to come to room temperature before use.
2. In the clean room, turn on pump at wall. Set spin coater to Program mode.
3. Set one plate heater to 65°C, the other to 95°C.
4. Set or program the correct spin program (include acceleration time in calculations) 2000rpm for 45 seconds (acceleration of 100rpm / second)
5. Place wafer onto centre of the spinner, press VAC to hold in place, and do a short RUN to check alignment (if not aligned, press VAC again to release wafer, and repeat alignment)
6. Closely dispense 5ml of SU-8 into the middle of the wafer using a 10ml syringe, or pour directly
7. When ready, turn on VAC to hold wafer, switch to RUN and press ENTER to start
8. EDGE bead removal this can be done during spinning using a squeezy bottle of EBR PG solvent to spray the edges of the wafer and remove any edge bead, resulting in improved contact between the wafer and the mask during the exposure step.
9. !!! Be careful and slow when lifting the spin coater lid mind the drips. Clean the drips from the edge of the spin coater and carefully remove the wafer, ensuring no drips fall onto the spun surface.
10. Soft bake at 95°C according to MicroChem datasheets. You can split this into 1 min at 65°C and the rest of the time at 95°C to reduce the risk of cracking of the SU8. 1 min at 65°C, 2mins 30 seconds at 95°C
11. Leave to cool to RT.

12. Place the mask over the wafer, and place the UV band-pass filter on top. Use magnets to ensure that there is no gap between the wafer and the film air gaps will significantly distort the final result.

13. Expose for 21 seconds at 60% power.

14. Post Bake directly after exposure to crosslink at 95°C. Again, the first minute is at 65°C. 1 min at 65°C, 3 mins 20 seconds at 95°C

15. Develop (outside the clean room) by first gently spraying SU-8 developer onto the wafer using a spray bottle, and then immerse in developer and agitate for 2-4 minutes (depending on coating thickness).

16. Remove from developer and perform a further gentle spray rinse in developer (10 seconds).

17. Rinse in Ethanol / IPA for 10 seconds. If you see a white film, repeat the developer rinse, and the Ethanol / IPA rinse.

18. Air dry or dry in a stream of nitrogen.

19. Hard bake at 150°C for 10-15 minutes.

Silanization of Wafer Master Template

1. Clean off surface of Wafer with SU-8 stamp using nitrogen gas to remove any dust particles.

2. In the fume hood, place Wafer in a 5-inch petri dish. CHLOROTRIMETHYLSILANE IS VERY TOXIC! DO NOT INHALE OR HAVE SKIN CONTACT!

3. Drop about 0.5 ml of chlorotrimethysilane around the Wafer using a disposal pipette pasteur. Do not drop the silane directly on the Wafer. Cover with the petri dish lid.

4. Cover the petri dish and allow 5 minutes for monolayer formation. After this time all the silane will have evaporated, and Wafer is now ready to use.

Appendix B

SOP OXYGEN PLASMA GENERATOR USAGE

Standard Operation Procedure

TE05 v1.0

OXYGEN PLASMA GENERATOR USAGE

Location: IBME Room 678.20.96 Created by Julian George on 11/02/2013

Warning: Samples exposed to Oxygen plasma may become hot. - use caution when removing samples from the chamber. Note: - Please be careful not to scratch or contaminate the inside of the glass chamber - Always pump down the chamber after use to prevent contamination of the chamber by dust, etc - Always turn off the O2 cylinder after use to prevent gas leakage

Procedure

1. Turn on the system at the wall, and on the front of the unit
2. Turn on the Oxygen cylinder on the bottle neck and set the regulator to 1 bar
3. Set the power level according to the effect required (typically 60%)
4. To open the chamber, ventilate the chamber by pressing the VENTILATION button
5. Place your sample on a tray in the middle of the chamber
6. Make sure both gas control valves are turned off on the front of the unit
7. Replace the door, hold in place to ensure a good seal and press PUMP to pump down the chamber for 60 seconds [after this, keep the PUMP on throughout]
8. Introduce oxygen into the chamber using the [O2] control valve on the front of the unit at an approximate flow of 0.4 ml/minute for 30 seconds
9. Turn off the oxygen and press the GENERATOR button to ignite the plasma
10. Turn off the GENERATOR after the required time (typically 60 seconds)
11. Turn off the PUMP and press VENTILATION to vent the chamber Note: This will cause air to rush into the chamber. If a slower flow of gas is required to prevent samples flying around the chamber, use the [X] gas flow control to slowly vent the chamber. It will take considerably longer to vent the chamber this way.
12. After 30 seconds, the chamber door should release and you can remove your treated samples. CAUTION: Sample may become hot use the protective gloves to remove samples where necessary

13. After use, make sure that the door seal is clean, replace the door and pump down the chamber to prevent dust and contaminants from entering the chamber between usage

14. Turn off the O2 gas bottle at the cylinder neck to prevent leakage

Appendix C

Mathematica code

Mathematica code developed for Chapter 4

```
In[17]:= CD0[f_, a_, v_] := f / a / (1 / 2 ρ v^2)

In[18]:= CD0[4 / 3 π a^3 g dρ, 4 π a^2, v]

Out[18]= 2 a dρ g / (3 v^2 ρ)

In[19]:= CD1[v_, η_, a_] := 16 / (ρ v 2 a / η) (1 + 0.15 (ρ v 2 a / η)^0.687)

In[20]:= frac[v_, η_, a_] :=
          1 / CD0[v, a] * CD1[v, η, a] /.
           {ρ → 1000, dρ → (1000 - 1.2), g → 10}

In[21]:= vel[a_, η_] :=
          Module[{},
           v /. Last[NMinimize[{1, frac[v, η, a] == 1, v < 25 a + 4, v > 26 a - 1}, v]]]

In[22]:= vel[0.00001, .01]
```

Bibliography

Victoria Oluwatosin Adesanya. *Rheological Characterisation of Algae for the Production of Biofuels*. PhD thesis, University of Cambridge, 2010.

Tanvir Ahmed and Roman Stocker. Experimental verification of the behavioral foundation of bacterial transport parameters using microfluidics. *Biophysical journal*, 95(9):4481–93, November 2008.

Tanvir Ahmed, Thomas S Shimizu, and Roman Stocker. Bacterial chemotaxis in linear and nonlinear steady microfluidic gradients. *Nano letters*, 10(9):3379–85, 2010.

Y Asano, E Horn, and Trapp G. Chemotaxis and Migration Tool 2.0, 2013. URL `http://ibidi.com/fileadmin/products/software/chemotaxis_tool/IN_XXXXX_CT_Tool_2_0.pdf`.

Javier Atencia, Jayne Morrow, and Laurie E Locascio. The microfluidic palette: a diffusive gradient generator with spatio-temporal control. *Lab on a chip*, 9(18):2707–14, 2009.

Peter Atkins. *Atkins' Physical Chemistry, 2nd Edition*. Oxford Univerisity Press, Oxford, 1982. ISBN 0198551517.

J. Barrios-Gonzalez, A. Tomasini, G. Viniegra-Gonzalez, and L. Lopez. Penicillin production by solid state fermentation. *Biotechnology Letters*, 10(11):793–798, November 1988.

G K Batchelor. Slender-Body Theory For Particles Of Arbitrary Cross-Section In Stokes Flow. *Journal Of Fluid Mechanics*, 44(NOV26):419–&, 1970.

John Bozeman, Ben Koopman, and Gabriel Bitton. Toxicity testing using immobilized algae. *Aquatic Toxicology*, 14(4):345–352, May 1989. URL `http://www.sciencedirect.com/science/article/pii/0166445X89900325`.

Dennis Bray. *Cell Movements; From Molecules to Motility*. Garland Pub., 2001.

Liam Brennan and Philip Owende. Biofuels from microalgaeA review of technologies for production, processing, and extractions of biofuels and co-products. *Renewable and Sustainable Energy Reviews*, 14(2):557–577, February 2010.

H Brenner. Rheology Of A Dilute Suspension Of Dipolar Spherical Particles In An External Field. *Journal Of Colloid And Interface Science*, 32(1):141–158, 1970.

P. Cappuccinelli. *Motility of living cells*. Chapman and Hall, 1980.

Ana P Carvalho, A Meireles, and F Xavier Malcata. Microalgal Reactors : A Review of Enclosed System Designs and Performances. *Biotechnology Progress*, (ii):1490–1506, 2006.

Ahammed Anwar Chengala, Miki Hondzo, Dan Troolin, and Paul A Lefebvre. Kinetic responses of Dunaliella in moving fluids. *Biotechnology and bioengineering*, 107(1):65–75, 2010.

Yusuf Chisti. Biodiesel from microalgae. *Biotechnology advances*, 25(3):294–306, 2007.

Sheng-Yi Chiu, Chien-Ya Kao, Ming-Ta Tsai, Seow-Chin Ong, Chiun-Hsun Chen, and Chih-Sheng Lin. Lipid accumulation and CO2 utilization of Nannochloropsis oculata in response to CO2 aeration. *Bioresource technology*, 100(2):833–8, 2009.

M S Croughan, J F Hamel, and D I C Wang. Hydrodynamic Effects On Animal-Cells Grown In Microcarrier Cultures. *Biotechnology And Bioengineering*, 29(1):130–141, 1987.

Maurycy Daroch, Shu Geng, and Guangyi Wang. Recent advances in liquid biofuel production from algal feedstocks. *Applied Energy*, 102:1371–1381, 2013.

Yanan Du, Jaesool Shim, Mahesh Vidula, Matthew J Hancock, Edward Lo, Bong Geun Chung, Jeffrey T Borenstein, Masoud Khabiry, Donald M Cropek, and Ali Khademhosseini. Rapid generation of spatially and temporally controllable long-range concentration gradients in a microfluidic device. *Lab on a chip*, 9(6):761–7, 2009.

Randy Ewoldt, Lucas Caretta, Anwar Chengala, and Jian Sheng. Effective Viscosity of Actively Swimming Algae Suspensions. *Unpublished*, (Poster presentation at 82nd Annual Society of Rheology Meeting), 2010.

K K Fleming Glass, E K Longmire, and A Hubel. Optimization of a microfluidic device for diffusion-based extraction of DMSO from a cell suspension. *International journal of heat and mass transfer*, 51(23-24):5749–5757, 2008.

James Friend and Leslie Yeo. Fabrication of microfluidic devices using polydimethylsiloxane. *Biomicrofluidics*, 4(2):026502–026502–5, January 2010.

E Gallagher. The Gallagher review of the indirect effects of biofuels production. Technical report, Renewable Fuels Agency, 2008. URL `http://www.unido.org`.

P-O Gendron, F Avaltroni, and K J Wilkinson. Diffusion coefficients of several rhodamine derivatives as determined by pulsed field gradient-nuclear magnetic resonance and fluorescence correlation spectroscopy. *Journal of fluorescence*, 18(6):1093–101, November 2008.

N.K. Gill, M. Appleton, F. Baganz, and G.J. Lye. Design and characterisation of a miniature stirred bioreactor system for parallel microbial fermentations. *Biochemical Engineering Journal*, 39(1):164–176, 2008.

James William Goodwin and Roy W. Hughes. *Rheology for chemists: an introduction*. Royal Society of Chemistry, 2008.

Luisa Gouveia and Ana Cristina Oliveira. Microalgae as a raw material for biofuels production. *Journal of industrial microbiology & biotechnology*, 36(2):269–74, 2009.

H C Greenwell, L M L Laurens, R J Shields, R W Lovitt, and K J Flynn. Placing microalgae on the biofuels priority list: a review of the technological challenges. *Journal of the Royal Society, Interface / the Royal Society*, 7(46):703–26, 2010.

Melinda J. Griffiths and Susan T. L. Harrison. Lipid productivity as a key characteristic for choosing algal species for biodiesel production. *Journal of Applied Phycology*, 21(5): 493–507, January 2009.

Yashodhan Hatwalne, Sriram Ramaswamy, Madan Rao, and R. Simha. Rheology of Active-Particle Suspensions. *Physical Review Letters*, 92(11), 2004.

K. Hayashi and A. Tomiyama. A drag correlation of fluid particles rising through stagnant liquids in vertical pipes at intermediate Reynolds numbers. *Chemical Engineering Science*, 64(12):3019–3028, 2009.

IPCC. Climate Change 2014. Mitigation of Climate Change. Technical report, Cambridge University Press, New York, 2014. URL `http://www.ipcc.ch/report/ar5/wg3/`.

T Ishikawa. Suspension biomechanics of swimming microbes. *Journal of the Royal Society Interface*, 6(39):815–834, 2009. doi: 10.1098/rsif.2009.0223.

T Ishikawa, M P Simmonds, and T J Pedley. Hydrodynamic interaction of two swimming model micro-organisms. *Journal of Fluid Mechanics*, 568:119–160, 2006.

Kazem Jamshidi-Ghaleh, Mohammad Taghi Tavassoly, and Nastaran Mansour. Diffusion coefficient measurements of transparent liquid solutions using Moiré deflectometry. *Journal of Physics D: Applied Physics*, (14):1993–1997, July 2004.

P Jaouen, L Vandanjon, and F Quéméneur. The shear stress of microalgal cell suspensions (Tetraselmis suecica) in tangential flow filtration systems: the role of pumps. *Bioresource technology*, 68:149–154, 1999.

Tolga Kaya and Hur Koser. Direct upstream motility in Escherichia coli. *Biophysical journal*, 102(7):1514–23, April 2012.

Martin Kolnik, Lev S Tsimring, and Jeff Hasty. Vacuum-assisted cell loading enables shear-free mammalian microfluidic culture. *Lab on a chip*, 12(22):4732–7, 2012.

Andrew K. Lee, David M. Lewis, and Peter J. Ashman. Disruption of microalgal cells for the extraction of lipids for biofuels: Processes and specific energy requirements. *Biomass and Bioenergy*, 46:89–101, 2012.

AS Lubansky, DV Boger, and JJ Cooper-White. Batchelor's theory extended to elongated cylindrical or ellipsoidal particles. *Journal Of Non-Newtonian Fluid Mechanics*, 130(1): 57–61, 2005.

Rolf H Luchsinger, Birger Bergersen, and James G Mitchell. Bacterial Swimming Strategies and Turbulence. 77(November):2377–2386, 1999.

Hanbin Mao, Paul S Cremer, and Michael D Manson. A sensitive, versatile microfluidic assay for bacterial chemotaxis. *Proceedings of the National Academy of Sciences of the United States of America*, 100(9):5449–54, 2003.

Marcos and Roman Stocker. Microorganisms in vortices: a microfluidic setup. *Limnology And Oceanography-Methods*, pages 392–398, 2006.

Teresa M. Mata, António A. Martins, and Nidia. S. Caetano. Microalgae for biodiesel production and other applications: A review. *Renewable and Sustainable Energy Reviews*, 14:217–232, 2010.

J C McDonald, D C Duffy, J R Anderson, D T Chiu, H Wu, O J Schueller, and G M Whitesides. Fabrication of microfluidic systems in poly(dimethylsiloxane). *Electrophoresis*, 21 (1):27–40, 2000.

J C Merchuk. *Bioreactor systems and effects : Shear effects on suspended cells*. Springer-Verlag, Berlin, 1991.

Christian M Metallo, Maxim A Vodyanik, Juan J de Pablo, Igor I Slukvin, and Sean P Palecek. The response of human embryonic stem cell-derived endothelial cells to shear stress. *Biotechnology and bioengineering*, 100(4):830–7, 2008.

Jan Mewis and Norman J. Wagner. Current trends in suspension rheology. *Journal of Non-Newtonian Fluid Mechanics*, 157(3):147–150, April 2009.

Dwight Neuenschwander. Albert Einstein's Dissertation: Elegant Connections in Physics. Technical report, 1999.

T J Pedley and J O Kessler. Hydrodynamic Phenomena In Suspensions Of Swimming Microorganisms. *Annual Review of Fluid Mechanics*, 24:313–358, 1992.

E Purcell. Life at Low Reynolds Number. *American Journal of Physics*, 45(June 1976): 3–11, 1976.

Salima Rafai, Levan Jibuti, and Philippe Peyla. Effective Viscosity of Microswimmer Suspensions. *Physical Review Letters*, 104(9), 2010.

Sriram Ramaswamy. The Mechanics and Statistics of Active Matter. *Annual Review of Condensed Matter Physics*, 1(1):323–345, August 2010.

I. Rawat, R. Ranjith Kumar, T. Mutanda, and F. Bux. Biodiesel from microalgae: A critical evaluation from laboratory to large scale production. *Applied Energy*, 103:444–467, 2013.

Liliana Rodolfi, Graziella Chini Zittelli, Niccolò Bassi, Giulia Padovani, Natascia Biondi, Gimena Bonini, and Mario R Tredici. Microalgae for oil: strain selection, induction of lipid synthesis and outdoor mass cultivation in a low-cost photobioreactor. *Biotechnology and bioengineering*, 102:100–12, 2009.

Roberto Rusconi, Jeffrey S. Guasto, and Roman Stocker. Bacterial transport suppressed by fluid shear. *Nature Physics*, 10(3):212–217, February 2014.

Peer M. Schenk, Skye R. Thomas-Hall, Evan Stephens, Ute C. Marx, Jan H. Mussgnug, Clemens Posten, Olaf Kruse, and Ben Hankamer. Second Generation Biofuels: High-Efficiency Microalgae for Biodiesel Production. *BioEnergy Research*, 1:20–43, 2008.

Caroline A Schneider, Wayne S Rasband, and Kevin W Eliceiri. NIH Image to ImageJ: 25 years of image analysis. *Nature Methods*, 9(7):671–675, June 2012.

Stuart a Scott, Matthew P Davey, John S Dennis, Irmtraud Horst, Christopher J Howe, David J Lea-Smith, and Alison G Smith. Biodiesel from algae: challenges and prospects. *Current opinion in biotechnology*, 21(3):277–86, June 2010.

A H Scragg, E J Allan, and F Leckie. Effect Of Shear On The Viability Of Plant-Cell Suspensions. *Enzyme And Microbial Technology*, 10:361–367, 1988.

Andrey Sokolov and Igor Aranson. Reduction of viscosity in suspension of swimming bacteria. *Phys Rev Lett*, 103(14):148101, 2009.

Joni J. St. John, Daniel J. Schroen, and H. Tak Cheung. An adhesion assay using minimal shear force to remove nonadherent cells. *Journal of Immunological Methods*, 170(2):159–166, April 1994.

Alberto Steriti, Roberto Rossi, Alessandro Concas, and Giacomo Cao. A novel cell disruption technique to enhance lipid extraction from microalgae. *Bioresource technology*, 164:70–7, 2014.

Roger I Tanner. *Engineering rheology*. Oxford : Oxford University Press, Oxford, 2000.

Graham B. Wallis. *One-dimensional Two-phase Flow*. McGraw-Hill, 1969.

Judyta Wegrzyn, Adam Samborski, Louisa Reissig, Piotr M. Korczyk, Slawomir Blonski, and Piotr Garstecki. Microfluidic architectures for efficient generation of chemistry gradations in droplets. *Microfluidics and Nanofluidics*, 14(1-2):235–245, 2012.

Douglas B Weibel, Willow R Diluzio, and George M Whitesides. Microfabrication meets microbiology. *Nature reviews. Microbiology*, 5(3):209–18, 2007.

George M Whitesides. The origins and the future of microfluidics. *Nature*, 442(7101):368–73, 2006.

Peter J. le B. Williams and Lieve M. L. Laurens. Microalgae as biodiesel & biomass feedstocks: Review & analysis of the biochemistry, energetics & economics. *Energy & Environmental Science*, 3(5):554, May 2010. ISSN 1754-5692.

Li Xie and Tuba Altindal. Bacterial flagellum as a propeller and as a rudder for efficient chemotaxis. In *Proceedings of the National Academy of Sciences of the United States of America*, volume 2010, 2011. URL `http://www.pnas.org/content/108/6/2246.short`.

Li Xie and Xiao-Lun Wu. Bacterial motility patterns reveal importance of exploitation over exploration in marine microhabitats. Part I: theory. *Biophysical journal*, 107(7):1712–20, October 2014.

Ding-Bang Xu, CynthiaP. Madrid, Max Rohr, and ChristianP. Kubicek. The influence of type and concentration of the carbon source on production of citric acid by Aspergillus niger. *Applied Microbiology and Biotechnology*, 30(6), June 1989.

Kimiko Yamamoto, Takaaki Sokabe, Tetsuro Watabe, Kohei Miyazono, Jun K Yamashita, Syotaro Obi, Norihiko Ohura, Akiko Matsushita, Akira Kamiya, and Joji Ando. Fluid shear stress induces differentiation of Flk-1-positive embryonic stem cells into vascular endothelial cells in vitro. *American journal of physiology. Heart and circulatory physiology*, 288:H1915–24, 2005.

Xiaowei Zhang, Matthieu Stettler, Oscar Reif, Andreas Kocourek, Maria Dejesus, David L Hacker, and Florian M Wurm. Shaken helical track bioreactors: Providing oxygen to high-density cultures of mammalian cells at volumes up to 1000 L by surface aeration with air. *New biotechnology*, 25:68–75, 2008.

Guoxia Zheng, Yunhua Wang, and Jianhua Qin. Microalgal motility measurement microfluidic chip for toxicity assessment of heavy metals. *Analytical and bioanalytical chemistry*, 404(10):3061–9, 2012.